NIST Special Publication 1087

COOLING MODE FAULT DETECTION AND DIAGNOSIS METHOD FOR A RESIDENTIAL HEAT PUMP

Minsung Kim
Seok Ho Yoon
W. Vance Payne
Piotr A. Domanski

NIST National Institute of Standards and Technology • U.S. Department of Commerce

NIST Special Publication 1087

COOLING MODE FAULT DETECTION AND DIAGNOSIS METHOD FOR A RESIDENTIAL HEAT PUMP

Minsung Kim
Korea Institute of Energy Research
Geothermal Energy Research Center
71-2 Jang-dong, Yuseong-gu, Daejeon 305-343, Korea

Seok Ho Yoon
Korea Institute of Machinery and Materials
Energy Systems Research Division
171 Jang-dong, Yuseong-gu, Daejeon 305-343, Korea

W. Vance Payne
Piotr A. Domanski
U.S. DEPARTMENT OF COMMERCE
National Institute of Standards and Technology
Building Environment Division
Building and Fire Research Laboratory
Gaithersburg, Maryland 20899-8631, USA

October 2008

Certain commercial entities, equipment, or materials may be identified in this document in order to describe an experimental procedure or concept adequately. Such identification is not intended to imply recommendation or endorsement by the National Institute of Standards and Technology, nor is it intended to imply that the entities, materials, or equipment are necessarily the best available for the purpose.

BRIEF SUMMARY OF THE RESEARCH

This research addresses the need for fault detection and diagnosis (FDD) in residential-style, air conditioner, and heat pump systems in an attempt to make these systems more trouble free and energy efficient over their entire lifetime. This work is one of the first to apply FDD techniques to a residential system with the added control element of a thermostatic expansion valve (TXV). Any control element actively seeks to perform its duties and thus obscures any faults occurring by making adjustments. This research work takes this into account and shows how FDD techniques may be applied to this type of system operating in the cooling mode.

Performance characteristics of an R410A residential unitary split heat pump equipped with a TXV were investigated in the cooling mode under no-fault and faulty conditions. Six artificial faults were imposed: compressor/reversing valve leakage, improper outdoor air flow, improper indoor air flow, liquid-line restriction, refrigerant undercharge/overcharge, and presence of non-condensable gas.

An automated method of steady-state detection was developed to produce consistent collection of data for all tests. The no-fault test measurements were used to develop a multivariate polynomial reference model for those system features (temperatures) that varied the most when a single fault was imposed. Outdoor air dry-bulb temperature, indoor air dry-bulb temperature, and indoor air dew-point temperature were used as the independent variables. From the no-fault reference model, feature residuals (differences between model predictions and measured values) were determined. Since the system was controlled by a TXV, the system could adapt itself to external variation much easier than a system with a fixed area expansion device. This added measure of refrigerant flow control provided by the TXV meant that the system compensated for faulty behavior more easily than a fixed area expansion device system. The distinctiveness of a fault depended on the TXV control status (fully open or fully closed), and thus the TXV affected the fault response of the selected features.

The rule-based chart method of fault detection and diagnosis presented in this work requires knowledge of the variation of system features at steady-state and during transient operation. Knowledge of the transient variation of the various features is necessary to establish the size of the moving window used by the steady-state detector, which is a key part of our FDD method. The goodness of fit of the no-fault reference model along with the lack of measurement repeatability from one day to the next was included in developing the FDD algorithm. The steady-state detector is the foundation upon which the FDD algorithm rests; only when all system features are within their strictly defined steady-state limits does the FDD algorithm begin applying the rule sets as defined in its rule-based chart. These steady-state limits are based upon the standard deviation of the feature values, within a fixed-time-interval moving window, being less than three times their no-fault steady-state standard deviation values.

Once the steady-state detector indicates that the important FDD features are steady, the difference in the moving window mean and the no-fault reference model values, feature residuals, are calculated using the no-fault reference model. A feature residual may have one of three values; positive or up-arrow $\uparrow$, negative or down-arrow $\downarrow$, or neutral [no change, NC (−)]. The NC case is defined by a positive and negative threshold about the moving window mean value. Each case has an associated probability of occurrence, $P(C \mid X)$, as shown in Figure *i*.
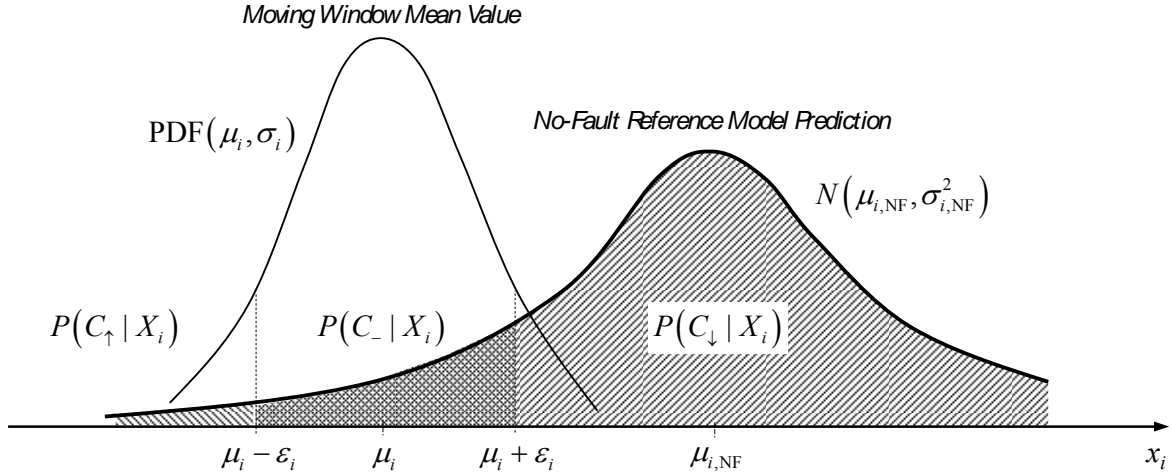
Figure *i*. Threshold for a moving window mean value

The calculation of the neutral threshold value, ε, involves selecting a confidence level (for example 99 %) to avoid a false alarm. For a given confidence level, the calculation of the appropriate confidence interval involves determining the appropriate variances (uncertainty) associated with steady-state measurement variations, modeling, and lack of measurement repeatability. These three sources of variance have individual confidence intervals associated with them, and their square rooted sum value gives the final value of ε at the given confidence level. With ε defined, the probability for each of the three cases may be calculated as shown in Figure *i*.

Looking at an example of a rule-based chart as shown in Table *i*, each positive, negative, or neutral case index (rows of the table) for the important features (columns of the table) has an associated probability (0< P(C | X)<1) including the probability of no-fault. The probability of a given fault is the product of all probabilities in a given row. When the probability of a given fault is higher than the no-fault probability (all calculated at the previously stated confidence level), the system most likely has this fault occurring.

Table *i*. Example rule-based chart

Fault Type	T_E	T_{sh}	T_D	T_C	T_{sc}	ΔT_{CA}	ΔT_{EA}
Refrigerant undercharge	↓	↑	↑	↓	↓	↓	↓
Refrigerant overcharge	–	–	↑	↑	↑	–	–
No-fault	–	–	–	–	–	–	–

The techniques discussed above are applied to a residential heat pump in the cooling mode with our results discussed herein. The addition of a complete definition of the no-fault case and the method of handling the TXV are unique to this work. The methods discussed in this work may be applied to any vapor compression system that can experience similar faults.

TABLE OF CONTENTS

LIST OF TABLES

LIST OF FIGURES

NOMENCLATURE

Symbols

a	coefficient of multivariate polynomial or a constant
A	air side or area
C	mass flow correction coefficient used with a TXV, or a general case-variable
F	fault case
g	number of coefficients used in a reduced coefficient correlation
h	specific enthalpy (kJ kg^{-1})
i	feature index
k	index of time
m	mass flow rate (kg/h)
m	mean or number of coefficients
n	number of data samples in a moving window
N	compressor rotational speed, or number of data points, or normal distribution
P	pressure (kPa) or probability
Q	capacity (W)
r	residual
s	positive constant multiplier of the measurement threshold
t	time
T	temperature (ºC)
u	mean value
v	variance
W	work (W)
x	variable representing measured data
$\bar{x}$	moving window average of measured data
z	feature residual
Z	set of feature residuals

Greek Symbols

α	probability of a classification error (%)
Δ	difference
ϕ	feature or performance parameter
ε	threshold value
σ	standard deviation
ρ	density

Subscripts

avg	average
comp	compressor
c	coefficients in the TXV mass flow rate equation
C	condenser
CA	condenser air
CW	condenser water in water-to-water heat pump
d	TXV discharge
D	compressor discharge
DB	dry bulb
exp	experimental
E	evaporator
EA	evaporator air
EB	evaporator brine in water-to-water heat pump
full	full model with all coefficients included
ID	indoor

IDP	indoor dew point
m	number of features
map	compressor performance map
NF	no fault
R	refrigerant
reduced	model with some coefficients removed as compared to full model
S	saturated refrigerant property
sc	subcooling
sh	superheat
ss	steady-state

Acronyms/Abbreviations

AC	air conditioner
ANN	artificial neural network
CF	condenser air flow fault
CFM	volumetric flow rate in cubic feet per minute (ft^3 min^{-1})
CMF	compressor fault
COP	coefficient of performance
DOE	United States Department of Energy
EER	energy efficiency ratio
EF	evaporator air flow fault
EPA	Environmental Protection Agency
FDD	fault detection and diagnosis
HP	heat pump
HVAC(&R)	heating, ventilating and air-conditioning (and refrigeration)
LL	liquid line or liquid line fault
MPR	multivariate polynomial regression
MS	mean squared
MSR	mean squared residual
MW	moving window
OC	refrigerant overcharged fault
OD	outdoor
PDF	probability density function
RH	relative humidity
scfm	standard cubic feet per minute (70 ^{o}F dry air with a density of 0.075 lbm ft^3)
SSR	sum of squared residuals
TXV	thermostatic expansion valve
UC	refrigerant undercharge fault
VAV	variable air volume

CHAPTER 1. BACKGROUND

This work examines *cooling mode* fault detection and diagnosis of a residential heat pump system with the intent of making these systems more trouble free and energy efficient over their entire lifetime. An increasing emphasis on energy saving and environmental conservation requires that air conditioners and heat pumps be highly efficient. To this end, a few government initiatives have been undertaken. For example, the EPA's Global Programs Division is responsible for the assessment of alternative refrigerant's performance and enforcement of the Clean Air Act. Another prime example is the ENERGY STAR initiative, a program formulated by the EPA/Climate Protection Partnerships Division and the Department of Energy (DOE), which promotes products that offer energy efficiency gains and pollution reduction. Directly affecting residential equipment, a recent DOE regulation imposed a 30 % increase in the minimum seasonal energy efficiency ratio (SEER) for central air conditioners, from 10.0 to 13.0, beginning January 23, 2006.

To ensure that heating, ventilating, and air-conditioning (HVAC) equipment operates in the field at its design efficiency, the efforts exerted by equipment manufacturers to improve equipment's SEER must be paralleled in the field by good equipment installation and maintenance practices. However, a survey of over 55 000 residential and commercial units found the refrigerant charge to be incorrect in more than 60 % of the systems (Proctor, 2004). Another independent survey of 1500 rooftop units showed that the average efficiency was only 80 % of the expected value, primarily due to improper refrigerant charge (Rossi, 2004). A low refrigerant charge in the system may be due to a refrigerant leak or improper charging during system installation. While the most common concern about a refrigerant leak is that a greenhouse gas has been released to the atmosphere, the greater impact is caused by the additional CO_2 emissions from a fossil fuel power plant due to a lowered air-conditioner (AC) efficiency.

Proctor's survey shows a correlation between the quality of installation and a technician's training and supervision. As is no surprise, proper training of the technician is the condition sine qua non for proper installation. But the survey also showed clearly that the number of return calls to correct improper installation was lowest when routine oversight of the installation work was provided, and that the number of faulty installations markedly increased when post-installation inspection visits were eliminated. At present, the homeowner has no quality assurance method for equipment installation as long as his/her comfort is not compromised.

The goal of this project is to study and develop fault detection and diagnostic (FDD) methods which could provide a technician with a fault diagnosis and could alert a homeowner when performance of his AC unit falls below the expected range, either during commissioning or post-commissioning operation. For the homeowner, this FDD capability could be incorporated into a future smart thermostat in the form of a readout to provide basic oversight of the service done on the unit and of its performance.

The benefits of fault detection and diagnosis (FDD) methods for ACs and HPs are numerous, and they include;
- reduction of energy use
- reduction in peak demand of electricity
- reduction in CO_2 emissions from fossil fuel power plants
- reduction in refrigerant emissions from AC and HP systems
- improvement of thermal comfort
- reduction in down time and maintenance cost

Fault detection and diagnosis is accomplished by comparing a system's current performance or features with those expected based on the measurements taken from the system when it was known to operate fault-free. FDD method development includes a laboratory phase during which fault-free and faulty

operations are mapped, and an analytical phase during which FDD algorithms are formulated. Kim et al. (2006) documented performance of the cooling mode fault-free and faulty heat pump operation, while this report describes the development of FDD concepts and their analytical implementation.

CHAPTER 2. OVERVIEW OF FAULT DETECTION AND DIAGNOSIS

2.1 Concept of Fault Detection and Diagnosis

Generally, a fault is a defect or condition that prevents the system from performing as intended. For a heat pump, a fault will result in degraded system capacity or efficiency, or both. The use of computers and microprocessors permits the application of FDD methods, which results in an earlier detection of faults than is possible by limit and trend checks that can be implemented by a conventional controller.

Isermann (1984) outlined a supervision loop for model-based FDD adopted in this study, shown in Figure 2.1. Once a fault is observed, the fault detection module produces a fault message and activates a fault diagnosis module, which identifies the cause of the fault and its location. Then, the identified fault is evaluated in a fault evaluation module by the class of its hazardous effect. Eventually, the decision module will decide the proper maintenance needed based upon economic considerations. After all the processes have been executed, the supervision process is reinitialized. The two modules of fault detection and diagnosis are typically combined and referred to as an FDD module.
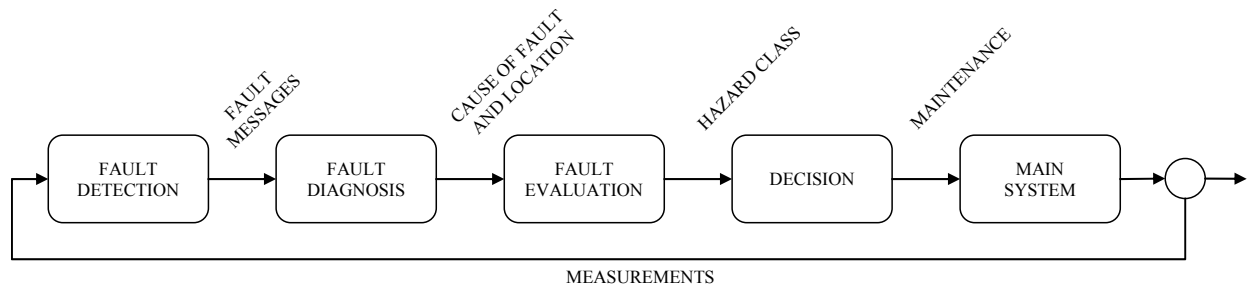
Figure 2.1. Supervision loop for fault detection and diagnosis (Isermann, 1984)

Figure 2.2 shows a detailed FDD procedure for a vapor compression system. System parameter measurements are first filtered through a steady-state detector to remove transient variation and external noise. The filtered data are converted into a variety of useful parameters such as EER, cooling capacity, flow rate, etc., using semi-physical derivations. Here, energy balance evaluations or manufacturer's formulations are utilized. Also from the filtered data, external parameters such as indoor and outdoor temperatures - called independent variables - are measured to determine the status of the system. These are used by the preprocessor to estimate the expected performance parameters - called features - using a no-fault, steady-state system model. The fault classifier analyzes and identifies the fault. The diagnostic result is evaluated by a decision module, which recommends a corrective reaction and communicates it to another authority.
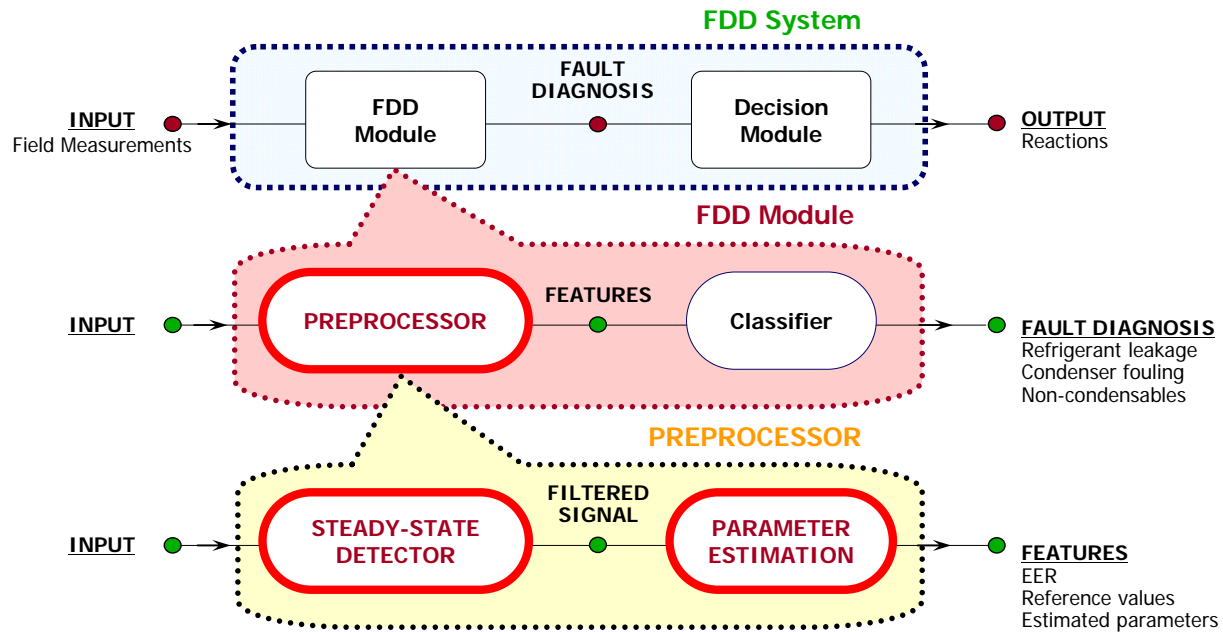
Figure 2.2. Equipment supervision for fault detection and diagnosis of a vapor compression system

Isermann's supervision loop differentiates fault detection from fault diagnosis, although both concepts originated from pattern recognition theories. Fault detection classifies the system status into two categories; no-fault and fault. When the FDD module diagnoses the system as being fault-free, the supervision process starts over. When the system is diagnosed as being faulty, the fault diagnostic classifier analyzes the system status in more detail to identify any on-going faults.

Sometimes the procedures of fault detection and fault diagnosis are unified in one step. Stylianou (1997) classified the status of a 5-ton commercial reciprocating chiller into one of five classes; a normal class and four fault classes. Stylianou applied a Bayesian decision rule and statistical training data to derive a family of classification functions.

2.2 Previous Research

A variety of FDD studies have been performed for HVAC systems. Since the automation of HVAC systems is strongly connected with building management systems, initial FDD studies were performed for whole HVAC systems and not discrete components (Anderson et al., 1989; Pape et al. 1991; Norford and Little, 1993; Lee et al., 1996a; Lee et al., 1996b; Peitsman and Bakker, 1996). Many of the studies were related to variable-air-volume (VAV) air-handling units. During the development of the first FDD techniques for large HVAC systems, energy savings was a secondary consideration to preventing equipment malfunction.

Even though there is a large body of literature on FDD applications for HVAC systems, relatively few publications exist for monitoring performance of residential vapor compression heat pumps. Grimmelius (1995) developed an on-line failure diagnosis method for a vapor compression refrigeration system. He established a symptom matrix based on the combination of casual analysis, expert knowledge, and simulated failure modes. He suggested using fuzzy logic for a real-time recognition of the failure mode. The author built a reference model based on a simple regression analysis and commented on the need to develop more general techniques for reference state estimation.

Stylianou and Nikanpour (1996) presented an FDD methodology for a reciprocating chiller using thermodynamic modeling, pattern recognition, and expert knowledge. The authors suggested three fault detection modules for off-cycle, start-up, and steady-state operations. In the off-cycle module, the authors estimated a temperature decay period, which activated FDD for sensor failure or drift. In the steady-state module, they estimated COP and capacity using a semi-empirical chiller model, which was then applied to fault detection. In order to isolate a fault, a rule-based fault pattern table was applied. In a successive investigation, Stylianou (1997) presented a fault diagnostic methodology using a statistical pattern recognition algorithm (SPRA) based on a Bayesian decision rule. The SPRA assigned different faults and a no-fault status to a set of five classes. The five classes were allocated equal probability, which biased the fault results more often than no-fault results. By shifting the scores of the classification functions, the bias impact was reduced.

Rossi and Braun (1997) developed a statistical FDD method for a roof-top air conditioner. The FDD system operated with seven representative temperature measurements. The residual values were used as performance indices for both fault detection and diagnosis. The residuals of seven FDD features were assumed to obey a Gaussian distribution. Statistical properties of the residuals for current and normal operation were used to classify the current operation as faulty or normal. The authors created a fault detection classifier module based on a Bayesian decision rule, which was optimized by minimizing the classification error. Once the system was suspected to have a fault, a fault diagnostic classifier was activated. A rule-based pattern chart which consists of the direction of residual change was used as an indication of fault symptoms. The fault diagnostic classifier module was devised assuming individual features as a series of independent probabilistic accidents. Since fault detection and fault diagnosis were running as independent modules, the fault diagnostic classifier functioned isolated from the detection module. Five types of faults could be distinguished from the diagnosis.

Breuker and Braun (1998a) surveyed frequently occurring faults for a packaged air conditioner. Based on field data, they sorted field faults into three different categories according to the cause of the fault, service frequency, and service cost. With respect to the cause of the fault, system shutdown failures were caused by electrical or control problems approximately 40 % of the time and mechanical problems approximately 60 % of the time. When sorted by service frequency, refrigerant leakage occurred most frequently, followed by condenser, air handler, evaporator, and compressor faults. When sorted by service cost, compressor failure contributed 24 % of total service costs. Control related faults contributed 10 % of total service costs.

Breuker and Braun (1998b) performed steady-state and transient tests on a packaged air conditioner and described an overall procedure to develop an FDD system. The authors developed no-fault steady-state models using polynomial representations. They introduced five types of faults with different levels. The impacts of steady-state detector threshold, detection error safety factor, and fault decision threshold were evaluated.

Chen and Braun (2001) developed a simplified FDD method for a 5-ton rooftop air conditioner with a thermostatic expansion valve (TXV). They modified an FDD technique by simplifying Rossi and Braun's method (1997). They used measurements and model predictions of temperatures for fault-free system operation to compute ratios sensitive to individual faults. The authors selected the two most sensitive measurements and developed a simple rule-based FDD algorithm. The FDD algorithm was based on sequential rules comparing the sensitivity of residuals organized within a fault characteristic chart.

Castro (2002) applied a k-nearest neighbor and k-nearest prototype method for fault detection of a chiller. The author calculated Euclidean distances for the current state based on the selected two largest residuals, and estimated the possibility of a fault from the distance information. In this research, the software MATCH was developed as a tool for the controls package to combine monitoring, fault detection, and diagnostic features. After detecting faults, data were input to the rule-based fault diagnosis algorithm. Castro preferred the nearest prototype classifier since the nearest neighbor classifier is more computationally intensive.

Comstock and Braun (2001) tested eight common faults in a 316 kW (90 ton) centrifugal chiller to identify the sensitivity of different measurements to the faults. The eight faults considered in the study were selected through a fault survey among major American chiller manufacturers. The fault testing led to a set of generic rules for the impacts of faults on measurements used for FDD. The impact of faults on cooling capacity and coefficient of performance was also evaluated.

Smith and Braun (2003) performed field-site tests of more than 20 units to identify local installation and operation problems. Using an 11 kW rooftop unit with a fixed orifice expansion device and a 18 kW unit with a TXV, they proposed a decoupling-based unified FDD technique to handle multiple simultaneous faults. Li (2004) re-examined the statistical rule-based method initially formulated by Rossi and Braun (1997) and presented two additional FDD schemes, which improved the sensitivity of the FDD module. He also developed virtual sensors to estimate characteristic parameters from indirect component modeling. For a reference model, Li combined a multivariate polynomial model and generalized regressive neural network (GRNN).

Kim and Kim (2005) tested a water-to-water heat pump system with a variable-speed compressor and an electrical expansion valve (EEV). They found the system parameters to be less sensitive to faults compared to a constant-speed compressor system. They reported that the control of compressor speed reduced the fault sensitivity of the system. They also developed an FDD algorithm along with two different rule-based charts that depended on the compressor status. The authors suggested that COP degradation due to a fault is much more severe with a variable-speed compressor than with a constant-speed compressor.

Navarro-Esbri et al. (2007) developed an adaptive Kalman filter/forgetting-factor based algorithm applied as a refrigerant charge leak detector for a breadboarded water-to-water chiller. Compressor rotation speed, suction refrigerant vapor superheat and suction pressure were the most sensitive variables to refrigerant charge. Proper experimental tuning of the forgetting-factor allowed this algorithm to immediately detect refrigerant charge leakage. This is very promising considering other investigators have noted difficulty in reliably detecting an undercharged condition until a fault level of at least 40 % lost refrigerant charge (Breuker and Braun 1998b, Stylianou and Nikanpour 1996).

The works cited above are summarized in Table 2.1. The investigators have extended previously known techniques and added unique FDD components to these varying system installations. The rule-based chart method based upon application of statistical methods was shown by several investigations to be very effective and adaptable. This is one reason this method has been adapted for use in the present work.

Table 2.1. Summary of system types and FDD methodology for selected previous investigations

System types	FDD methodology
VAV air-handling units and whole building system	Component FDD and black box model FDD
Vapor compression refrigeration system	Symptom matrix with expert system decision making algorithm (IF..THEN..ELSE).
Reciprocating chiller	Off, Start, and Steady FDD
Rooftop AC w/ orifice	Feature residual, rule-chart FDD based upon statistical method
Packaged AC	Five faults, FDD with steady-state detector
Rooftop with TXV	Ratios sensitive to certain faults were identified and a rule-based chart FDD scheme was used
Centrifugal chiller	Residuals calculated and k-nearest neighbor method used for FDD
Centrifugal chiller	Eight faults and impacts of faults on efficiency were studied
Rooftop unit w/ TXV	FDD with virtual sensors, polynomial and neural network reference model
Variable speed, mini split AC	Rule-based chart FDD
Small breadboard chiller	Fast detection of charge loss

CHAPTER 3. STEADY-STATE DETECTOR

In this study, we envision the fault detection and diagnosis (FDD) process to be performed every time the system is in steady state. For this reason, identification of the steady state is an important task in our FDD analysis. Some of the first investigations of system steady-state identification came from process control field studies including model development, optimization, fault detection, and control (Mahuli et al., 1992, Cao and Rhinehart, 1995, Jiang et al. 2003). Steady state can be detected by observing global system characteristics, e.g., capacity, or – more simply – by monitoring selected parameters. If the only goal was to check system performance, providing enough time to reach steady-state capacity and power input could be a sufficient approach. However, reaching steady capacity would not guarantee the actual steady-state of all parameters used in a particular FDD scheme.

In previous investigations within the HVAC field, several investigators suggested steady-state identification techniques for FDD purposes (Glass et al., 1995, Rossi, 1995, Breuker and Braun, 1998a, Li, 2004). Since the goal of these investigations was mainly fault detection, the evaluation of the steady-state detectors was not performed in detail. In this investigation, a moving window steady-state detector was evaluated and optimized. A systematic methodology to design a steady-state detector is provided below.

3.1 A Moving Window for Steady-State Detection

The concept of the steady-state detector originates from noise filter theory. When a system is not steady, thermodynamic system parameters are highly unstable. The variance, or standard deviation, of important parameters is typically utilized to indicate the statistical spread within the data distribution and can be used to characterize random variation of the measured signals.

The most common and simple steady-state detectors analyze data over a predefined moving window, as illustrated in Figure 3.1. A predefined time interval is established over which important parameters are sampled at regular intervals. This produces an array of system parameters that are continuously updated and held in memory. Since a moving window replaces each data point within the timespan, the moving window average is equivalent to a low-pass filter.
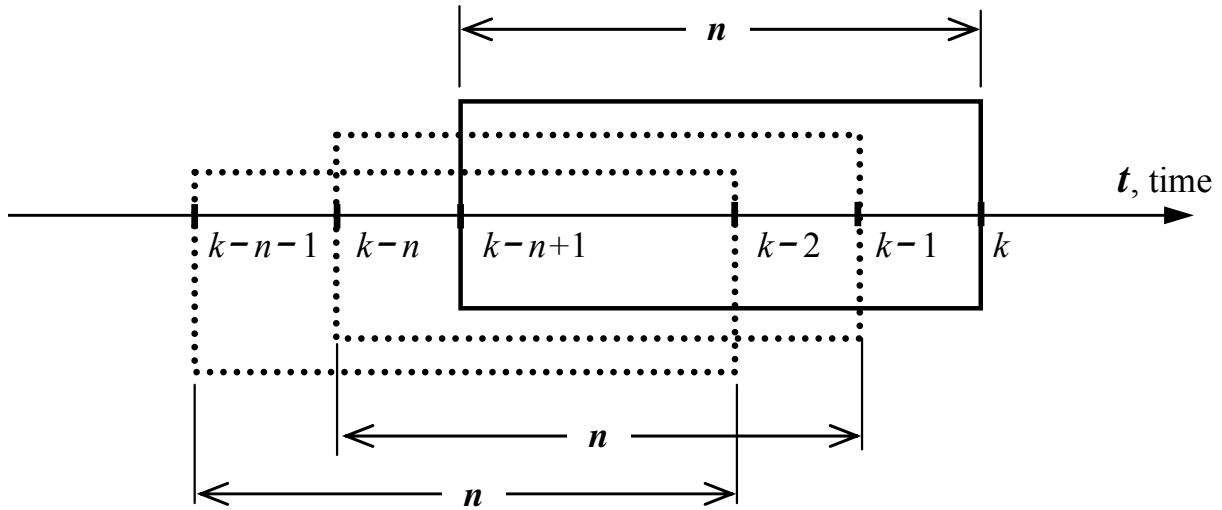
Figure 3.1. Moving windows of n data points at k^{th} time

Several methods of steady state detection were investigated by other researchers. Glass et al. (1995) formulated a steady-state detector using a geometrically weighted running method. In this method, the old data are exponentially and automatically attenuated through multiplication with a "forgetting factor", which is based upon a system transition time constant. Some FDD investigations of vapor compression systems applied this method (Rossi 1995, Breuker and Braun 1998b). Equations 3.1 and 3.2 denote geometrically weighted average and geometrically weighted variance, respectively. Geometrically weighted average and variance may have different weights.

$$\overline{x_n}(\alpha) = \frac{\sum_{k=0}^{n} \alpha^{n-k} x_k}{\sum_{k=0}^{n} \alpha^{n-k}} \tag{3.1}$$

$$v_n = \frac{\sum_{k=0}^{n} \alpha^{n-k} (x_k - \overline{x_n}(\alpha))^2}{\sum_{k=0}^{n} \alpha^{n-k}} \tag{3.2}$$

The geometric weighting factor, α is calculated as in Equation 3.3 and has a value between 0 and 1. In this equation, τ_{ss} is a time constant and Δt is a time increment between measurements.

$$\alpha = \frac{\tau_{ss}}{\tau_{ss} + \Delta t} \tag{3.3}$$

Li (2004) utilized moving window slopes and variances of evaporator exit superheat and liquid line subcooling as the key parameters of the steady-state detector in his FDD research on roof-top air conditioners.

In our study the moving window standard deviation calculated for an optimized moving window size with defined feature thresholds indicates the steady state of the heat pump. The steady-state detector calculates standard deviation of parameters in a recursive fashion. Suppose that at any instant k, the average of the latest n samples of a data sequence, x_i, is given by,

$$\overline{x}_k = \frac{1}{n} \sum_{i=k-n+1}^{k} x_i \tag{3.4}$$

A difference between two averages of the latest n samples at the current time, k, and at the previous time instant, $k-1$, is,

$$\overline{x}_k - \overline{x}_{k-1} = \frac{1}{n} \left[\sum_{i=k-n+1}^{k} x_i - \sum_{i=k-n}^{k-1} x_i \right] = \frac{1}{n} \left[x_k - x_{k-n} \right] \tag{3.5}$$

Rearranged, the current average is calculated by,

$$\overline{x}_k = \overline{x}_{k-1} + \frac{1}{n} \left(x_k - x_{k-n} \right) \tag{3.6}$$

This approach is known as a moving window average because the average at each kth instant is based on the most recent set of n values. In other words, at any instant, a moving window of n values is used to calculate the average of the next data sequence. A moving window variance can be defined similarly.

$$v_k = \frac{1}{n} \sum_{i=k-n+1}^{k} \left(x_i - \overline{x}_k \right)^2 = \frac{1}{n} \sum_{i=k-n+1}^{k} x_i^2 - \overline{x}_k^2 . \tag{3.7}$$

$$v_k = v_{k-1} + \frac{1}{n} \left(x_k^2 - x_{k-n}^2 \right) - \left(\overline{x}_k^2 - \overline{x}_{k-1}^2 \right) \tag{3.8}$$

The moving window standard deviation is then given as

$$\sigma_k = \sqrt{v_k} \tag{3.9}$$

The steady-state detector identifies steady operation if the standard deviations for the selected features representing the status of the system fall below a predefined threshold.

3.2 Development of the Steady-State Detector

3.2.1 Experimental setup and conditions

The studied system was an R410A, 8.8 kW (2.5 ton) split residential heat pump with Seasonal Energy Efficiency Ratio (SEER) of 13 (ARI, 2006). The unit consisted of an indoor fan-coil section, outdoor section with a scroll compressor, cooling mode and heating mode thermostatic expansion valves (TXV), and connecting tubing. Both the indoor and outdoor air-to-refrigerant heat exchangers were of the finned-tube type. The unit was installed in environmental chambers and charged with refrigerant according to the manufacturer's specifications. Figure 3.2 shows a schematic of the experimental setup indicating the measurement locations of temperature, pressure, and mass flow rate. On the refrigerant side, pressure transducers and T-type thermocouple probes were attached at the inlet and exit of every component of the system. The refrigerant mass flow rate was measured using a Coriolis flow meter. The air enthalpy method served as the primary measurement of the system capacity, and the refrigerant enthalpy method served as the secondary measurement. These two measurements always agreed within 5 %. Table 3.1 lists uncertainties of the major quantities measured during this work. Detailed specification of the test rig including indoor ductwork, dimensions, data acquisition, measurement uncertainty, and instrumentation is described in Kim et al. (2006).
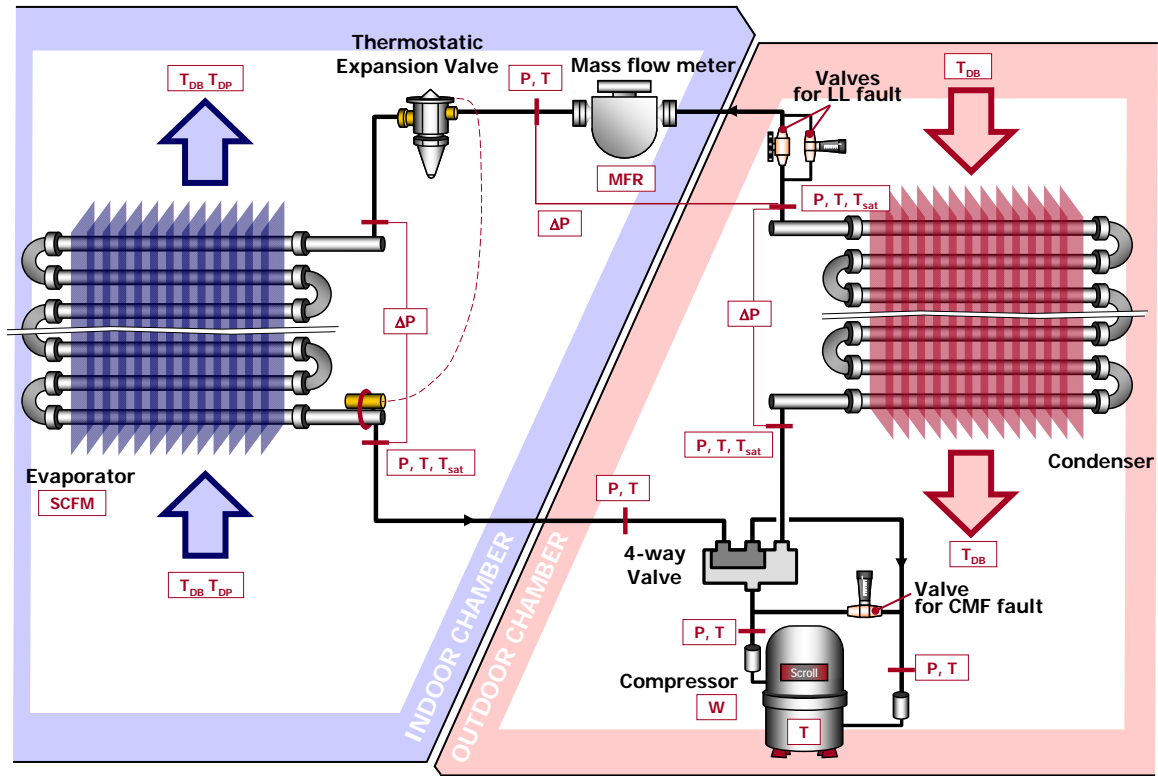
Figure 3.2. Schematic diagram of the experimental setup

Table 3.1. Measurement uncertainties

Measurement	Range	Uncertainty at the 95 % Confidence Level
Individual Temperature	-18 °C to 93 °C	±0.3 °C
Temperature Difference	0 °C to 28 °C	±0.3 °C
Air Nozzle Pressure	0 Pa to 1245 Pa	±1.0 Pa
Refrigerant Mass Flow Rate	0 kg/h to 544 kg/h	±1.0 %
Dew point Temperature	-18 °C to 38 °C	±0.4 °C
Dry-Bulb Temperature	-18 °C to 40 °C	±0.4 °C
Total Cooling Capacity	3 kW to 11 kW	±4.0 %
COP	2.5 to 6.0	±5.5 %

3.2.2 Selection of measurement features

Table 3.2 shows system features used in fault detection. In this laboratory study, we measured pressure at the exits of the evaporator and the condenser to obtain T_E and T_C, respectively. The obtained pressures were converted into saturation temperatures using REFPROP 7 (Lemmon et al., 1998). For the other five features, T-type thermocouples were used.

Table 3.2. System features used in fault detection

Independent Features		Dependent Features	
Outdoor dry-bulb temperature	T_{OD}	Evaporator exit refrigerant saturation temperature	T_E
Indoor dry-bulb temperature	T_{ID}	Evaporator exit refrigerant superheat	T_{sh}
Indoor dew point temperature	T_{IDP}	Condenser inlet refrigerant saturation temperature	T_C
		Compressor discharge refrigerant temperature	T_D
		Condenser exit liquid line refrigerant subcooled temperature	T_{sc}
		Evaporator air temperature change	ΔT_{EA}
		Condenser air temperature change	ΔT_{CA}

3.2.3 Setting feature thresholds based upon steady-state data

The threshold of each feature that bounds the steady-state signal is an important parameter in determining the performance of a steady-state detector. The smaller a threshold is, the more sensitive an FDD module is because steady state is more conservatively identified. However, if a threshold is too small, it takes more time for the given feature to settle within its threshold range. Also, an excessively small threshold value may inhibit the functioning of the steady-state detector when operating in the field. Large thresholds allow faster data collection but carry a risk of including some transient data, which decreases the performance of an FDD system. Therefore, the thresholds must be selected to both minimize the inclusion of non-steady-state data and maximize the recognition of steady state.

To determine the thresholds, we collected steady-state data over 60 minutes commencing 3 hours after startup at fixed chamber conditions and calculated the standard deviations, σ, for all seven features. As an example, Figure 3.3 shows the variation and standard deviation of the steady-state data for all features, and Table 3.3 summarizes the ranges and standard deviations of all seven features. Since the system operated under stable conditions, the standard deviations and ranges in Table 3.3 are small. As expected, superheat shows the largest fluctuation.
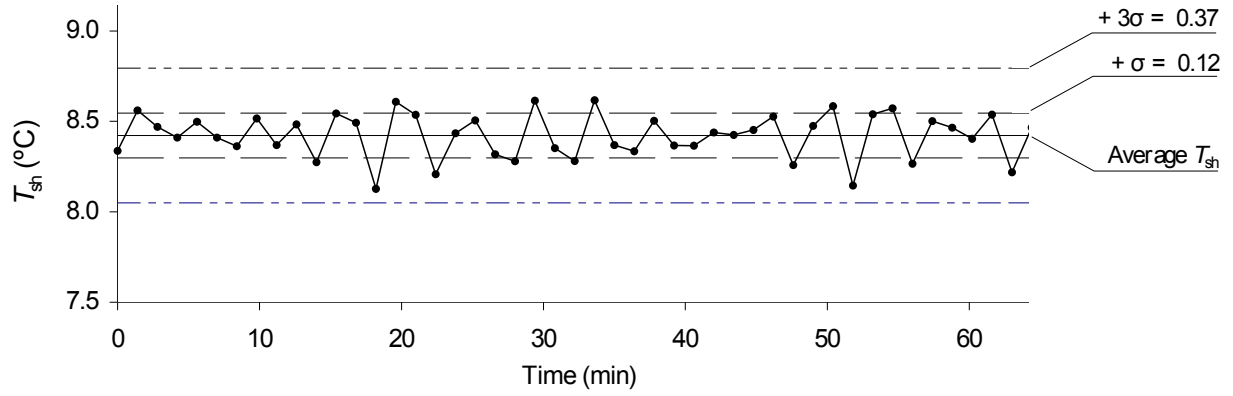
Figure 3.3(a). Variation of superheat (T_{ID} = 26.7±0.5 °C; T_{OD} = 27.8±0.5 °C)
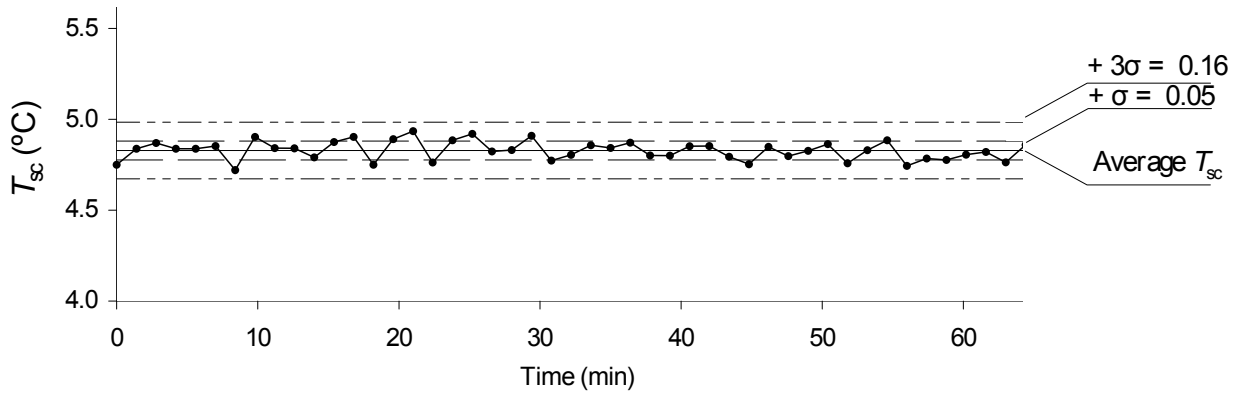
Figure 3.3(b). Variation of subcooling (T_{ID} = 26.7±0.5 °C; T_{OD} = 27.8±0.5 °C)
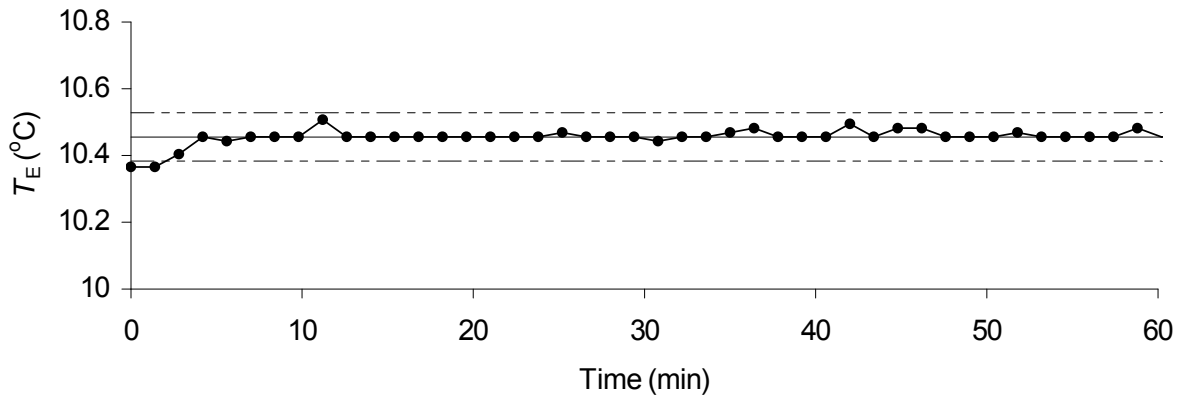
Figure 3.3(c). Variation of evaporator saturation temperature (T_{ID} = 26.7±0.5 °C; T_{OD} = 27.8±0.5 °C)
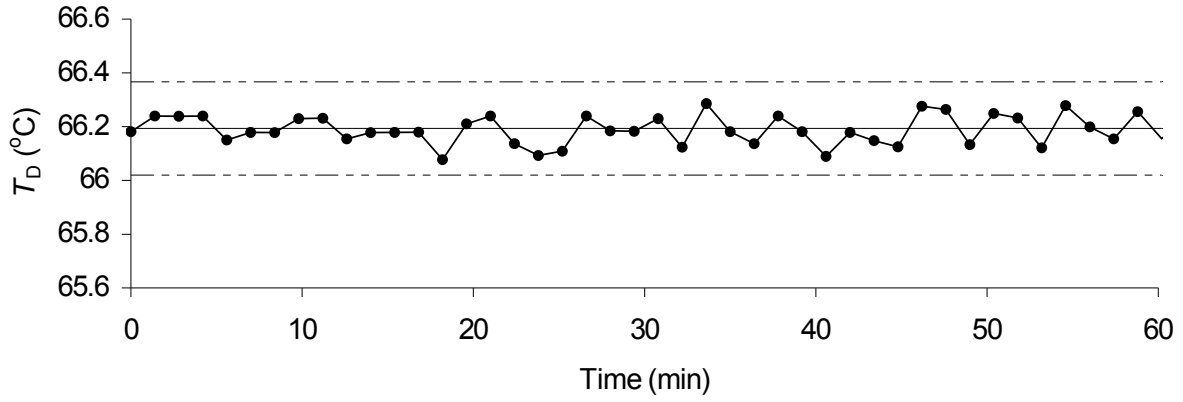
Figure 3.3(d). Variation of compressor discharge temperature (T_{ID} = 26.7±0.5 °C; T_{OD} = 27.8±0.5 °C)
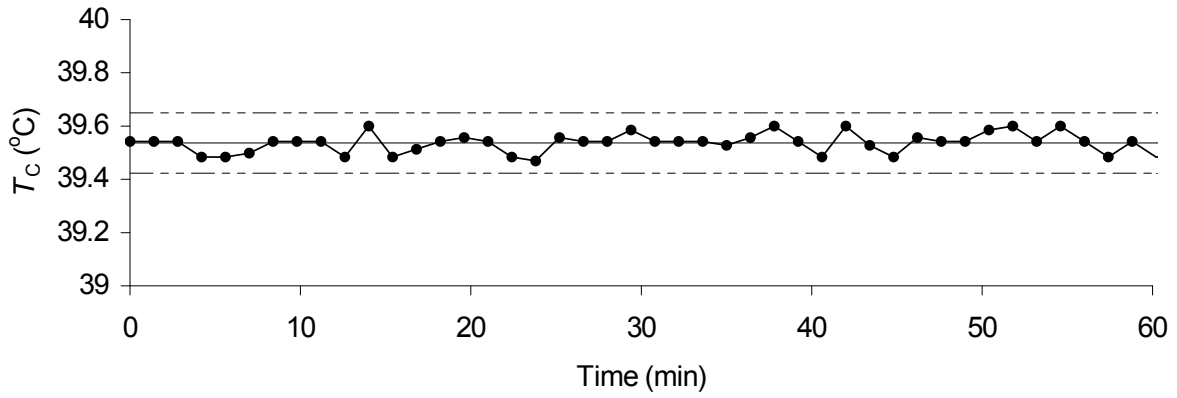
Figure 3.3(e). Variation of condenser saturation temperature (T_{ID} = 26.7±0.5 °C; T_{OD} = 27.8±0.5 °C)
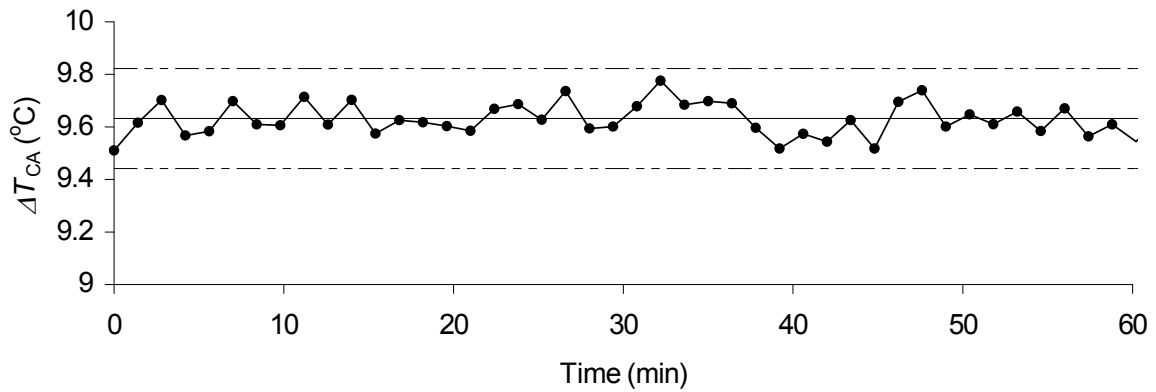
Figure 3.3(f). Variation of air temperature increase through condenser (T_{ID} = 26.7±0.5 °C; T_{OD} = 27.8±0.5 °C)

14
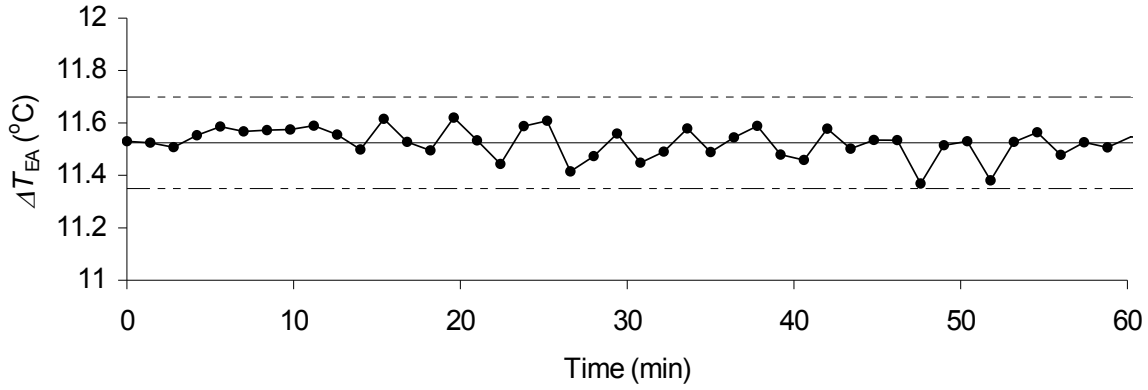
Figure 3.3(g). Variation of air temperature drop through evaporator (T_{ID} = 26.7±0.5 °C;

T_{OD} = 27.8±0.5 °C)

Table 3.3. Variations of selected features during steady state

Features	T_{sh}	T_{sc}	T_E	T_D	T_C	ΔT_{CA}	ΔT_{EA}
Range* (°C)	0.49	0.22	0.14	0.25	0.17	0.27	0.25
Standard deviation, σ (°C)	0.124	0.052	0.024	0.058	0.035	0.063	0.058
Calculated thresholds, 3σ (°C)	0.37	0.16	0.07	0.17	0.11	0.19	0.17

* Difference between the maximum and minimum value

3.2.4 Selection of moving window size using startup transient tests

Figures 3.4, 3.5, and 3.6, presented in this section, were derived from the same startup transient test. Figure 3.4 displays variation of the seven features in the post-startup period. The figure demonstrates that T_{sh} and T_{sc} fluctuate the most and are the dominant indicators of system instability during startup. Figure 3.5(a) further examines fluctuations of T_{sh} and T_{sc} showing them with ±3σ thresholds superimposed (these thresholds were presented in Figure 3.3). The vertical dashed line extending to Figures 3.5(b) and 3.5(c) indicates the onset of steady state at approximately 6 minutes and 30 seconds. From this point in time and on, the values of both features are retained within their respective ±3σ thresholds.

While Figure 3.5(a) convincingly shows us, based on individual measurements, that steady state was attained at 6 minutes and 30 seconds after the startup, we must realize that we could make this determination only after extending the data collection much further in time beyond 6 minutes and 30 seconds to be able to calculate T_{sh} and T_{sc} mean values for steady-state operation. For this reason, using individual feature measurements for steady state indication proves not to be a robust approach, and it is rather attractive to base a steady-state detector on some statistical quantity based upon measurements taken within a predefined moving time window. In this study we applied the ±3σ steady-state thresholds and standard deviations of moving-window-measured T_{sh} and T_{sc} values, $\sigma_{MW}(T_{sh})$ and $\sigma_{MW}(T_{sc})$, for steady-state detection during the startup transient.

15
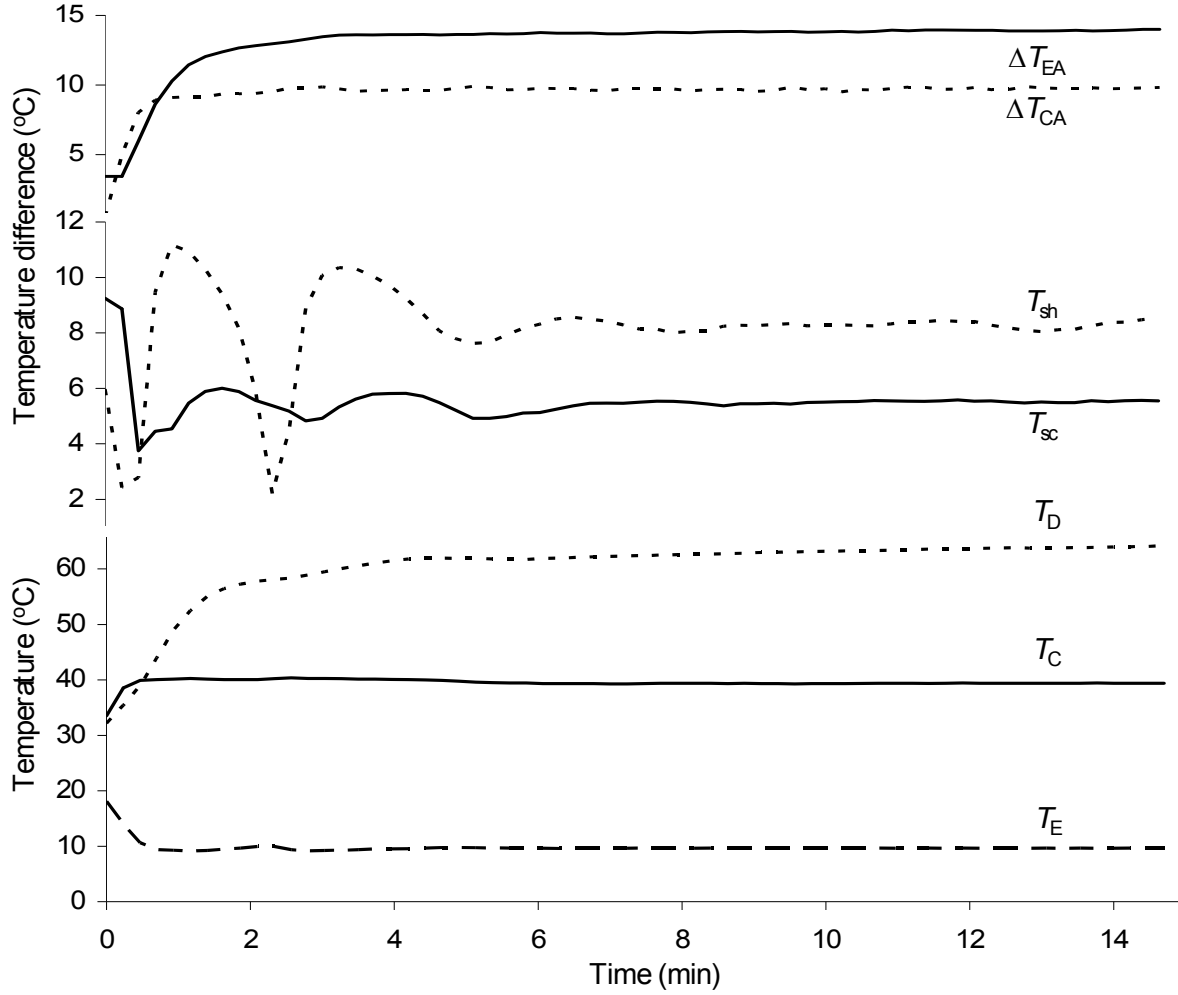
Figure 3.4. Variation of seven features during a startup transient, $T_{ID} = (26.7\pm0.5)°C$, $T_{OD} = (27.8\pm0.5)°C$

Figures 3.5(b) and 3.5(c) explain the procedure we used to determine the size of the moving window by showing T_{sh} and T_{sc} standard deviations, $\sigma_{MW}(T_{sh})$ and $\sigma_{MW}(T_{sc})$, respectively, for three windows sizes with a sample period of 14 seconds/sample: 70 seconds (MW70s), 140 seconds (MW140s), and 210 seconds (MW210s). It is our interest to establish the minimum window size for which the calculated $\sigma_{MW}(T_{sh})$ and $\sigma_{MW}(T_{sc})$ are below their respective threshold values past the onset of steady state, which is shown in Figure 3.5 to occur at 6 minutes and 30 seconds after startup.
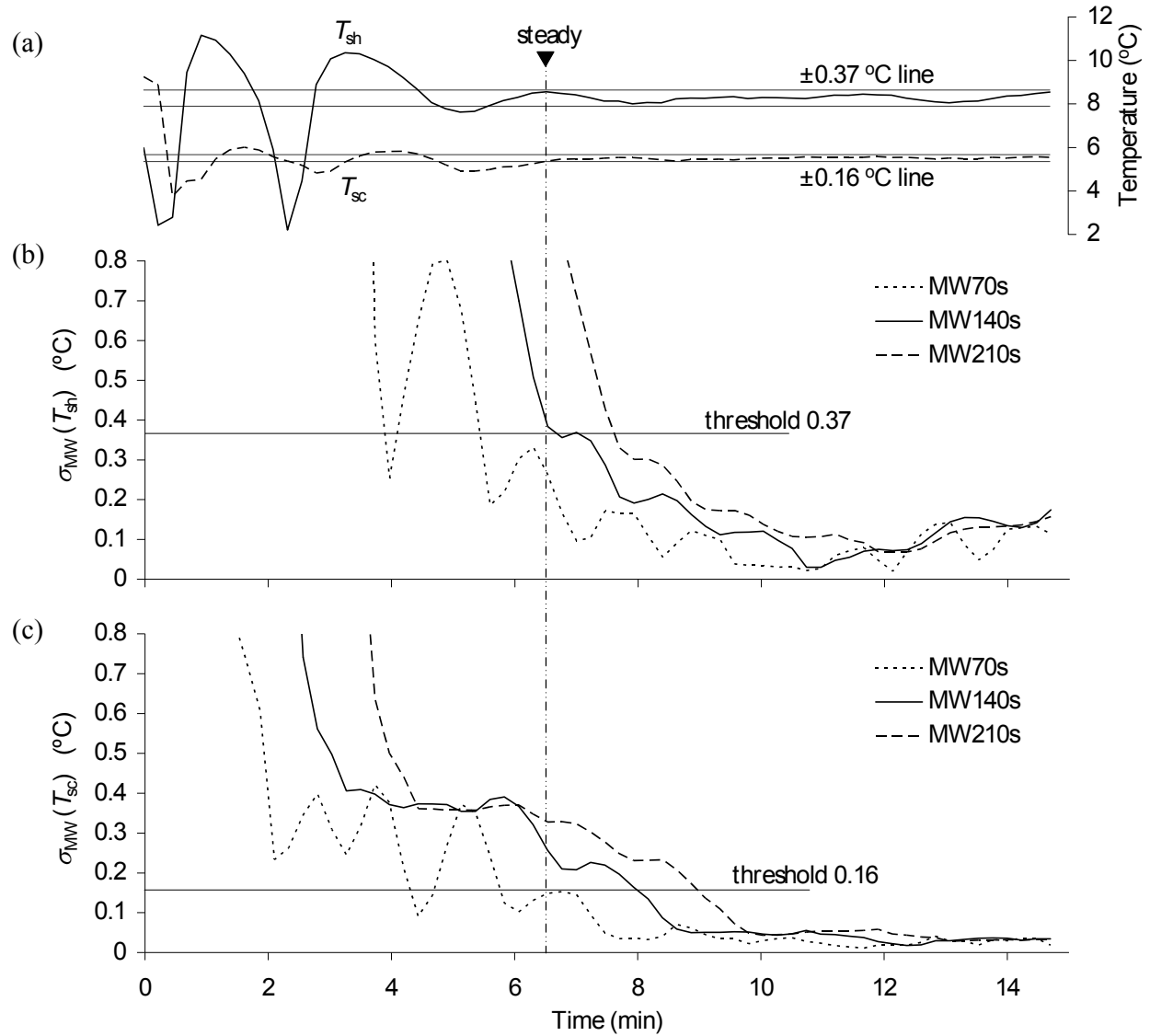
Figure 3.5. Onset of steady state during a no-fault startup transient test, $T_{ID} = (26.7 \pm 0.5)°C$, $T_{OD} = (27.8 \pm 0.5)°C$; (a) Decision on steady state; (b) $\sigma_{MW}(T_{sh})$; (c) $\sigma_{MW}(T_{sc})$

The general procedure for determining the minimum moving window size, illustrated in Figure 3.5, is as follows:

1. Collect selected feature data during the start-up period for at least 30 samples into the steady-state region at a sampling rate equal to the sampling rate used for steady-state sampling. The steady-state region is defined here to occur when the instantaneous values of the selected features fluctuate within $\pm 3\sigma$ of their steady-state mean values, as determined in Figure 3.3. The dashed vertical line in Figure 3.5(a) illustrates this onset of steady-state using the two most fluctuating FDD features during the startup, T_{sh} and T_{sc}.

2. For all features, calculate the moving window standard deviation versus time for a range of moving window sample sizes, as presented in Figures 3.5(b) and 3.5(c) for T_{sh} and T_{sc}.

3. The moving window size that results in *all* features' standard deviations *crossing* and *remaining* within the $\pm 3\sigma$ threshold *after* steady-state is attained (as defined in Step 1), is the minimum acceptable moving window size.

17

The minimum acceptable moving window size (and thus sample size for our sampling rate) is determined by plotting the moving window standard deviations as a function of time for all features used in the FDD algorithm. In our case the last two features to vary within their $\pm 3\sigma$ thresholds, of all the features listed in Table 3.3, were T_{sc} and T_{sh}. The moving window standard deviations of T_{sh} and T_{sc} ($\sigma_{MW}(T_{sh})$ and $\sigma_{MW}(T_{sc})$) are plotted as a function of time in Figures 3.5(b) and 3.5(c) with the vertical steady-state line determined in Figure 3.5(a) extending down to indicate the onset time of steady-state.

Selecting the 70 second long moving window, MW70s, would not be appropriate because both $\sigma_{MW}(T_{sh})$ and $\sigma_{MW}(T_{sc})$ values calculated for this window size drop below the respective thresholds well before the onset of steady state at 6 minutes and 30 seconds. The MW140s appears to be a good selection because it produces standard deviations that remain below the steady-state threshold after the vertical steady-state line; with a few seconds past this instance for $\sigma_{MW}(T_{sh})$ and 90 seconds later for $\sigma_{MW}(T_{sc})$ at 8 minutes. Hence, MW140s would indicate the onset of steady state 90 seconds after it actually has occurred, but it would not provide a false indication of steady state at any time earlier because of the relatively smooth and oscillation-free character of $\sigma_{MW}(T_{sh})$ and $\sigma_{MW}(T_{sc})$ lines. For MW210s, steady-state detection was indicated at approximately 9 minutes with $\sigma_{MW}(T_{sh})$ being the defining factor; this moving window could be acceptable, but it is not the minimum moving window size to satisfy our steady-state criteria that all features remain within their $\pm 3\sigma$ thresholds.

In this startup test, we took measurements every 14 seconds. We should note that the data sampling rate (samples/s or Hz) should be based upon a Nyquist frequency (greater than twice the frequency of the most varying feature) (Franklin et al. 1991), as determined by the frequency of variation in the features important to the FDD algorithm. For this investigation, the heat pump features during steady-state varied at a maximum frequency well below 0.03 Hz. Sampling at greater than twice this frequency, or 1 sample every 16 seconds, would capture all the feature variations. The sample rate, fixed at 1 sample per 14 seconds, was sufficient to eliminate or greatly reduce the likelihood of signal measurement bias. A greater sampling rate could be desirable, but sampling at much greater than the Nyquist frequency gains no new information.

As defined by the $\pm 3\sigma$ steady-state threshold, the system was stable approximately 6 minutes and 30 seconds after startup; however, the discharge line wall temperature, T_D, continued to increase. Figure 3.6 shows that T_D increased by 2.1 °C for the remainder of the time shown in the figure while the evaporator capacity, Q_{EA}, increased by 1.3 % with no change in the condenser capacity, Q_{CA}. The unchanging value of Q_{CA} tends to indicate a thermal inertia effect for T_D. The slow increase, or drift, in this temperature does not preclude its use as a fault detection feature, however, it will result in a higher uncertainty for T_D within the system's steady-state no-fault reference model.
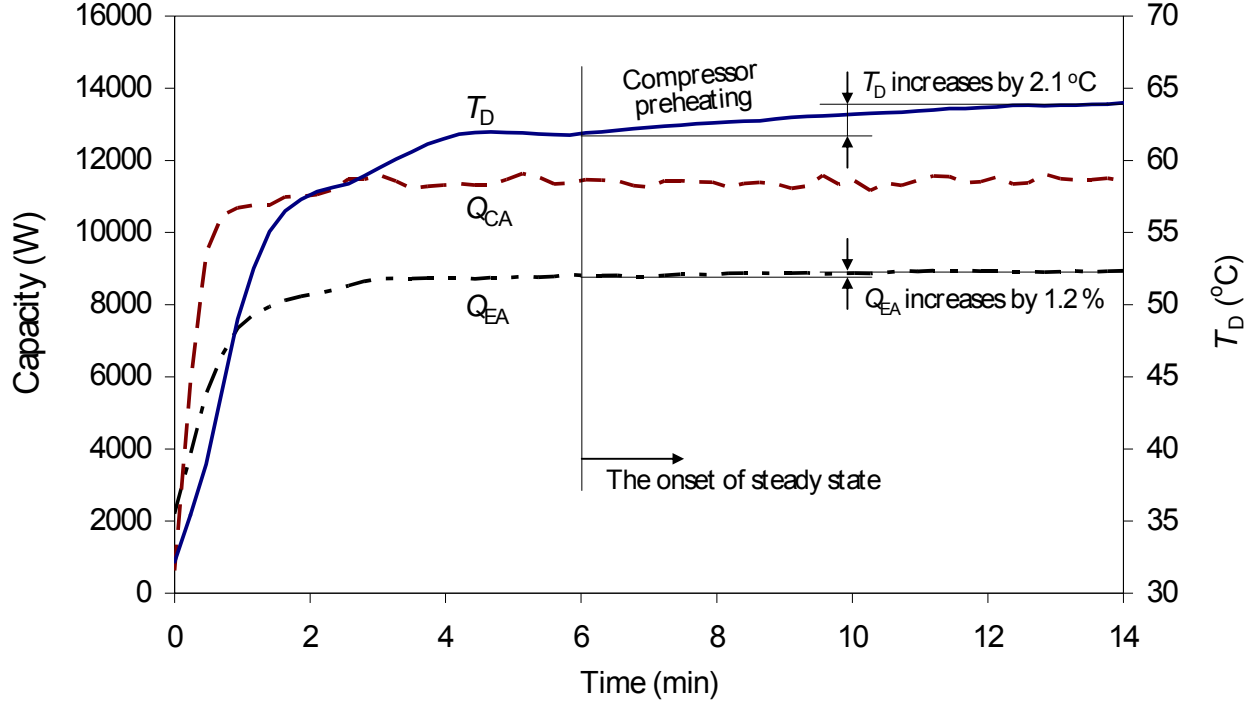
Figure 3.6. The startup transients of compressor discharge temperature and evaporator/condenser capacities, $T_{ID} = (26.7\pm0.5)°C$, $T_{OD} = (27.8\pm0.5)°C$

3.3 Verification of the Steady-State Detector Using an Indoor Load Change Test

3.3.1 Tests with no faults imposed

Figure 3.7 presents verification of the developed steady-state detection procedure during transients driven by changes in the indoor air temperature with no faults imposed. Stepped increases in T_{ID} in Figure 3.7(a) reflect the energizing of additional indoor chamber electric duct heaters. In addition to T_{ID}, the figure shows T_{sh}, T_{sc}, and standard deviations of T_{sh}, T_E and ΔT_{EA} for an 18 second sample interval and moving window sizes of 72 seconds (4 samples), 144 seconds (8 samples), and 216 seconds (12 samples). T_{sh}, T_{sc} and $\sigma_{MW}(T_{sh})$ are included because they were important during the startup transient. While T_{sh} shows some variation during an indoor load change test, T_{sc} is much more stable than during the startup transient.

The figures show two transient regions, which were identified using a 144 second moving window. The gray areas in the plots indicate transient regions for individual features as determined by the $\pm3\sigma$ threshold steady-state detector algorithm within a 144 seconds moving window. Figure 3.7(e) shows that ΔT_{EA} consistently indicates the beginning of the transient while Figure 3.7(d) shows that T_E indicates the end of the transient. The variation of T_{sh} in Figure 3.7(c) cannot filter out the whole transient region for all of these parameters. Instead, the variation of T_E and ΔT_{EA} in Figures 3.7(d) and 3.7(e) control the detection of steady state. Since the transients in Figure 3.7(a) are due to changes in T_{ID}, the features that characterize the evaporator (indoor coil), T_E and ΔT_{EA}, proved to be necessary for steady state detection.

19
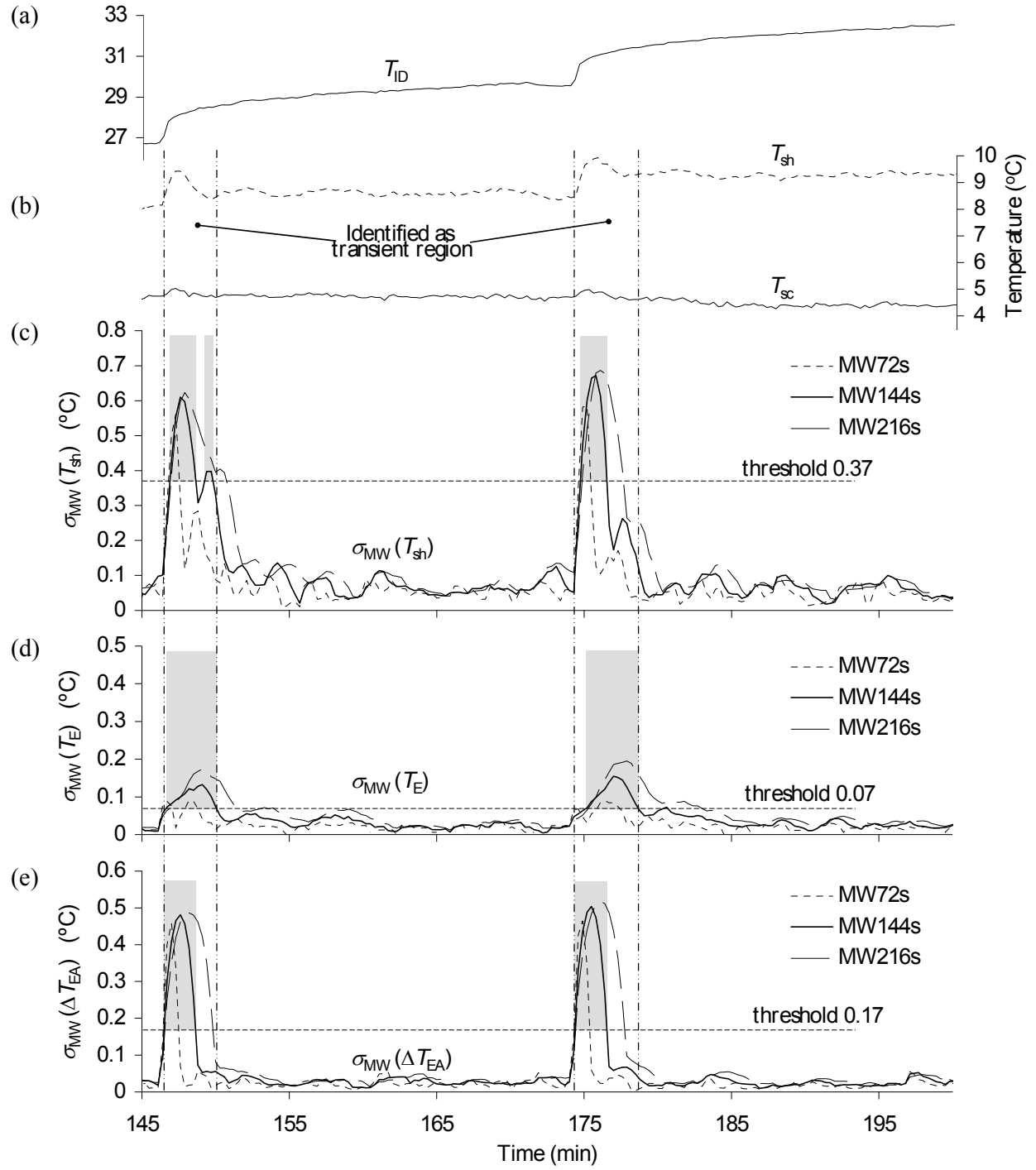
Figure 3.7. Identification of steady state during a no-fault indoor load change test, $T_{OD} = (35 \pm 0.5)°C$, (a) T_{ID}; (b) T_{sh} and T_{sc}; (c) $\sigma_{MW}(T_{sh})$; (d) $\sigma_{MW}(T_E)$; (e) $\sigma_{MW}(\Delta T_{EA})$

3.3.2 Test with a 20 % refrigerant undercharge fault

Since the goal of an FDD scheme is to detect a system fault, the steady-state detector must be able to identify steady state during a system's faulty operation. For this reason, we applied the developed steady-state detector during a test with changing indoor temperature with a 20 % refrigerant undercharge fault.

Figure 3.8 shows the selected system parameters and features during the 35 °C outdoor temperature test. The moving window sizes are 66 seconds (3 samples), 132 seconds (6 samples), and 198 seconds (8 samples) with a data sampling rate of 22 seconds. Figure 3.8(a) shows two rapid drops of T_{ID} due to turning off chamber electric duct heaters and a continuous decrease of T_{ID} due to chamber cooling by the tested system.

As during the fault-free indoor temperature change transient test, the change of $\sigma_{MW}(T_{sh})$ in Figure 3.8(c) is not large enough to filter out the transient state, but changes in $\sigma_{MW}(T_E)$ and $\sigma_{MW}(\Delta T_{EA})$, taken together, correctly identify steady state, as shown in Figures 3.8(d) and 3.8(e). Hence, the same features identified steady state during the undercharge fault and no-fault operations. Further, our review of transient data of the system operating under different faults indicated that the developed steady-state detector would work reliably with other faults as well.

3.4 Verification of the Steady-State Detector During a Startup Transient Test with a Fault Imposed

To verify the steady-state detector developed in this study, several startup transient tests were performed with evaporator and condenser faults imposed on the system. Operating conditions for all tests were (27.8±0.5) °C outdoor dry-bulb, (26.7±0.5) °C indoor dry-bulb, and indoor relative humidity of (50.0±1.0) %.

3.4.1 Test with condenser fault imposed

A condenser fault was imposed by blocking the condenser heat exchanger face area with paper from the bottom up. The fault level for this transient test was set at 30 % face area having no air flow. Figure 3.9 shows the variation of four features during the startup of the heat pump. Superheat and subcooling are shown in Figure 3.9(a). The standard deviation of T_{sh}, T_{sc}, T_E, and T_D in a 144 seconds (9 sample) moving window are shown in Figure 3.9 in sequence. T_{sh} and T_{sc} reach steady state 4 and 5 minutes after the system starts, but the compressor discharge temperature, T_D, continues to change thus delaying the beginning of steady state to 10 minutes. With the condenser air flow fault, the discharge pressure of this system is higher than that of the no-fault system; hence this causes the discharge temperature to be higher. The thermal inertia time constant for the discharge wall temperature results in T_D attaining steady state later than other features. This test shows that the steady-state detector still safely determines steady state even if the system has a condenser fouling fault.
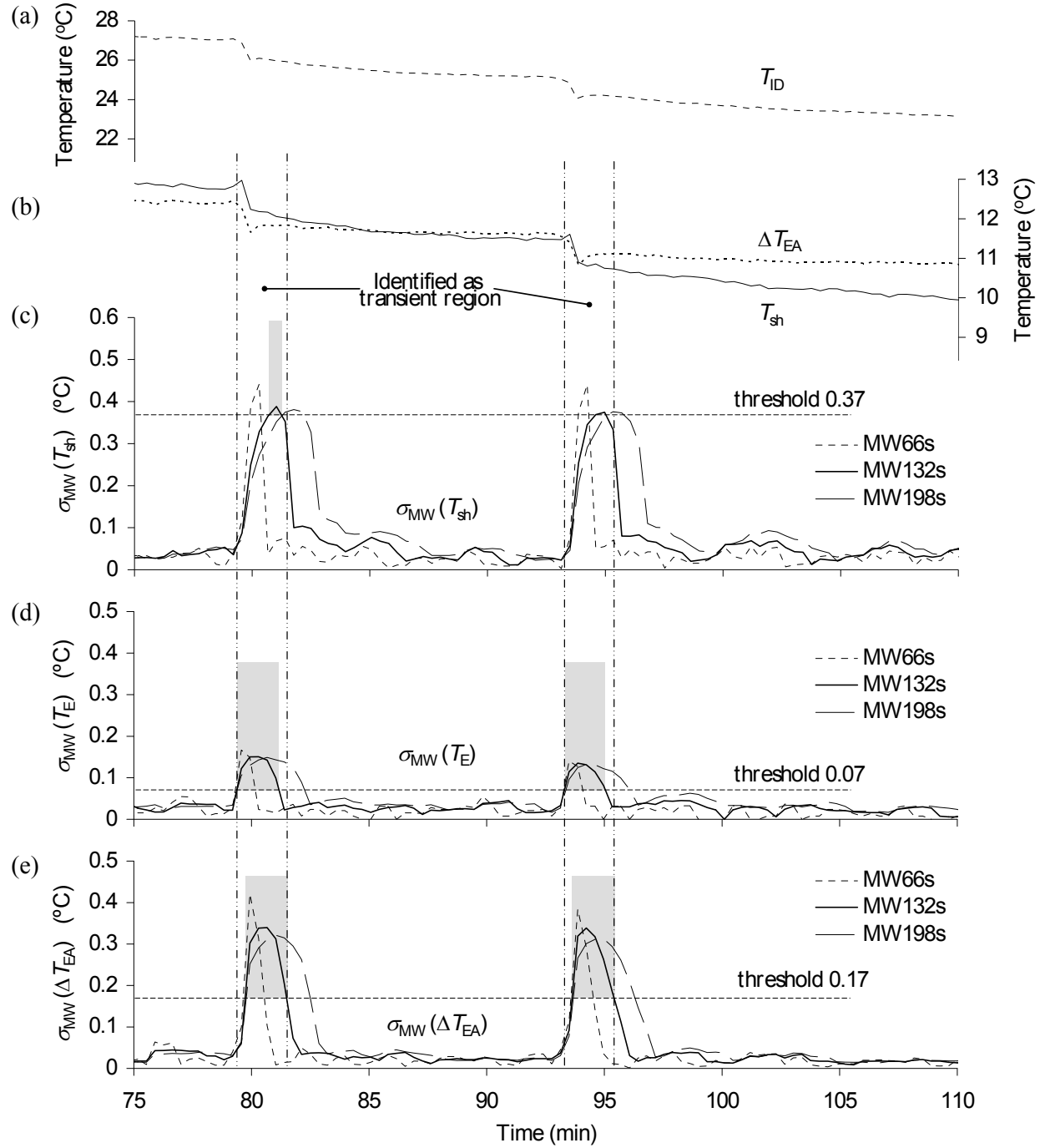
Figure 3.8.   Identification of steady state during an indoor load change test with a 20 % refrigerant undercharge fault, $T_{OD} = (35 \pm 0.5)°C$, (a) T_{ID}; (b) T_{sh} and ΔT_{EA}; (c) $\sigma_{MW}(T_{sh})$; (d) $\sigma_{MW}(T_E)$; (e) $\sigma_{MW}(\Delta T_{EA})$
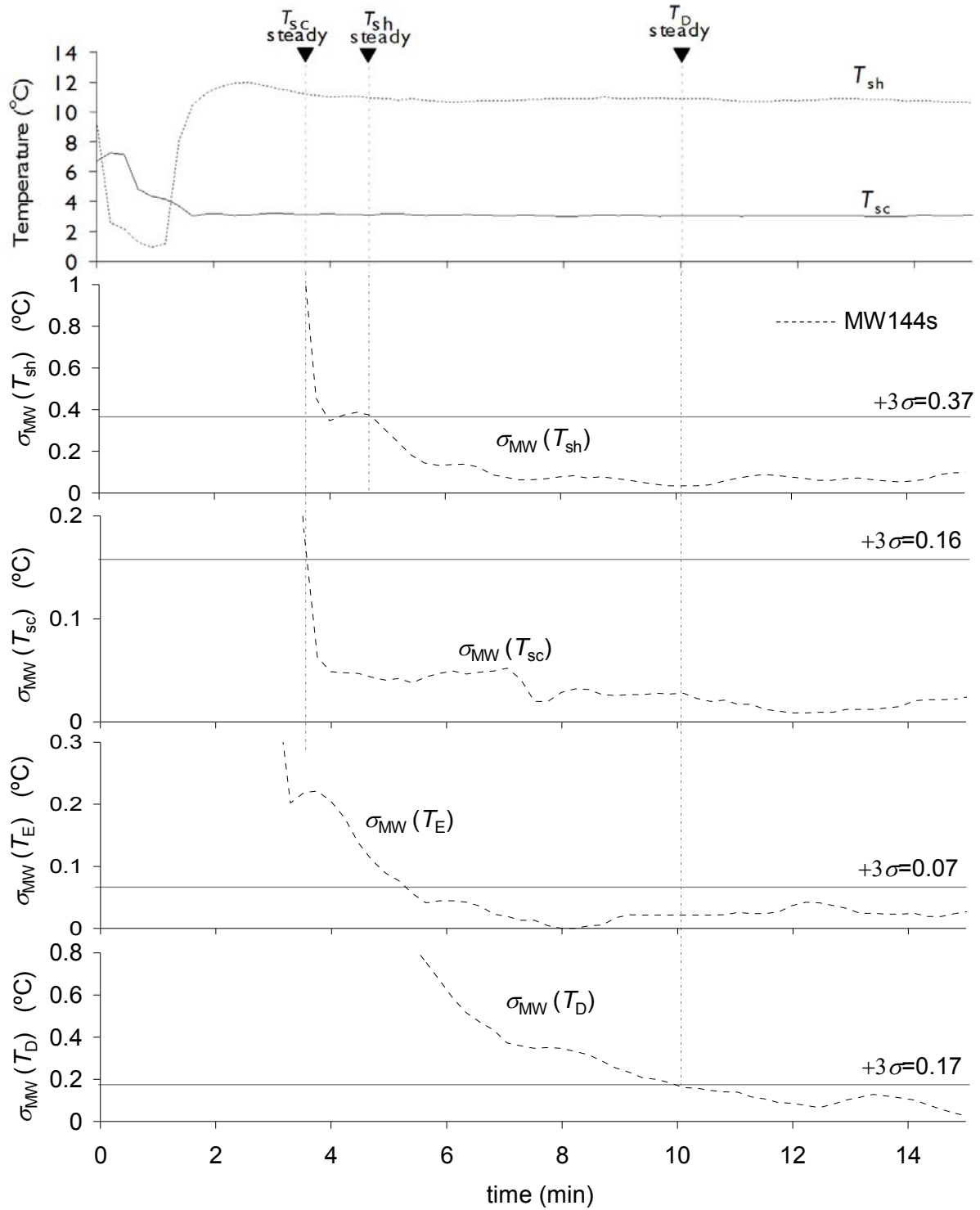
Figure 3.9. Variation of T_{sc}, T_{sh}, T_E and T_D during startup transient with a 30 % condenser air flow fault level with standard deviations calculated for a 144 s (9 sample) moving window

3.4.2 Test with an evaporator air flow fault imposed

An evaporator fault was imposed by reducing the air flow rate through the evaporator heat exchanger. The fault level was a 30 % reduction in normal air flow.
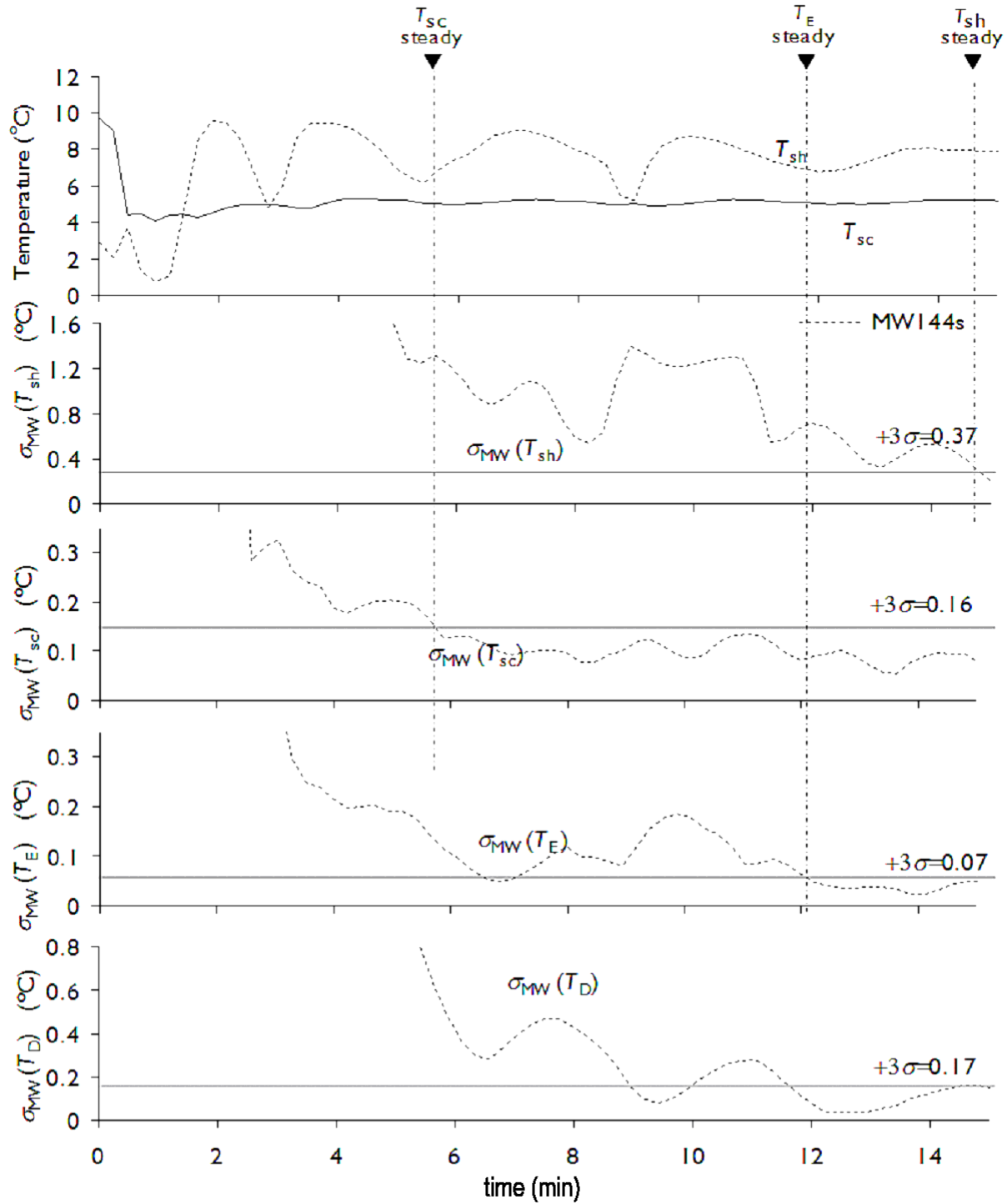
Figure 3.10. Variation of T_{sc}, T_{sh}, T_E and T_D during startup transient with a 30 % evaporator air flow fault level with standard deviations calculated for a 144 s (9 sample) moving window

Figure 3.10 shows evaporator exit refrigerant superheat and inlet refrigerant liquid subcooling in addition to the standard deviation of T_{sh}, T_{sc}, T_E, and T_D within a 144 second (9 sample) moving window. The standard deviation of superheat remains below its threshold indicating steady state at about 15 minutes after the system starts. Because this system has an evaporator air flow fault, the evaporator saturation temperature and superheat became unstable. On the contrary, the subcooling and the discharge temperature reach steady state well before T_{sh}. The steady-state detector can still indicate the initiation of steady state for all of the features, but this indication occurred much later than the no-fault steady-state startup time interval of 6 min 30 s.

3.5 Verification of the Steady-State Detector During Continuous and Cyclic Operations

Figure 3.11 shows an example of the operation of the steady-state detector based on the thresholds listed in Table 3.3. The data in Figure 3.11 were sampled while the system was continuously operating. Figure 3.11(a) shows rises and falls in indoor temperature as electric air heaters were turned on and off.

Based on the Boolean chart in Figure 3.11(c), the features T_D and T_{sh} have the largest number of transitions from 0 (unsteady) to 1 (steady); however, the majority of the time was identified as steady state. Even though indoor temperature varied as the indoor electric heaters were energized, the system was still regarded as steady when the feature variations were small enough to satisfy the steady–state detector. From Figures 3.11(a) and 3.11(c), several minutes of uniform temperature do not necessarily produce a steady state. Since T_{OD} was fixed during these tests, the condenser saw little change as indicated by the steady Boolean values of T_C and T_{sc}.

Figure 3.12 presents performance of the steady-state detector for on-off transient operation at fixed operating conditions. At approximately 3 minutes the system turned off and remained off for 27 minutes. It turned off again at 33 minutes, on at 40 minutes, off at 47 minutes, on at 57 minutes, off at 63 minutes and finally on again at 88 minutes. The figure includes five of seven features. Based on the value (0 or 1) of the 'SS detector' in Figure 3.12(b), it takes 5 minutes or more of system runtime to reach a steady state.
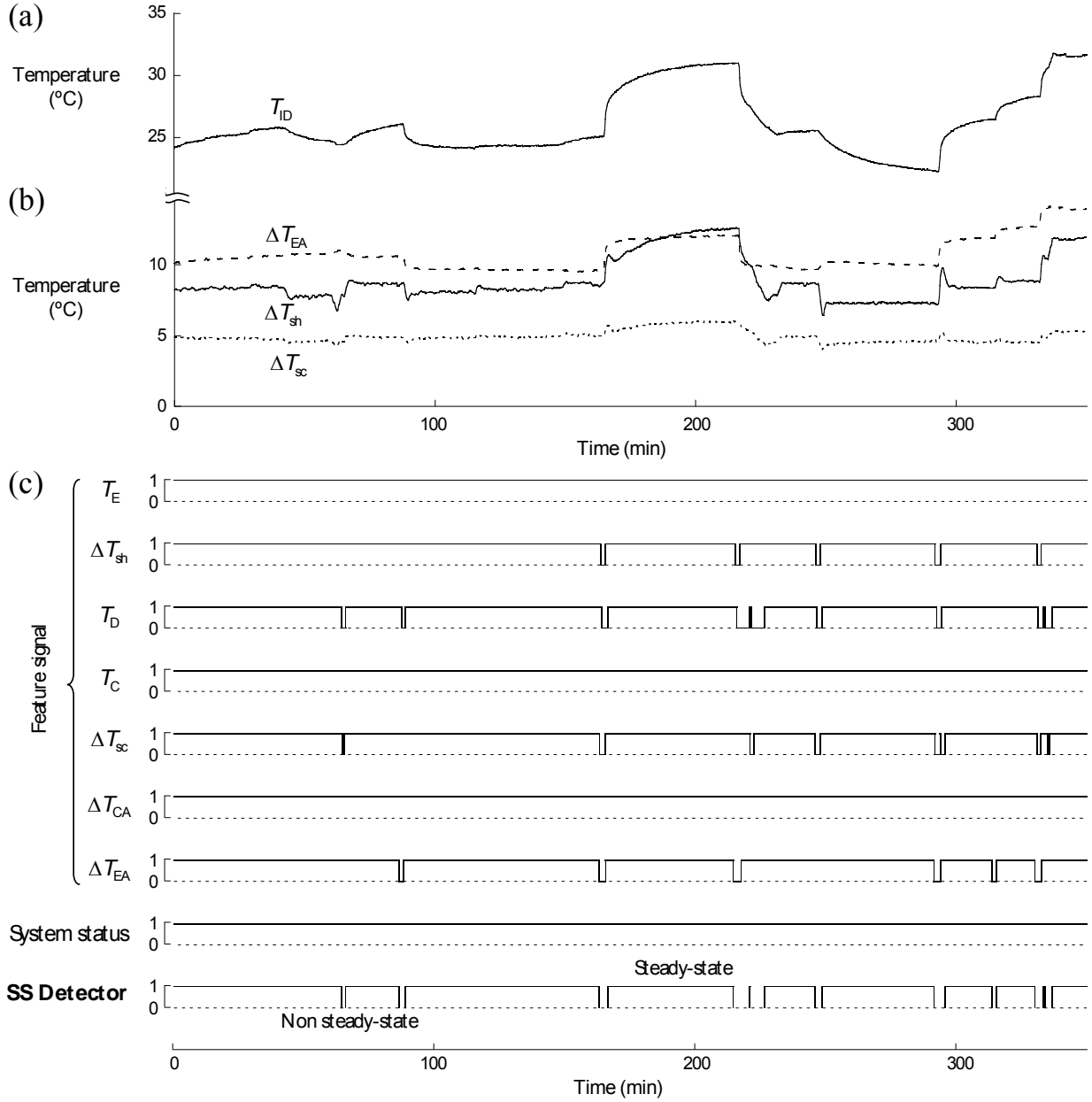
Figure 3.11. Sample operation of a steady-state detector during continuous system operation (T_{ID} = varied, T_{OD} = (27.8±0.5) °C, moving window size = 150 s); (a) Variation of indoor temperature; (b) Temperature differences; ΔT_{EA}, T_{sh}, and T_{sc}; (c) Decision from the steady-state detector: 0-unsteady, 1-steady
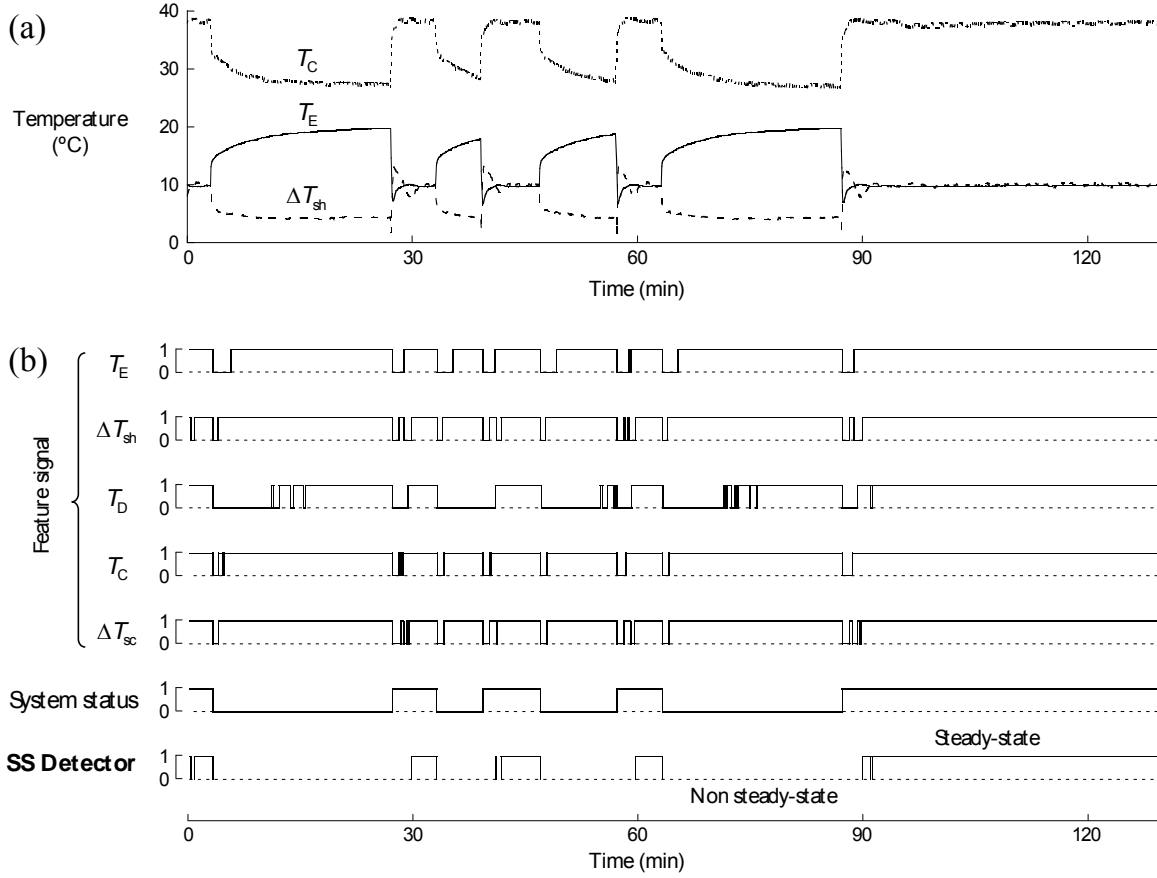
Figure 3.12.   Operation of a steady-state detector during system on-off transient operation (T_{ID} = (26.7±0.5) °C; T_{OD} = (27.8±0.5) °C); (a) Variation of T_C, T_E, and T_{sh}; (b) Decision from the steady-state detector: 0-unsteady, 1-steady

3.6 Steady-State Detector Summary

The presented methodology for developing a steady-state detector for a vapor compression system is based on a moving window and using standard deviations of seven parameters selected as features. When the threshold band of the features was set at ±3σ, reflecting their fluctuations during steady-state operation, the optimal moving window size was approximately 140 seconds for a 14 second sampling rate. Of the seven monitored features, T_{sh} and T_{sc} measurements were sufficient for determining the onset of steady state during the startup transient. However, they were not the dominant steady-state indicators during indoor temperature change tests, where T_E and ΔT_{EA} were needed for proper steady-state identification. Consequently, we recommend including all FDD features in the steady-state detector to ensure the robustness of the detector because different features may play key roles with different transients. While the proposed steady-state detector was developed from no-fault data, we verified that it can perform correctly with a faulty system.

A practical steady-state detector must be defined based upon the heat pump and system controller that will perform the fault detection and diagnosis. For any given system, the designer may choose FDD features other than those identified here. The system controller and instrumentation used in a commercial product most likely will have a different resolution or noise immunity than a dedicated lab quality data acquisition system. This would translate into larger standard deviations and threshold values with different sampling rates and moving window sizes.

CHAPTER 4. NO-FAULT REFERENCE MODEL

FDD systems recognize a set of key system performance parameters and function by comparing predicted fault-free parameter values to the current values, and analyzing their residuals. Thus, a reference model is required to estimate the fault-free system parameters at any operating condition. Since an FDD system model requires precise estimation of system parameters, generalized conventional analytical modeling techniques were replaced with empirical correlations in several studies (Gordon and Ng, 1995; Rossi, 1995). Lee et al. (1996b) used an artificial neural network to relate the dominant symptoms and faults of an air-handling unit. To improve the modeling capability of an FDD system, Li and Braun (2003) implemented a polynomial/generalized neural network regression in their reference model, and they produced improved interpolation and extrapolation results for a roof top unit. Navarro-Esbri et al. (2007) developed a low-data-requirement model based on neural networks for a water-to-water vapor compression system focused on refrigerant leak detection. In this study we collected extensive data for cooling mode, and evaluated multivariable polynomial and artificial neural network reference models for their ability to predict system features selected for the FDD scheme.

4.1 Data Collection for the Reference Model

We systematically varied three independent variables, T_{OD}, T_{ID}, and T_{IDP} and monitored the seven features as listed in Table 3.2. To implement the most efficient test procedure, outdoor temperature was fixed at one of four constant values, the addition of steam to the indoor chamber was set at one of several discrete levels by modulating a steam valve, and the indoor dry-bulb temperature was changed over the desired operating range by energizing 10 fixed heaters sequentially. For example, as the number of indoor electric heaters increased, the test conditions moved from A to B in Figure 4.1(a) with indoor temperature increasing and relative humidity decreasing. The data were recorded continuously and filtered through the steady-state detector, which qualified steady-state data for use in development of the reference model. In this process, instability of the system due to on-off transients and rapid load changes was filtered out by the steady-state detector.

Table 4.1 shows operating conditions for the fault-free tests. The four outdoor temperatures were maintained within ±0.3 °C. For the indoor conditions, the amount of steam introduced to the indoor chamber was fixed such that the humidity ratio varied from 0.0037 to 0.0168. Data were recorded, every 18 s, as indoor dry-bulb temperature varied from 15.3 °C to 33.9 °C. The range of operating conditions for which data were collected defines the applicable limits for the FDD scheme.

Table 4.1. Operating conditions for fault-free tests

Outdoor dry-bulb temp. (°C)	27.8, 32.2, 35.0, 37.8
Indoor dry-bulb temp. (°C)	15.3 to 33.9
Indoor humidity ratio	0.0037 to 0.0168

From the total number of 10409 recorded data sets, 5830 data sets passed through the steady-state detector. Among these steady-state sets, 2176 sets were collected at 27.8 °C outdoor temperature, 1732 sets at 32.2 °C, 633 sets at 35.0 °C, and 1289 sets at 37.8 °C. Figure 4.1(b) shows a sample of data (every fifth data point) taken at four fixed outdoor temperatures. In addition, we performed ARI standard rating tests at 27.8 °C indoor and 35.0 °C outdoor dry-bulb temperatures (ARI, 2006) and included these data to develop the fault-free steady-state reference models.
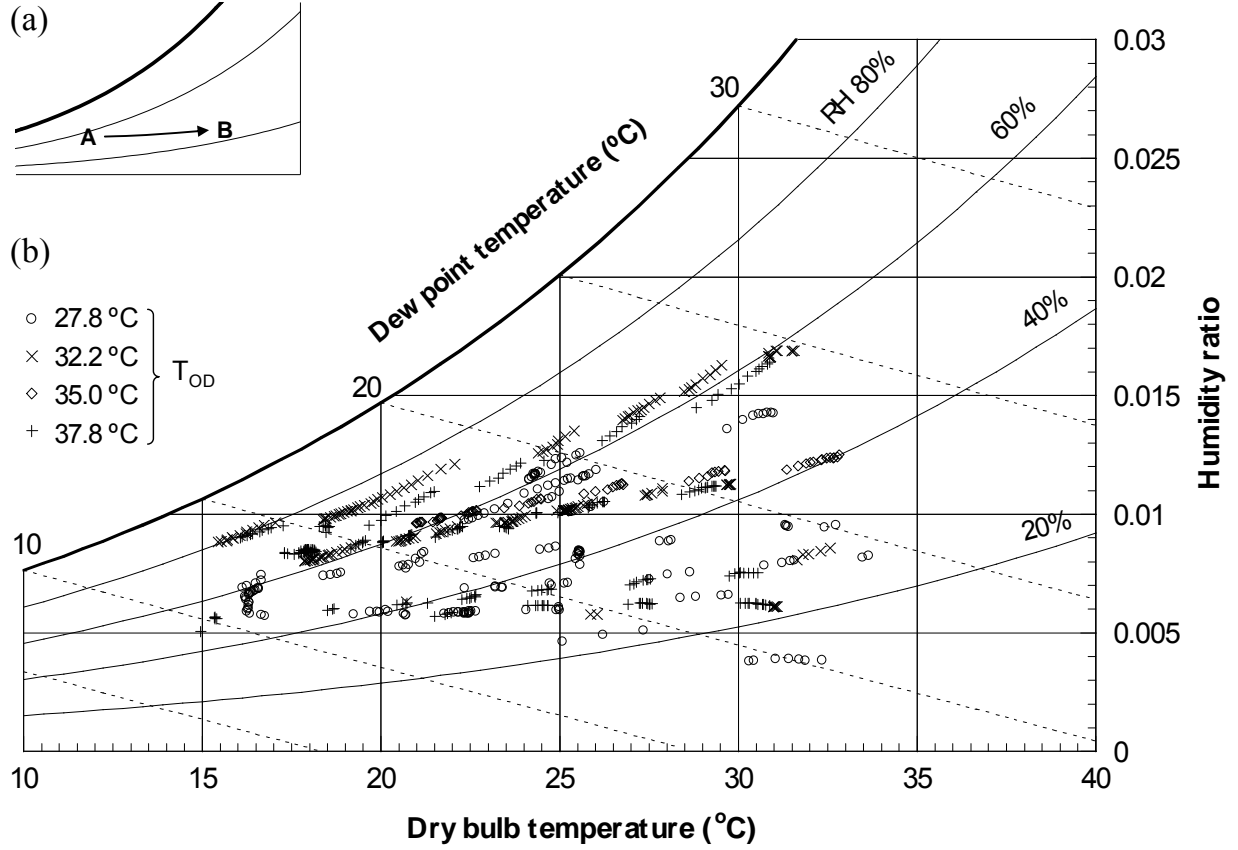
Figure 4.1. Indoor test conditions on a psychrometric chart for fault-free model experiments at a fixed outdoor temperature; (a) Indoor condition change as electric heaters activate; (b) Sampled indoor air conditions at four T_{OD} (27.8, 32.2, 35.0, and 37.8) °C

4.2 Multivariate Polynomial Regression (MPR) Reference Model

The MPR model belongs to the "black-box" category of models, which do not consider the physics of the system and require a large data set to accurately predict a system's performance. In our study, we evaluated 1st, 2nd, 3rd, and 4th order MPR models representing the seven key features of the heat pump. The higher order MPR models offer better accuracy of prediction; however, excessive polynomial order for a relatively small database may worsen data interpolation. The MPR models presented in this work have an advantage in that they have a simple structure and can be programmed easily. In addition, they can be implemented for any other experimental database with little modification, because they have no physical basis.

We used outdoor dry-bulb temperature (T_{OD}), indoor dry-bulb temperature (T_{ID}), and indoor dew-point temperature (T_{IDP}) as independent variables. These variables were regressed upon the database generated from the fault-free tests. Equations (4.1a), (4.1b), (4.1c), and (4.1d) show the general form of the regressed equations for the ith feature (or i^{th} dependent variable) as 1st, 2nd, 3rd, and 4th order MPR models, respectively.

$$\phi_i^{(1)} = a_0 + a_1 T_{OD} + a_2 T_{ID} + a_3 T_{IDP} \quad (1^{st} \text{ order}) \tag{4.1a}$$

$$\phi_i^{(2)} = \phi_i^{(1)} + a_4 T_{OD}^2 + a_5 T_{ID}^2 + a_6 T_{IDP}^2 + a_7 T_{OD} T_{ID} + a_8 T_{ID} T_{IDP} + a_9 T_{IDP} T_{OD} \quad (2^{nd} \text{ order}) \tag{4.1b}$$

$$\phi_i^{(3)} = \phi_i^{(2)} + a_{10}T_{OD}{}^3 + a_{11}T_{ID}{}^3 + a_{12}T_{IDP}{}^3 + a_{13}T_{OD}T_{ID}T_{IDP}$$

$$+ a_{14}T_{OD}{}^2T_{ID} + a_{15}T_{OD}{}^2T_{IDP} + a_{16}T_{ID}{}^2T_{OD} + a_{17}T_{ID}{}^2T_{IDP} + a_{18}T_{IDP}{}^2T_{OD} + a_{19}T_{IDP}{}^2T_{ID}$$

(3rd order) (4.1c)

$$\phi_i^{(4)} = \phi_i^{(3)} + a_{20}T_{OD}{}^4 + a_{21}T_{ID}{}^4 + a_{22}T_{IDP}{}^4 + a_{23}T_{ID}{}^2T_{OD}{}^2 + a_{24}T_{ID}{}^2T_{IDP}{}^2 + a_{25}T_{IDP}{}^2T_{OD}{}^2$$

$$+ a_{26}T_{ID}T_{OD}{}^3 + a_{27}T_{ID}T_{IDP}{}^3 + a_{28}T_{IDP}T_{OD}{}^3 + a_{29}T_{ID}{}^3T_{OD} + a_{30}T_{ID}{}^3T_{IDP} + a_{31}T_{IDP}{}^3T_{OD}$$

(4th order) (4.1d)

$$+ a_{32}T_{ID}{}^2T_{OD}T_{IDP} + a_{33}T_{ID}T_{OD}{}^2T_{IDP} + a_{34}T_{ID}T_{OD}T_{IDP}{}^2$$

4.3 Artificial Neural Network (ANN) Reference Model

An Artificial Neural Network (ANN) model was developed for the seven features. The relationship of independent variables and features is learned by an artificial neural network using a back propagation algorithm (Wasserman, 1989; Hassoun, 1995). Figure 4.2 shows the structure of the ANN used in this study. It has three input variables (T_{OD}, T_{ID}, and T_{IDP}) and one output. This neural network has three layers consisting of an input, hidden, and output layer with the input and hidden layers having three nodes. The sigmoid function is used as the activation function of the hidden layer. The weight coefficients and offsets are "learned" using a momentum back propagation algorithm through more than 10,000 iterations.

The input layer acts only as input nodes; no processing of T_{OD}, T_{ID}, or T_{IDP} occurs within the input layer. The various arrows between the input layer and the hidden layer indicate weights, or multipliers, applied to each input variable before passing to the sigmoid function within each hidden layer node. Equation 2 illustrates the output of a neuron, $f(s)$, and how the sigmoid function is applied within the layers.

$$f(s) = \frac{1}{2}\left(1 + \tanh(2s)\right) \qquad s = \left(\sum_{k=1}^{3} x_k w_k\right) + c \tag{2}$$

The three-node hidden layer uses 9 adjustable weighting coefficients and 3 offset coefficients. The single output node has its own 3 adjustable weighting coefficients and a single offset to produce the final predicted value of the feature, F_{model}. Each heat pump feature to be represented by the ANN is calculated in this manner using T_{OD}, T_{ID}, or T_{IDP} as inputs. The predicted value is compared to the measured value to produce an error value (residual) for each feature. The back propagation algorithm is then used to adjust the weights and offsets to minimize the error, or "train" the ANN.
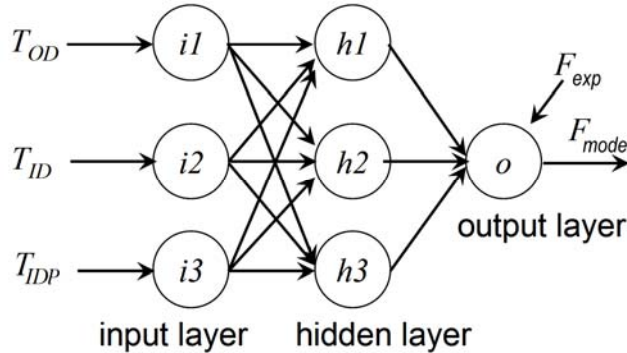
Figure 4.2. Artificial neural network structure

In validating the model, we used a dataset of 111 points, a subset of the full 5830 point dataset, to improve the performance of the ANN learning process. The 111 point dataset was created by selecting the data points that were spaced by a minimum predetermined distance in the independent variables space. First, T_{ID}, T_{OD}, and T_{IDP} were mapped onto *xyz*-coordinates. Each (x, y, z) point was then compared to all of the other points to determine if any of the other points fell within the predetermined distance of the point. This is equivalent to drawing a sphere of radius *r* at a particular (x, y, z) location and examining this sphere volume to determine if any other points fall within. If another (x, y, z) point fell within this sphere, it was removed from the data set; thus all of the independent variable (x, y, z) points were examined and winnowed in this manner. In this study, *r* was selected to be 0.96 °C.

Table 4.2 shows the mean squared residual (MSR), as calculated by Eq. 4.3, for the multivariate polynomial regression models and ANN model when fit to the reduced dataset consisting of 111 points. The mean squared residual is the sum of the squared residuals divided by the degrees of freedom for the regression and is an estimate of the model variance (Graybill and Iyer, 1994a).

$$MSR = \frac{\sum_i \left\{ x_i - \phi_i^{(n)} \right\}^2}{N - (m+1)} \tag{4.3}$$

Table 4.2. MSR of the models fit to a reduced dataset for the seven selected features

Feature	1st order	2nd order	3rd order	4th order	ANN
T_E (°C)	1.298	0.095	0.052	0.016	0.122
T_{sh} (°C)	0.980	0.442	0.222	0.140	0.263
T_C (°C)	0.136	0.014	0.007	0.005	0.072
T_D (°C)	2.215	0.373	0.246	0.110	1.341
T_{sc} (°C)	0.198	0.139	0.081	0.036	0.395
ΔT_{EA} (°C)	1.431	0.087	0.030	0.012	0.159
ΔT_{CA} (°C)	0.106	0.019	0.012	0.009	0.024
N			111		
m+1	4	10	20	35	16

Table 4.3 shows the MSRs for the models fit to the full dataset of 5830 points while Table 4.4 shows the MSRs for the reduced dataset models applied to the full dataset. The reduced models' MSRs of Table 4.4 and the full dataset MSRs of Table 4.3 differ by an average of 26 %. Thus the reduced dataset is a good representation of the system features, but the full dataset model produces smaller MSRs.

Table 4.3. MSR of the models fit to the full dataset for the seven selected features

Feature	1st order	2nd order	3rd order	4th order	ANN
T_E (°C)	0.979	0.072	0.051	0.015	0.129
T_{sh} (°C)	1.055	0.397	0.176	0.121	0.273
T_C (°C)	0.108	0.011	0.007	0.005	0.068
T_D (°C)	2.078	0.342	0.213	0.088	1.403
T_{sc} (°C)	0.202	0.135	0.066	0.028	0.480
T_{EA} (°C)	1.103	0.066	0.027	0.011	0.159
T_{CA} (°C)	0.085	0.018	0.014	0.012	0.030
N			5830		
m+1	4	10	20	35	16

Table 4.4. MSR of the reduced dataset model applied to the full dataset of seven selected features

Feature	1st order	2nd order	3rd order	4th order	ANN
T_E (°C)	0.992	0.077	0.061	0.023	0.129
T_{sh} (°C)	1.160	0.465	0.258	0.213	0.273
T_C (°C)	0.110	0.012	0.0080	0.0078	0.068
T_D (°C)	2.403	0.409	0.285	0.161	1.407
T_{sc} (°C)	0.213	0.144	0.083	0.055	0.482
T_{EA} (°C)	1.116	0.072	0.033	0.017	0.160
T_{CA} (°C)	0.087	0.019	0.017	0.019	0.030
N			5830		
m+1	4	10	20	35	16

As expected, a higher order MPR model produces a smaller mean squared residual. However, the number of model coefficients increases exponentially due to the addition of the crossterm coefficients. The number of coefficients used to model each feature may be reduced by applying an F-Test to each coefficient of the respective models (Graybill and Iyer, 1994b). The F-statistic is calculated using the following equations:

$$MS_{drop} = \frac{\left(SSR_{reduced} - SSR_{full}\right)}{m - g} \tag{4.4}$$

$$MSR_{full} = \frac{SSR_{full}}{N - (m+1)} \tag{4.5}$$

$$F = \frac{MS_{drop}}{MSR_{full}} \tag{4.6}$$

where g+1 is the number of coefficients in the reduced model. The F-statistic follows an F distribution with m-g and N-(m+1) degrees of freedom. Large values of F indicate that the terms removed from the reduced model were significant. One may use the F-statistic as a means of ranking the contribution of a particular coefficient to the fit of the regressed model. By dropping one term at a time and sorting the reduced models in terms of their F-statistics, the effect of removal of a particular term may be assessed by comparing the MSR of the reduced model to that of the full model. Table 4.5 shows the results of this technique when applied to a backward elimination on the full 3rd order polynomial model.

Table 4.5. F-statistic and percent change in MSR with respect to the full models for seven features

	3rd Order MPR Model Backward Elimination, x = T_{OD}, y = T_{ID}, z = T_{IDP}		
Feature	Less than 1 % higher MSR	Less than 5 % higher MSR	Less than 10 % higher MSR
	Term(s) removed		
T_E	z, xy, z²	z, xy, z², x², y, y³	N/A
T_{sh}	y², z, z², y²z, x	y², z, z², y²z, x, y, z³	y², z, z², y²z, x, y, z³, y²x, y³
T_C	y	y, y²z, y³	y, y²z, y³, yz, z³
T_D	x, y³	x, y³, yz, x²y, z²y, xyz	x, y³, yz, x²y, z²y, xyz, z²
T_{sc}	y, z², z²y, y³	y, z², z²y, y³, y²x, yz, z²x	N/A
ΔT_{EA}	y	N/A	y, z
ΔT_{CA}	x²z, y, z³	x²z, y, z³, y³, z, x²y, zx	N/A

N/A: The % change in MSR does not fall within the
bounds with the removal of a single coefficient.

Table 4.5 shows that one to five terms may be removed from the full 3rd order polynomial while the models' MSRs remain less than 1 % from the full models' MSRs. If the criteria is raised to within 5 % of the full models' MSRs, up to seven terms may be removed from several of the 3rd order polynomials. Raising the percentage change in MSR to within 10 % allows the removal of up to nine coefficients for T_{sh}. The decision as to how many terms to remove is at the discretion of the model developer, but as with any regression equation, the confidence interval on the mean value of any of the features determined at a particular value of the independent parameters will be larger for larger MSRs. The confidence interval is a function of the MPR model standard residual ($\sqrt{MSR}$), the Student's t-value for the particular confidence level, and degrees of freedom (Ott 1984).

Figure 4.3 shows the performance of the full MPR models and ANN model during operation at a T_{OD} of 27.8±0.3 °C. If an air conditioning system is installed in the field, T_{ID} may change continuously according to indoor cooling load or thermostat settings. The three features, T_{sh}, T_{sc}, and T_D, are shown in Figure 4.3 because they varied the most as indoor temperature changed. In Figure 4.3(a), where there is an abrupt change in T_{ID}, the steady state of the system is broken, as indicated by the steady-state detector in Figure 4.3(e).

Figures 4.3(b), 4.3(c), and 4.3(d) show T_{sh}, T_{sc} and T_D as predicted by the 1st, 2nd, and 3rd order MPR models and the ANN model. The 3rd order MPR model shows the best fit to the measured data during steady-state operation. As the order of the polynomial model decreases, the fit to the experimental data set degrades. Predictions by the ANN model are worse than those by the 3rd order MPR model. The T_{sh} predicted by the ANN model is comparable to that of the 3rd order MPR model (Figure 4.3(b)), but T_{sc} was not predicted well by the ANN model, as shown in Figure 4.3(c). The predicted values of T_D for the ANN model are between the 1st and 2nd order MPR models, as shown in Figure 4.3(d).
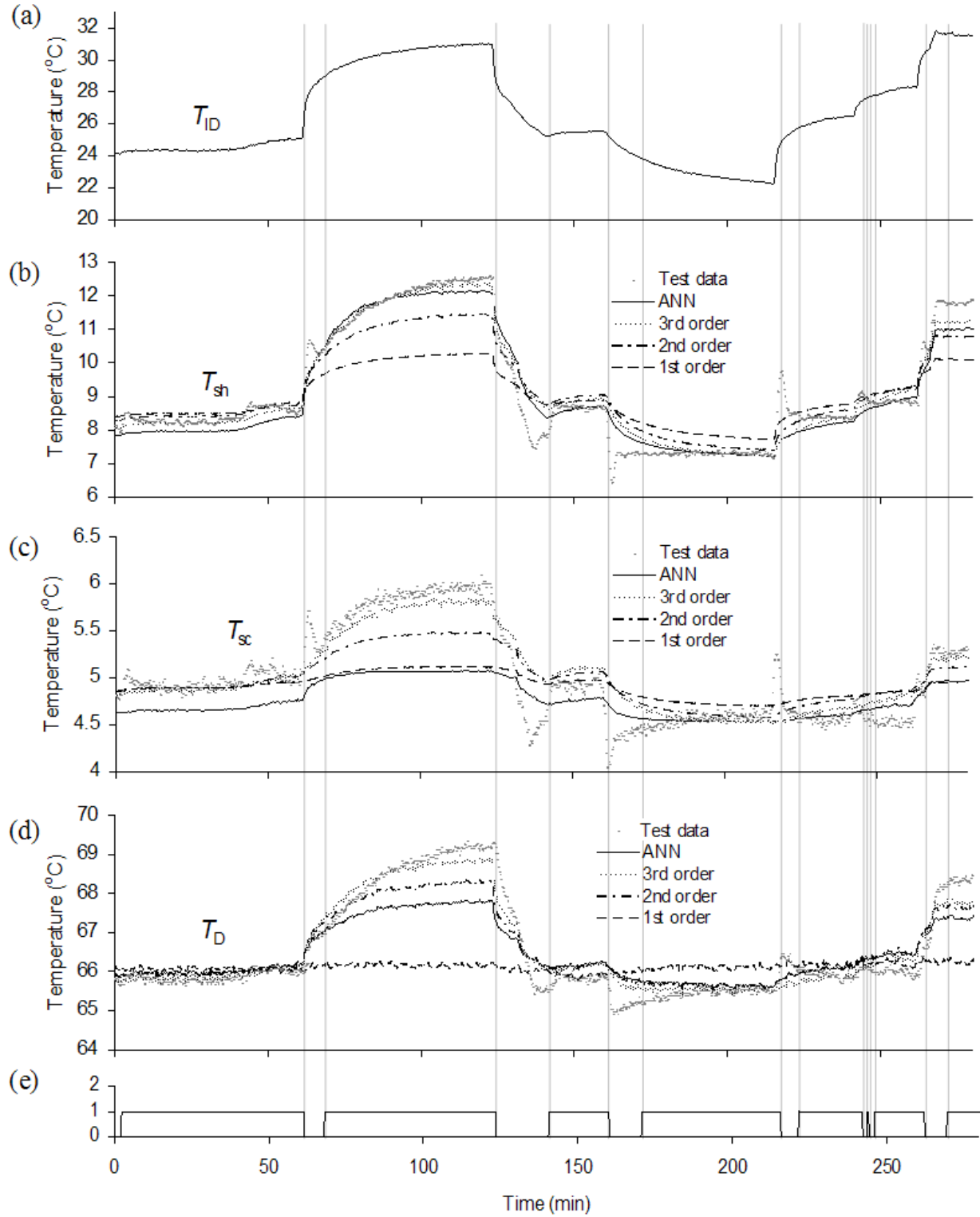
Figure 4.3. Performance of MPR models and ANN model to predict features during a sample operation period; (a) T_{ID}; (b) T_{sh}; (c) T_{sc}; (d) T_D; (e) steady state

4.4 Sensitivity of the Reference Model to the Steady-State Detector

4.4.1 Effect of the steady-state detector threshold values on the reference model

Data used to generate the reference model was taken by changing indoor or outdoor temperatures in a stepwise manner and holding the new conditions for a fixed time interval. If we had selected a very strict definition of steady state (small threshold values such as a fraction of one standard deviation of the important features), the time required to reach steady state would have increased. During the stepwise changes in conditions, a given temperature state was only maintained for 30 to 45 minutes before moving on to the next condition. A stricter more sensitive steady-state detector would have indicated steady state for a shorter period of time, thus limiting the number of data points collected for the given time period. The number of data points collected along with their variance from their respective means would be greatly affected by this change in threshold values and thus influence the reference model's dataset. A strict, small threshold steady-state detector produces fewer data points with lower variance, while a less strict steady-state detector would produce more data points with higher variance.

The threshold values of standard deviation for the monitored system features define the performance of the steady-state detector. The smaller a threshold is the more stable the system must be before steady state is declared. On the other hand, if a threshold is too small more time is required to collect reference data, and this small threshold value may inhibit data collection. Large thresholds increase the variability of the reference model and the effectiveness of the FDD system. Therefore, it is necessary to find thresholds that minimize the uncertainty and variability of the reference model while maximizing the use of experimental data.

To investigate the relation between reference model and threshold values, we compared the various reference models as a function of various threshold values. To do this, the system reference model was re-calculated after all data were filtered through the steady-state detector using different thresholds. Specifically, we developed the 2nd order polynomial reference model from the steady-state data determined by the steady-state detector with (0.06, 0.17, 0.28, 0.56, and 1.11) °C ((0.1, 0.3, 0.5, 1.0, and 2.0) °F) thresholds for all features. Then, we calculated the standard deviation between the steady-state data and predicted data for all features.

$$\text{Standard Deviation} = \sqrt{\frac{\sum (\text{Predicted value - Measured value})^2}{N}} \qquad (4.3)$$

Figure 4.4 shows the polynomial reference model standard deviation and data extraction percentage for each system feature. The x-axis represents the threshold for the seven features. As the threshold of the steady-state detector increases, the standard deviations of T_D, T_{sh}, T_E, and T_{sc} pass through an optimal point. Discharge temperature and superheat show this tendency clearly. In this figure, we can see that the optimal threshold exists around 0.17 °C (0.3 °F) for T_D, T_{sh}, T_E, and T_{sc}. Below 0.17 °C (0.3 °F), the uncertainty worsens due to the increase of model residuals caused by excessive filtration by the steady-state detector. Considering both data extraction rate and uncertainties of the thermocouple sensors, the thresholds should be set between 0.11°C to 0.28 °C (0.2 °F to 0.5 °F). This figure compares well to the ±3σ thresholds listed in Table 3.3 which indicates that the selection of thresholds that at three times larger than the steady-state standard deviation produces a near minimum model standard deviation (as calculated by Equation 4.3) while at the same time yielding acceptable use of the available data.
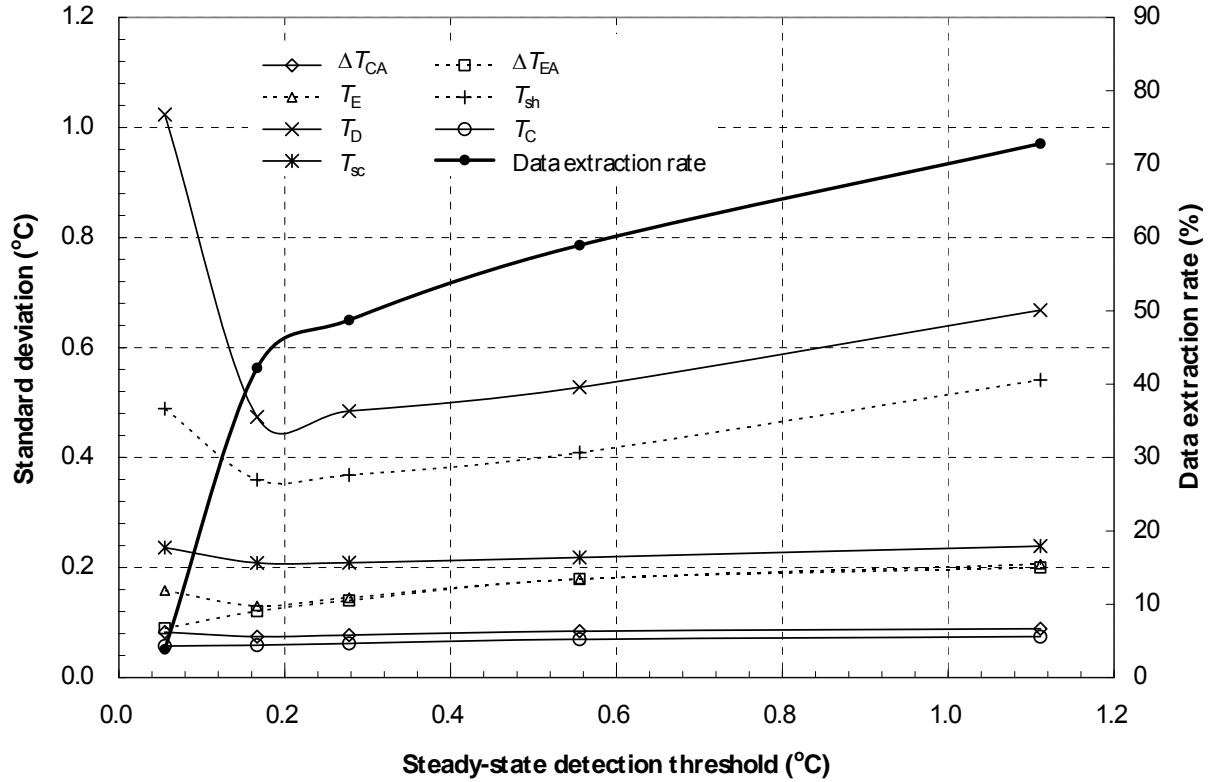
Figure 4.4. Standard deviation for the seven features of the no-fault system reference model and data extraction rate as a function of the steady-state detector thresholds (sampling interval: 18 seconds, moving window size: 144 seconds)

4.4.2 Example of the steady-state detector applied to the experimental heat pump

Figures 4.5(a) and 4.5(b) show sample feature residuals as a function of indoor temperature and relative humidity. In Figure 4.5, all of the non steady-state data having large deviation from the reference were filtered out. For both figures, zone A represents the non steady-state data filtered out during the startup transient. In the low humidity area of Figure 4.5(b), marked as zone B or 'TXV hunting,' highly fluctuating data were filtered out by the steady-state detector. Since the evaporator capacity is reduced for dry inlet air conditions, refrigerant exiting the evaporator oscillates between saturated and superheated. These abrupt condition changes at the evaporator exit cause TXV hunting. When the TXV hunting occurs, other temperatures, especially on the evaporator side, also oscillate within a large range. The no-fault model would thus estimate the parameters inaccurately due to a lack of steady-state data in that range. Once the model estimations are acceptable for other conditions, there is no reason to set the steady-state thresholds so low as to filter all the oscillating data out. By including some data in this oscillating zone within a no-fault model, we can obtain a model that covers a wider range of operating conditions.
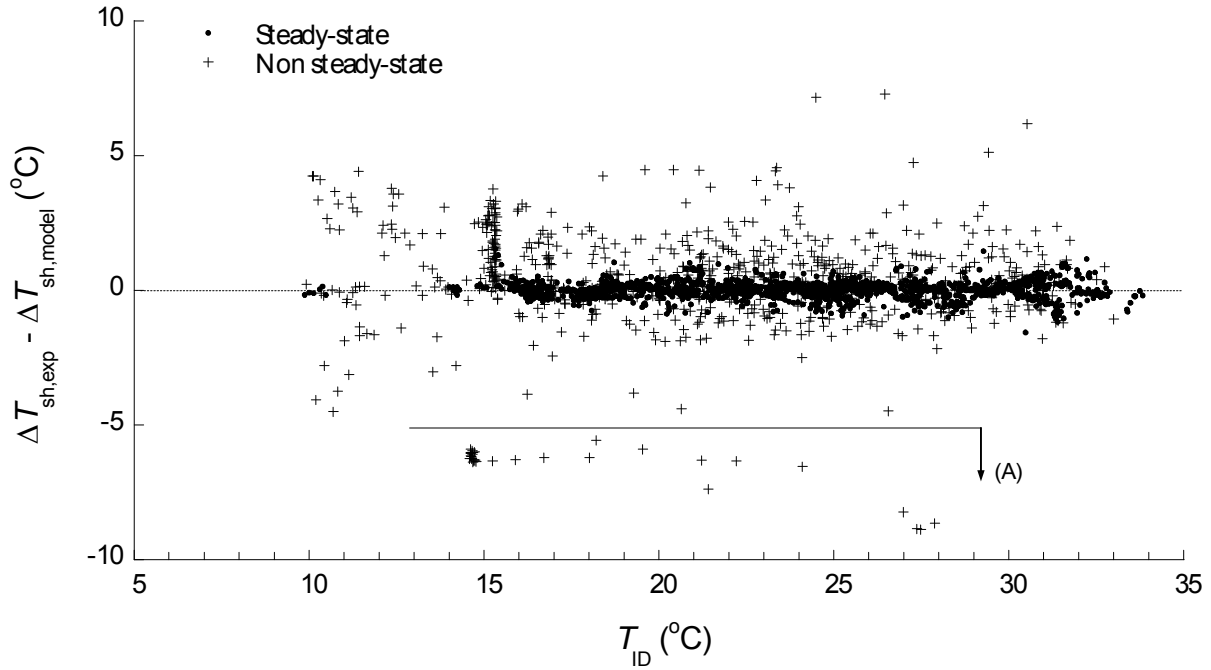
(a) Residual of evaporator exit superheat versus indoor temperature
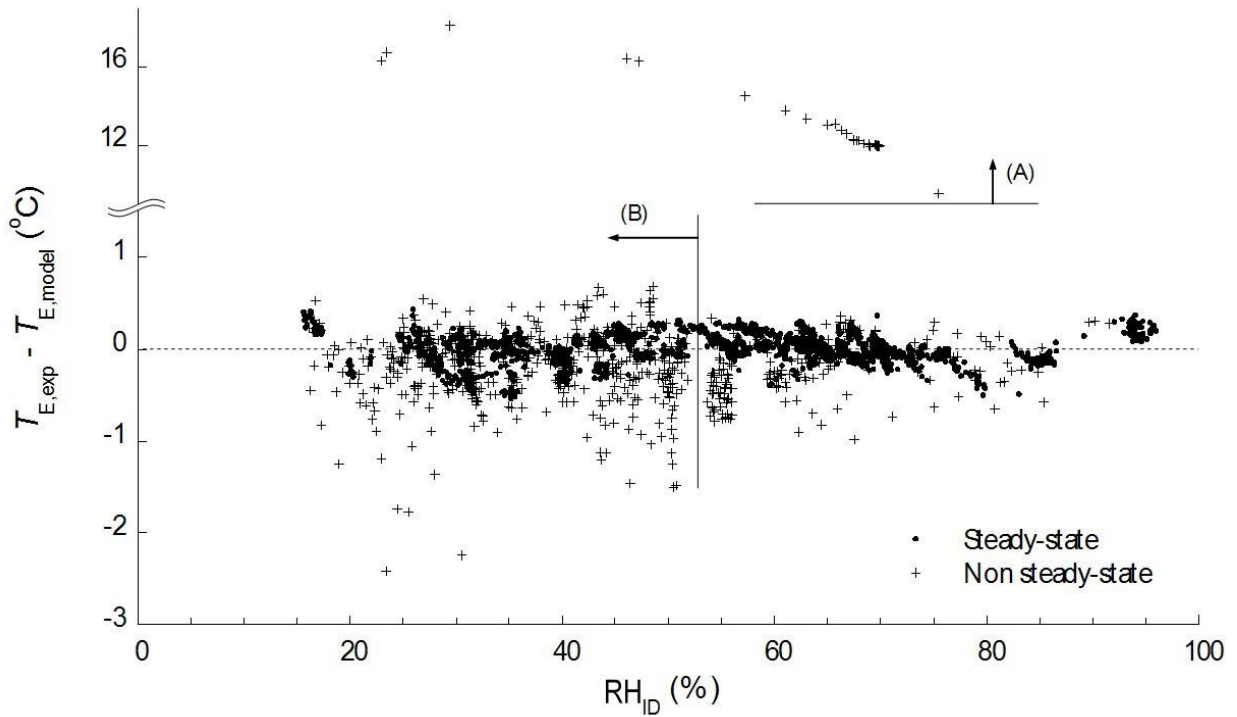
(b) Residual of evaporator exit saturation temperature versus indoor relative humidity

Figure 4.5.   Results filtered by the steady-state detector on the plots with feature residuals and independent variables (zone A: startup transient, zone B: TXV hunting)

4.5 Conclusions on System Reference Model

Seven features of a residential heat pump system were modeled using the 1st, 2nd, 3rd, and 4th order MPR models and an ANN model. The laboratory data were filtered by a steady-state detector, which automatically examined and processed data to improve data collection consistency and the resulting reference model for steady state. When we consider the accuracy of a reference model and usefulness of field data, the 3rd order polynomial model provides a reasonable fit uncertainty. The F-Test is one method of reducing the number of coefficients in a general linear model, and this technique may aid a developer in creating a more compact representation of the system features. The ANN model predicted all features with less accuracy than the 3rd order MPR model. Because of insignificant non-linearity between the independent variables and the features in the cooling mode, the ANN model did not produce lower MSRs than the best MPR models.

The reference model should not be over-specified by increasing the order of the MPR model. The model variance (MSR) should be lower than that associated with the measurement uncertainty of the independent variables. The smaller the models' variances, the smaller their contributions to the overall uncertainty of the predicted features. The model developer must decide on an acceptable level of model variance (associated with model order) based upon his FDD requirements and his ability to measure the variables.

In general, any order MPR model is a "black box model" and may be applied to any unknown system. When the system is changed slightly due to aging, a rigid non-physical model cannot accurately predict performance, which will cripple the FDD system. Although the model may be updated by ongoing commissioning, a model with semi-physical concepts can be easily adjusted to compensate for gradual system changes. Models that can adapt to changing system conditions must be developed. It would be advantageous to revise an existing model using up-to-date information, which would eventually evolve into a model capable of learning and self-tuning during normal operation, yet still ensure that the system remained within the manufacturer's performance limits.

CHAPTER 5. STATISTICAL METHODOLOGY FOR FAULT DIAGNOSIS USING A RULE-BASED APPROACH

The concept of a rule-based FDD system originated from expert system theory. Typically, knowledge-based expert systems are designed to solve problems that would normally be tackled by a human *expert*. Though the application domain of expert systems might be narrow and restricted, it provides experienced aid to developers (Tzafestas, 1989).

Since expert systems originated from human experts' knowledge, most of the related schemes can be interpreted by rules such as IF, THEN, ELSE algorithms. Based on this interpretation, there are a number of different methods for rule-based algorithms. Fault tree methods (Lee et al., 1985), fuzzy theory-based techniques (Krandel, 1992), and signed directed graph (SDG) methods (Kramer and Palowitch, 1987) were examined by several investigators.

A rule-based approach has various advantages, including the transparency, flexibility, and adaptability obtained by expressing the knowledge base as a set of rules. Commissioning engineers prefer using the rule-based algorithm because it helps with intuitive judgment of the system status. The rule-based algorithm is simple, so it is convenient to develop new rules for an unknown object system. Furthermore, the rule-based module is suitable to run on an embedded device like a microprocessor since it requires a relatively small computational capacity and memory requirement (Schein and Bushby, 2005). If FDD for HVAC systems are to be affordable, rule-based approaches are of great benefit because they require low computing overhead and are relatively inexpensive to implement.

5.1 Fault Influences on System Parameters

A handful of researchers have attempted rule-based algorithms for identifying vapor compression system faults. Since the pattern of system response changes with the system configuration, the researchers provided their unique rule-based charts for every corresponding system.

Rossi and Braun (1997) provided a rule-based chart of seven feature residuals with regard to five different faults of a rooftop air conditioner. The rooftop system was equipped with a constant speed compressor and a short tube expansion device. The authors merged the rule-based knowledge into a statistical pattern recognition technique in order to develop a fault detection classifier. Assuming the individual temperature measurements being independent, the type of each fault was classified. Breuker and Braun (1998b) modified the rule-based chart of the same system based on their experimental verification.

Castro (2001) tested a 41 kW (12 ton) air-cooled liquid chiller with a constant speed, two-stage reciprocating compressor. Twelve performance parameters were originally monitored to track system performance. Eight representative parameters were selected to build a rule-based chart. The author calculated Euclidean distances of the current state based on the selected two largest residuals, and estimated the possibility of a fault from the distance information. After detecting a fault, the data were input to the rule-based fault diagnosis algorithm.

Kim and Kim (2005) tested a water-to-water heat pump system with an electronic expansion valve (EEV) driven by an open-type variable-speed compressor. Depending on the cooling load, the compressor was operated in two modes, variable speed or constant speed. The authors provided two separate rule-based charts depending on the operating mode.

Table 5.1 lists rule-based charts from previous investigations on: (a) a rooftop air conditioner with a short tube orifice and a constant-speed compressor; (b) a water-to-water heat pump with an Electronic

Expansion Valve (EEV) and a constant-speed compressor; and (c) a heat pump with an EEV and a variable-speed compressor. The indices of features represent three rules; up-arrows (increased residual), down-arrows (decreased residual), and no-change (neutral residual).

Table 5.1. Comparison of rule-based patterns with regard to three different configurations of vapor compression systems

(a) Rooftop air conditioner with a short tube orifice and constant-speed compressor[1] (no controller)

Fault Type	T_E	T_{sh}	T_D	T_C	T_{sc}	ΔT_{CA}	ΔT_{EA}
Compressor valve leakage	↑	↓	↑	↓	↓	↓	↓
Refrigerant leakage	↓	↑	↑	↓	↓	↓	↓
Liquid-line restriction	↓	↑	↑	↓	↑	↓	↓
Condenser fault	↑	↓	↑	↑	↓	↑	↓
Evaporator fault	↓	↓	↓	↓	↓	↓	↑

[1] Breuker and Braun (1998b)

(b) Water-to-water heat pump with an EEV and constant-speed compressor[2] (one controller)

Fault Type		T_E	T_{sh}	T_D	T_C	T_{sc}	ΔT_{CW}	ΔT_{EB}	N
Compressor valve leakage		↑	–	↑	↓	↓	↓	↓	–
Refrigerant leakage	< 15%	–	–	–	–	↓	↓	↑	–
	> 15%	↓	↑	↑	↓	↓	↓	–	–
Condenser fault		↓	–	↑	↑	–	↓	↓	–
Evaporator fault		↓	–	–	↓	↑	↓	↓	–

[2] Kim and Kim (2005)

(c) Water-to-water heat pump with an EEV and variable-speed compressor[3] (two controllers)

Fault Type		T_E	T_{sh}	T_D	T_C	T_{sc}	ΔT_{CW}	ΔT_{EB}	N
Compressor valve leakage		–	–	↑	–	–	–	–	↑
Refrigerant leakage	< 15%	–	–	–	–	↓	–	–	↑
	> 15%	↑	↓	↑	↑	↓	↓	↓	–
Condenser fault		–	–	↑	↑	↓	–	–	↑
Evaporator fault		↓	–	↑	–	↑	–	–	↑

[3] Kim and Kim (2005)

Table 5.1(a) does not contain a neutral (NC (-)) index, which implies that a system response is directly associated with a fault regardless of the fault type. However, for the fixed orifice system (Table 5.1(a)) compared to an EEV-equipped system (Table 5.1(b)), many of the positive or negative indices become neutral indices. When compressor speed control is added, additional rules become neutral indices (see Table 5.1(b) and (c)).

If we pair the EEV and the variable-speed compressor as a single-controller unit, Table 5.1(a) can be regarded as a rule-based chart of a system with no controller, Table 5.1(b) for a single-controller system, and Table 5.1(c) for a double-controller system. As the number of controllers increases, the variability of the system features decreases. When a system changes due to an external influence, faults, or controller noise, controllers attempt to adjust the system to maintain the original status. Thus, controllers reduce system variability creating a much more fault-tolerant system (more neutral indices) (Kim and Kim, 2005).

The work done during this investigation shows that the addition of the extra control provided by a TXV does in fact create a more fault-tolerant system, and thus produces more neutral indices in the feature set. Table 5.2 shows the feature set and their changes with faulty operation for the faults imposed for the current cooling mode investigation. This added variety within the feature set can be directly compared to that of the fixed orifice expansion device system of Table 5.1(a).

Table 5.2 Rule-based fault pattern chart of seven features

Fault Type	zone[1]	T_E	T_{sh}	T_D	T_C	T_{sc}	ΔT_{CA}	ΔT_{EA}
Compressor valve leakage[2]	A	↑	–	↑	↓	↓	↓	↓
Improper outdoor air flow	A	↑	–	↑	↑	↓	–	↓
	B	↓	↑	↑	↑	↓	↓	↓
Improper indoor air flow[2]	A	↓	–	–	↓	–	↓	↑
Liquid-line restriction[3]	A	–	–	–	–	–	–	–
	B	↓	↑	↑	↓	↑	↓	↓
Refrigerant undercharge	A	–	–	–	↓	↓	↓	↓
	B	↓	↑	↑	↓	↓	↓	↓
Refrigerant overcharge[2]	A	–	–	↑	↑	↑	–	–
No-fault	–	–	–	–	–	–	–	–

[1] Zone A: $T_{sh} < 9$ ºC, Zone B: $T_{sh} > 9$ ºC
[2] The case of $T_{sh} > 9$ ºC was not observed within the fault levels of this study.
[3] The rules when $T_{sh} < 9$ ºC were identical with no-fault cases.

Compared to the rule-based chart in Table 5.1(a), the rule-patterns for a liquid-line restriction and refrigerant undercharge fault were the same as Breuker and Braun (1998b) at a high fault level in zone B. Considering that they tested a rooftop air conditioner with a short tube orifice, this tends to indicate that the TXV is working like a fixed area expansion device; the TXV is saturated or at its control limits. However, the improper outdoor air flow fault rule-pattern in zone B is different from that of a condenser fault in Table 5.1(a), both of which were simulated by blocking the flow passage through the condenser. This is because the air inflow area of the outdoor unit was blocked from the bottom in this research, but Breuker and Braun (1998b) blocked the condenser randomly.

5.2 Classification of Feature Rules

5.2.1 Statistical rule-based classification for two cases; positive or negative residuals

Figure 5.1 shows two probability distributions corresponding to the current measurement and the no-fault model's estimate. The current mean, μ_i, and standard deviation, σ_i, are calculated in the moving window of on-going measurements. The estimated mean, $\mu_{i,NF}$, and standard deviation, $\sigma_{i,NF}$, of the ith feature are determined from the no-fault model and associated uncertainty, respectively. The difference in the two means, $\mu_i - \mu_{i,NF}$, is defined as the residual of the feature, r_i, in Equation 5.1.

$$r = \mu_i - \mu_{i,NF_i} \tag{5.1}$$

Assuming that the features are random variables, the estimated features from the no-fault model can be assumed to obey a Gaussian probability distribution, $N(\mu_{i,NF}, \sigma_{i,NF}^2)$. Based on the probability distributions and the sign of the residual (positive ↑ or negative ↓), the probability of the feature being

higher or lower than the reference model prediction can be estimated in a statistical fashion. Looking at Table 5.1(a), a set of seven features establishes a 7-dimensional multivariate Gaussian probability distribution. With the assumption that each dimension is independent, the probability corresponding to a given fault type can be calculated from a single variable Gaussian distribution (Rossi and Braun, 1997). Though the independent assumption was reported to be less accurate compared to other schemes that do not force independence (Li and Braun, 2003), the assumption of independence is still applicable in this type of FDD analysis, or in other words we may ignore any cross-correlation, which simplifies this analysis.
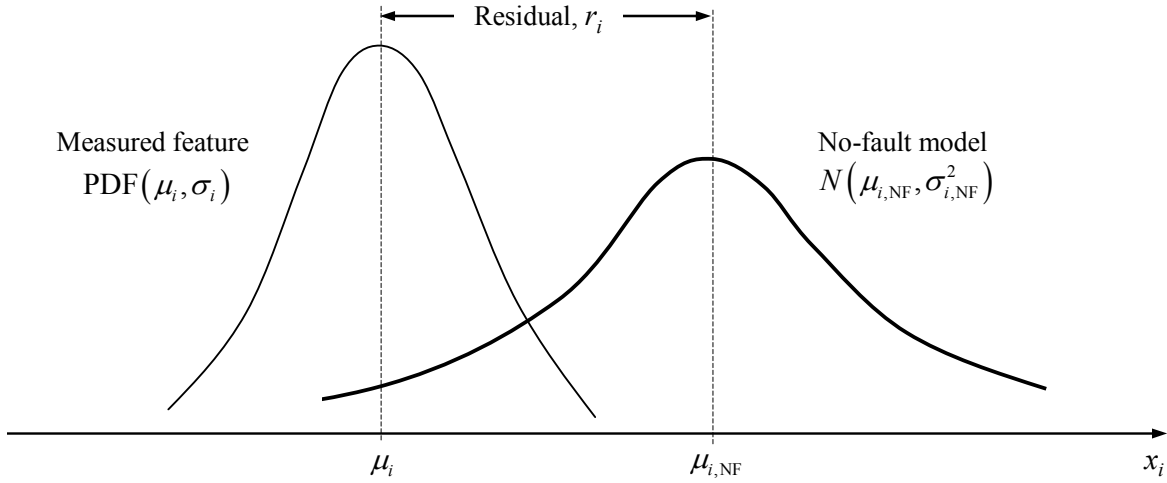
Figure 5.1. Probability density functions (PDF) of ith feature, x_i, for the current measurement and the no-fault model prediction

Equation 5.2 defines the probability of seeing the jth fault, $P(F_j \mid \mathbf{X})$, corresponding to the set of m independent variables, $\mathbf{X}$, for the current measurements.

$$P(F_j \mid \mathbf{X}) = P(C_{1j} \mid X_1) \cdot P(C_{2j} \mid X_2) \cdots P(C_{ij} \mid X_i) = \prod_{i=1}^{m} P(C_{ij} \mid X_i) \tag{5.2}$$

$P(C_{ij} \mid X_i)$ denotes the individual probability of seeing case variable C (positive $\uparrow$ or negative $\downarrow$) for the ith feature (T_{sh}, T_{sc}, ΔT_{EA}, etc.) with the jth fault type. Since the features are assumed to be independent, the total conditional probability, $P(F_j \mid \mathbf{X})$, can be obtained by the multiplication of individual $P(C_{ij} \mid X_i)$'s. Rossi and Braun (1997) assumed that the current distribution follows a Gaussian pattern and suggested $P(C_{ij} \mid X_i)$ be represented by the form of Equation 5.3.

$$P(C_{ij} \mid X_i) = \frac{1}{2}\left[1 + a_i \mathrm{erf}\left(\frac{\mu_i - \mu_{i,\mathrm{NF}}}{\sqrt{2}\sigma_{i,\mathrm{NF}}}\right)\right] = \frac{1}{2}\left[1 + a_i \mathrm{erf}\left(\frac{r_i}{\sqrt{2}\sigma_{i,\mathrm{NF}}}\right)\right]$$

$$\tag{5.3}$$

$$\text{where } a_i(r_i) = \begin{cases} +1 \text{ if } r_i > 0, \\ -1 \text{ if } r_i \le 0. \end{cases}$$

Standard deviation $\sigma_{i,\mathrm{NF}}$ is the square root of the ith diagonal component in the covariance matrix of the no-fault model. The set of rules in Table 5.1(a) consists of positive $\uparrow$ or negative $\downarrow$ discrete values. Noting that an up-arrow rule implies positive r_i and a down-arrow rule implies negative r_i, the constant a_i

is assigned a value of 1 for positive r_i or –1 otherwise. Since Equation 5.3 can be applied only to rules with two classes (positive ↑ or negative ↓), it is necessary to evaluate the neutral (– or NC) class in a different way.

5.2.2 Statistical rule-based classification with three case indices; positive, negative, or neutral

A set of measurement features can be regarded as a multi-dimensional Gaussian probability distribution. In contrast to the rules of Rossi and Braun in Section 5.2.1, the neutral index (– or NC) is required for the system features shown in Table 5.1(b) and (c) and Table 5.2. When we use the assumption that each dimension is independent, we can extend the statistical rule-based classification to a three-class problem (positive ↑, negative ↓, or neutral –) with each class being represented by a simple Gaussian distribution rather than a more complicated distribution with multiple degrees of freedom and dependencies.

When the operation is controlled by feedback controllers, a system will adjust itself based upon the control variable. Since the active control reduces system variation, many features will not change clearly enough to apply a two-rule diagnosis. Therefore, researchers using rule-based charts, in several investigations for more complicated systems, added a neutral rule resulting in a three-class variation (positive, negative, neutral). Applying different rules for different systems as seen in the previous researches, allowed us to more easily find the appropriate FDD rules for the system.

A conventional way of classifying residuals as positive, negative, or neutral is by enumerating the probable faults based on belief functions. For example, Figure 5.2 illustrates a Boolean and a smoothed belief function, $b(C_{ij} | X_i)$, of the ith feature with regard to residual r_i. $P(R_i)$ is the Gaussian distribution of residual r_i. Boolean classification results in a case of 0 or 1 depending on the value of residual r_i and the given threshold ε_i. When measurement noise produces random fluctuation in the signal around the thresholds, $+\varepsilon_i$ or $-\varepsilon_i$, a Boolean classification returns highly unstable belief values rapidly fluctuation between 0 and 1. To solve this problem, later investigators implemented smoothed belief functions to alleviate the diagnostic instability of Boolean classification. The smoothed belief function in Figure 5.2 represents a sigmoidal type suggested by Kramer (1987). The factor $1 - u_i$ (one minus the uncertainty in r_i) permits the introduction of uncertainty into the belief function. Although the Boolean belief function, $b(C_{ij} | X_i)$, is similar conceptually to the probability function $P(C_{ij} | X_i)$ in Equation 5.2, they should be kept separate since belief functions were derived empirically and have only a weak background in probability theory.
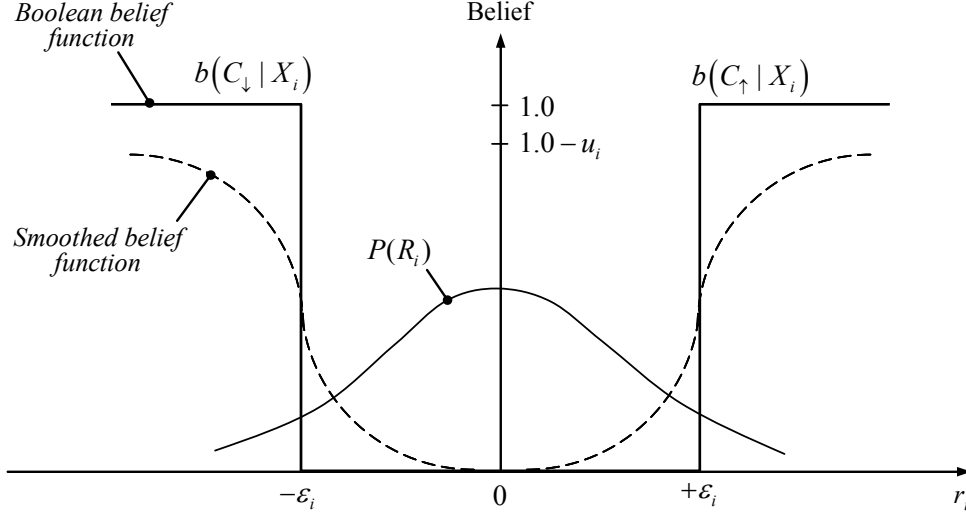
Figure 5.2. Example of a three case classification using a Boolean and a smoothed belief function with regard to the residual r_i and its Gaussian probability distribution $P(R_i)$ for a given threshold on r_i of $\pm\varepsilon_i$ (Kramer 1987)

When we assume that the measured signal is a normally distributed random variable with zero mean and a given variance, σ_i^2, the three cases ($\downarrow$, $\uparrow$, and $-$) can be estimated using standard statistics. The chi-squared (χ^2) probability distribution gives the probability of the squared sum of the standardized multi-dimensional variables that have normal independent distributions with zero-mean and unity variance. The number of variables is the degree of freedom. When the degree of freedom is one, the probability determined by a chi-square distribution is identical to a normal distribution. For the current research, the seven features, with the assumption of independence, provide seven individual chi-square distributions with 1 degree of freedom. Thus, statistical inferences can be based on a Gaussian distribution.

Figure 5.3 represents the probability for three cases of (a) negative ($\downarrow$), (b) positive ($\uparrow$), and (c) neutral ($-$). The conditional probability, $P(C_{ij} | X_i)$, is shown as the cross-hatched area depending on the corresponding rule. The probability for each rule was described in Equation 5.3.

$$P(C_\downarrow | X_i)$$
$$P(C_\uparrow | X_i) \tag{5.4}$$
$$P(C_- | X_i)$$

If $P(x)$ is a Gaussian distribution, $P(x_i < a_i)$ can be expressed in an explicit form by Equation 5.5.

$$P(x_i < a_i) = \frac{1}{2}\left[1 + \text{erf}\left(\frac{a_i - \mu_{i,\text{NF}}}{\sqrt{2}\sigma_{i,\text{NF}}}\right)\right] \tag{5.5}$$

where the error function, erf, is defined as follows:

$$\text{erf}(z) = \frac{2}{\sqrt{\pi}}\int_0^z e^{-t^2}\, dt \tag{5.6}$$
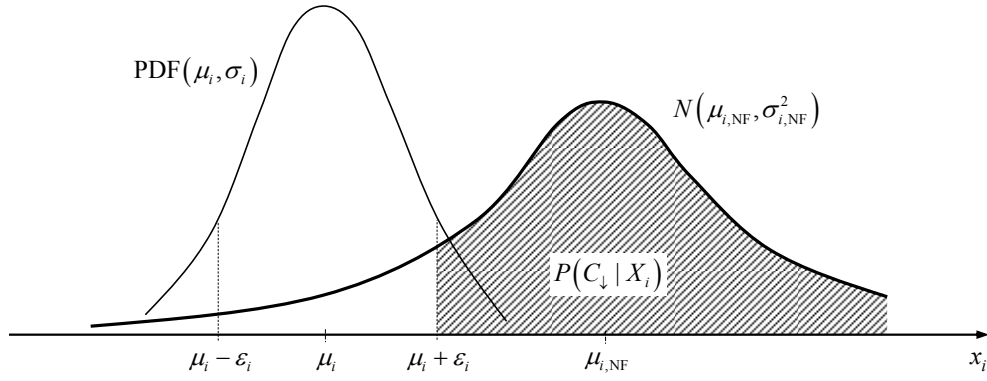
(a) Probability of negative (↓) case
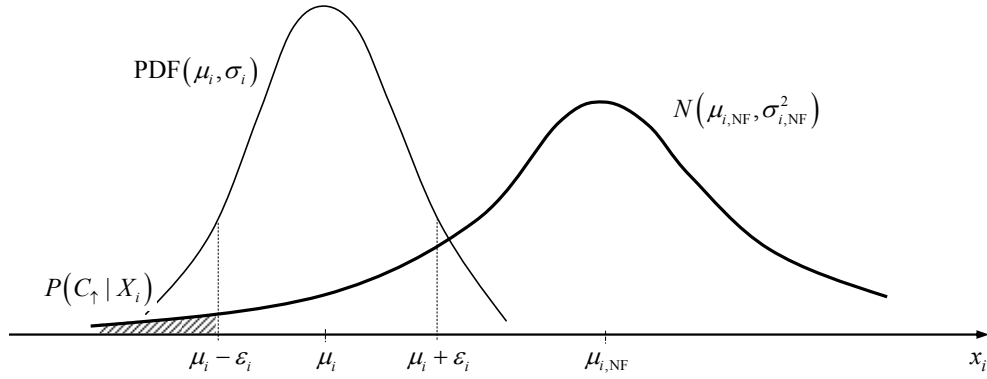
(b) Probability of positive (↑) case
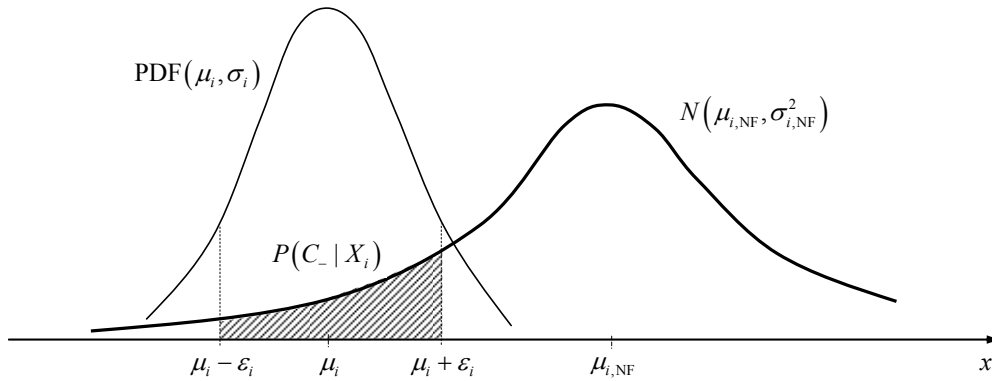
(c) Probability of neutral (–) case

Figure 5.3. Estimation of conditional probability of the ith feature with regard to the current measurement complying with individual rules. The subscript of the case variable C corresponds to the rules in Table 5.2 and represents a (a) negative change, (b) positive change, or (c) no change

From Equation 5.5 and Figure 5.3, the three probability terms in Equation 5.4 can be evaluated. Note that the cross-hatched area on the right side of the current distribution represents the negative change conditional probability since the current distribution produces a negative residual. The probabilities are expressed as functions of the threshold ε_i.

$$P\left(C_\downarrow \mid X_i\right) = P\left(x_i \geq \mu_i + \varepsilon_i\right) = \frac{1}{2}\left[1 - \operatorname{erf}\left(\frac{r_i + \varepsilon_i}{\sqrt{2}\sigma_{i,\mathrm{NF}}}\right)\right] \tag{5.7a}$$

$$P\left(C_\uparrow \mid X_i\right) = P\left(x_i \leq \mu_i - \varepsilon_i\right) = \frac{1}{2}\left[1 + \operatorname{erf}\left(\frac{r_i - \varepsilon_i}{\sqrt{2}\sigma_{i,\mathrm{NF}}}\right)\right] \tag{5.7b}$$

$$P\left(C_- \mid X_i\right) = P\left(\mu_i - \varepsilon_i < x_i < \mu_i + \varepsilon_i\right) = \frac{1}{2}\left[\operatorname{erf}\left(\frac{r_i + \varepsilon_i}{\sqrt{2}\sigma_{i,\mathrm{NF}}}\right) - \operatorname{erf}\left(\frac{r_i - \varepsilon_i}{\sqrt{2}\sigma_{i,\mathrm{NF}}}\right)\right] \tag{5.7c}$$

The summation of Equations 5.7a, 5.7b, and 5.7c equals unity.

$$P\left(C_\downarrow \mid X_i\right) + P\left(C_\uparrow \mid X_i\right) + P\left(C_- \mid X_i\right) = 1 \tag{5.8}$$

5.2.3 Decision rule index and building a rule-based chart

In our analysis a non-faulty, current measurement is assumed to show the same variation as the no-fault steady-state reference experiments.

$$\sigma_i^2 \approx \sigma_{i,NF}^2 \tag{5.9}$$

Let the measurement threshold, ε_i, be the multiplication of the measurement standard deviation, σ_i, by a positive constant s.

$$\varepsilon_i(s) = s\sigma_i, \; s > 0 \tag{5.10}$$

Let the standardized measurement residual be represented by z_i.

$$z_i = \frac{x_i - \mu_i}{\sigma_i} \tag{5.11}$$

Substituting Equations 5.9 to 5.11 into Equations 5.7 yields more compact definitions of the Probability Distribution Functions (PDF) for the standardized measurement residual of the ith feature.

$$P\left(C_\downarrow \mid Z_i\right) = P\left(z_i \geq s\right) = \frac{1}{2}\left[1 - \operatorname{erf}\left\{\frac{1}{\sqrt{2}}\left(\frac{z_i}{\sigma_i} + s\right)\right\}\right] \tag{5.12a}$$

$$P\left(C_\uparrow \mid Z_i\right) = P\left(z_i \leq s\right) = \frac{1}{2}\left[1 + \operatorname{erf}\left\{\frac{1}{\sqrt{2}}\left(\frac{z_i}{\sigma_i} - s\right)\right\}\right] \tag{5.12b}$$

$$P\left(C_- \mid Z_i\right) = P\left(-s < z_i < s\right) = \frac{1}{2}\left[\operatorname{erf}\left\{\frac{1}{\sqrt{2}}\left(\frac{z_i}{\sigma_i} + s\right)\right\} - \operatorname{erf}\left\{\frac{1}{\sqrt{2}}\left(\frac{z_i}{\sigma_i} - s\right)\right\}\right] \tag{5.12c}$$

Figure 5.4 shows probability distributions of the above three cases when the measurement threshold standard deviation multiplier, s, has values of 1 and 2. With a zero residual ($z_i = 0$), the no-change probability has a maximum value but the probabilities for up-change and down-change are non-zero. Compared with Figure 5.2 where there was no representation of a no-change case, the no-change case can be evaluated based on the value of z_i and its accompanying threshold ε_i ($= s\sigma_{i,NF}$). Depending on the value of the residual z_i and threshold ε_i, the probability of a feature's three possible states can be classified into one of the three categories as seen in Figure 5.4.
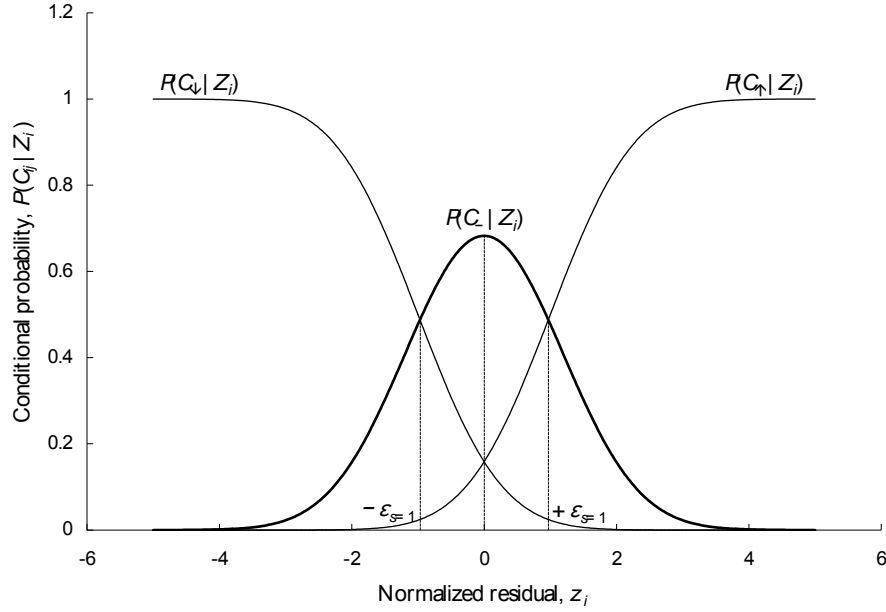
(a) $P(C_{ij} \mid Z_i)$ at $s = 1$
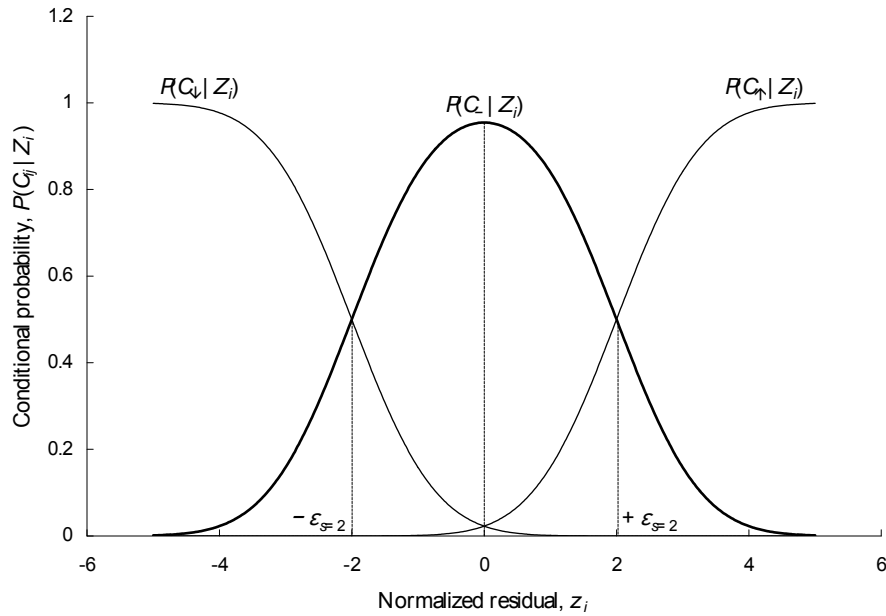
(b) $P(C_{ij} \mid Z_i)$ at $s = 2$

Figure 5.4. Classification probability functions for positive change, negative change, and neutral change with regard to the measurement threshold standard deviation multiplier, $s=1$ and $s=2$.

When we build a rule-based chart, each feature is associated with a case (or status) group ($C_\downarrow$, C_-, $C_\uparrow$) to which its residual, z, belongs. To clarify, Equation 5.13 shows the regimes for determining the rule index for the ith feature with the jth fault.

$$
\begin{aligned}
z_{ij} &\leq -\varepsilon_{i,s}(s) & Z_{ij} &\in C_\downarrow \\
-\varepsilon_i(s) &< z_{ij} < +\varepsilon_i(s) & Z_{ij} &\in C_- \\
z_{ij} &\geq +\varepsilon_i(s) & Z_{ij} &\in C_\uparrow
\end{aligned}
\tag{5.13}
$$

Equation 5.13 presents general cases of a case group for the threshold $\pm\varepsilon_i(s)$ ($\varepsilon_i > 0$) regardless of the assumption in Equation 5.10. For logical consistency, the probabilities of no-change and either of up-or-down change must be identical when the residual, z_{ij}, equals the threshold, ε_i, as in Equation 5.14.

$$\text{In case } P\big(C_\downarrow \,|\, Z_i\big) = P\big(C_- \,|\, Z_i\big), \text{ then } z_{ij} = -\varepsilon_i(s) \tag{5.14a}$$

$$\text{In case } P\big(C_\uparrow \,|\, Z_i\big) = P\big(C_- \,|\, Z_i\big), \text{ then } z_{ij} = +\varepsilon_i(s) \tag{5.14b}$$

From Equations 5.14, the relation between the constant s and threshold $\varepsilon_i(s)$ can be derived by setting Equations 5.12a and 5.12c or 5.12b and 5.12c to be equal. In either case, the equality can be formulated in the same form as in Equation 5.15.

$$
f\big(\varepsilon_i, s\big) = 1 - 2\mathrm{erf}\left\{ \frac{1}{\sqrt{2}}\left(\frac{\varepsilon_i}{\sigma_i} + s \right) \right\} + \mathrm{erf}\left\{ \frac{1}{\sqrt{2}}\left(\frac{\varepsilon_i}{\sigma_i} - s \right) \right\} = 0
\tag{5.15}
$$

Figure 5.5 represents the relation between the constant s and the threshold $\varepsilon_i(s)/\sigma_i$. As s increases, the function asymptotically approaches a linear function, $\varepsilon_i/\sigma_i = s$. When $s > 1$, the threshold is within 0.4 % of $\varepsilon_i/\sigma_i = s$. Therefore, we can simply assume $\varepsilon_i(s) \approx s\sigma_i$ as in Equation 5.10, in most cases, when $s > 1$.
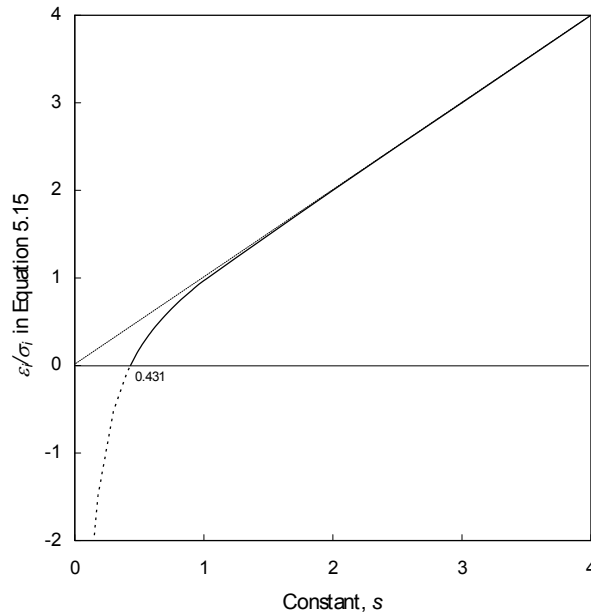
Figure 5.5. Relation between $\varepsilon_i(s)$ and s

48

5.2.3.1 Fault classification error in a three case classification

In order to estimate the probability of making a mistake and misinterpreting no-fault as being faulty, the no-fault probability was evaluated. If all the measurements are identical to the model expectations ($z = 0$), the system is performing exactly as predicted by the reference model, and the NC or neutral case for each feature will have a maximum probability as seen in Figure 5.4. Equation 5.16 is the classification error, α, based upon the overall probability, $P(C_- | \mathbf{Z})|_{\mathbf{z}=0}$, calculated when all the features have zero residuals. For example, an $\alpha = 1$ % probability would occur when the probability of NC ($P(C_- | \mathbf{Z})|_{\mathbf{z}=0}$) equals 99 %.

$$\alpha = 1 - P\left(C_- | \mathbf{Z}\right)\Big|_{\mathbf{z}=0} \tag{5.16}$$

From the previous definitions and assumption of the measurement of m features being independent, the classification error for a particular fault may be simplified.

$$\alpha = 1 - P\left(C_- | Z_1\right)\Big|_{z_1=0} P\left(C_- | Z_2\right)\Big|_{z_2=0} \cdots P\left(C_- | Z_m\right)\Big|_{z_m=0} = 1 - \left[P\left(C_- | \mathbf{Z}\right)\Big|_{\mathbf{z}=0}\right]^m \tag{5.17}$$

From Equations 5.12c and 5.17, the relation between the threshold standard deviation multiplier s and classification error α can be obtained. Figure 5.6 shows the plot of s versus α with regard to the number of features. In most cases, the classification error is below 5 % when $s > 2$.
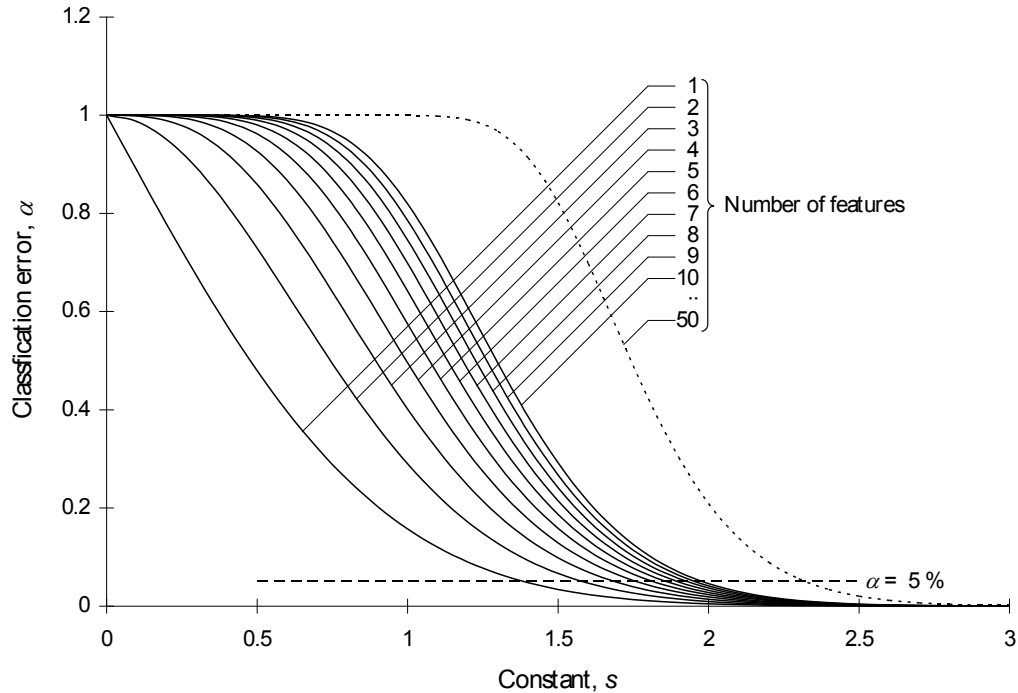
Figure 5.6. Classification error, α, versus measurement threshold standard deviation multiplier, s, with regard to the number of features

For a 5 % value of α, the independent assumption forces s to be larger as the number of features increases. When k cases are to be classified using m features, the combination will manipulate k^m classes. For example, a three case classification using two features combines $3^2 = 9$ classes, but 10 features combines

$3^{10} = 59049$ classes. Since no-fault is one class among all of the classes, the increase of independent features will reduce the no-fault probability exponentially. Thus, when the classification error, α, is fixed at a constant value, the threshold standard deviation multiplier s must increase as seen with 50 features in Figure 5.6. If the FDD system operates with a large number of features, the independent assumption may prevent the FDD system from detecting concurrent faults due to less sensitivity caused by a high s value. Therefore, the threshold standard deviation multiplier s needs to be set below a reasonable value that may require some engineering judgment to determine. The sensitivity of the no-fault reference model, the maintenance cost, and the uncertainty of the sensors should be accounted for when optimizing the threshold standard deviation multiplier s.

Since this evaluation is biased toward minimizing the risk of false alarm, the opposite case which interprets a fault state as being no-fault, is underestimated. Excessive credibility (large s value) degrades the sensitivity of an FDD system; however, false alarms decrease its usefulness and dependability. Since FDD systems for HVAC applications are mainly intended to reduce operating costs, false alarms are more detrimental than low sensitivity in terms of cost effectiveness. Therefore, it is reasonable to set a large threshold standard deviation multiplier (large s value) to minimize false alarms.

5.2.3.2 Probability of a fault classification error

Figure 5.7 presents the classification error using the polynomial reference models discussed in Chapter 4. The 1st, 2nd, and 3rd order MPR models were compared with regard to the constant s. Classification error, α, for the case with seven independent features is shown by a dashed line. In contrast to the curves seen in Figure 5.6, classification error decreases rapidly for smaller values of s than it did for the independent assumption cases of Figure 5.6. Unless the seven features are perfectly independent, the classification error would be less for this more realistic situation of some dependence between features. The three MPR models show similar trends; when $s < 0.5$, most of the no-fault cases are incorrectly categorized as being faulty; when $s = 2.0$, the classification error for the 3rd order MPR model drops to 0.58 % from 3.2 % as compared to the independent assumption.
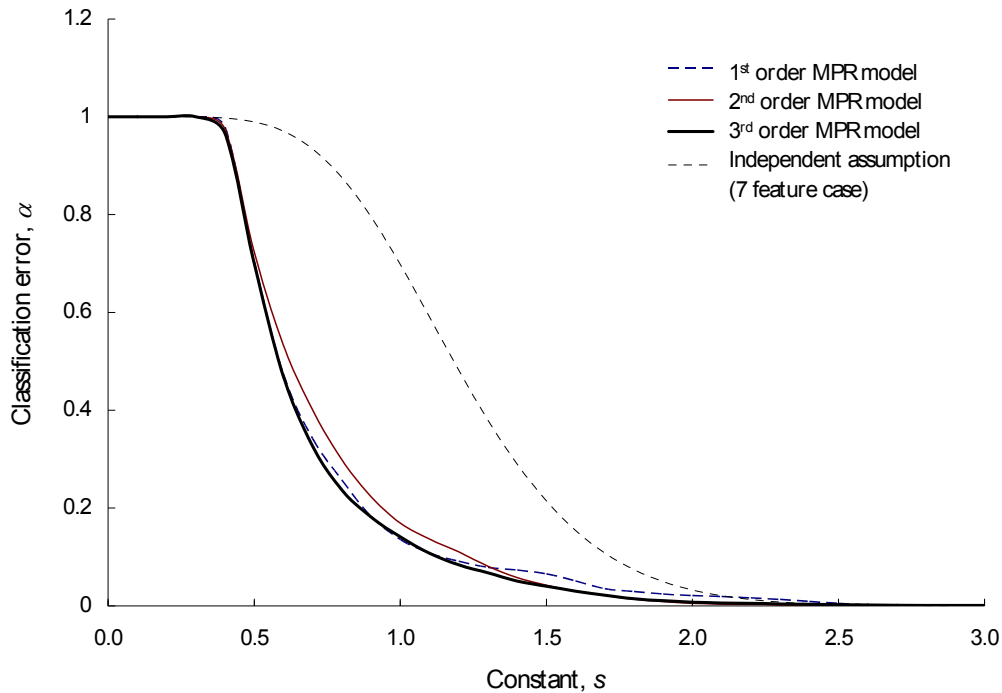
Figure 5.7. Classification error with regard to the constant *s* for three different MPR models with seven features

5.3 Setting the Neutral Threshold by Calculating Total Residual Uncertainty

5.3.1 Uncertainties due to steady-state variation and lack of measurement repeatability

To determine a realistic value of the neutral threshold, ε_i, as discussed in Section 5.2, validation of the measurements is mandatory. Naturally, the system measurements have uncertainties due to sensors – mostly thermocouples – and due to lack of measurement repeatability. The uncertainty of a thermocouple may come from measurement noise and drift. Considering the measurement noise behaves like zero-mean white noise, its natural variation can be characterized closely by the steady-state standard deviation, $\sigma_{i,SS}$, defined in Chapter 3. Thermocouple drift is the measurement bias that varies over longer time periods than noise. However, the thermocouple drift can be regarded as negligible in this research since the same built-in sensors are used for model development and application to the tested system for FDD, thus their bias has been considered in the reference model measurements.

To examine the repeatability of the system measurements, we analyzed repetitive tests. Referencing Table 3.3 in Kim et al., 2006, the tests were performed at 6 month intervals with 9 tests at condition 4 ($T_{OD} = 27.8\,°C$ (82.0 °F), $T_{ID} = 21.1\,°C$ (70.0 °F),   and $RH_{ID} = 50\,\%$),   11   tests   at   condition   5 ($T_{OD} = 27.8\,°C$ (82.0 °F), $T_{ID} = 26.7\,°C$ (80.0 °F), and $RH_{ID} = 50\,\%$), 8 tests at condition 8 ($T_{OD} = 37.7\,°C$ (100.0 °F), $T_{ID} = 21.1\,°C$ (70.0 °F),   and $RH_{ID} = 50\,\%$),   and   10   tests   at   condition   9   ($T_{OD} = 37.7\,°C$ (100.0 °F), $T_{ID} = 26.7\,°C$ (80.0 °F), and $RH_{ID} = 50\,\%$). The feature standard deviations from repeatability tests, $\sigma_{i,Repeat}$, are listed in Table 5.3.

Table 5.3. Standard deviation of the selected features

(°C)		T_{sh}	T_{sc}	T_{E}	T_{D}	T_{C}	ΔT_{CA}	ΔT_{EA}
Steady-state standard deviation	$\sigma_{i,\text{SS}}$	0.124	0.052	0.024	0.058	0.035	0.063	0.058
Standard deviation from repeatability tests	$\sigma_{i,\text{Repeat}}$	0.101	0.156	0.084	0.280	0.166	0.088	0.111

Table 5.3 gives us the measurement uncertainty due to steady-state variation, $\sigma_{i,\text{SS}}$, and due to variation from test-to-test (measurement repeatability), $\sigma_{i,\text{Repeat}}$, for similar test conditions. These two values will be used to calculate total residual threshold uncertainty for each feature.

5.3.2 Uncertainties due to the reference models

In section 5.2 we studied the variation of probabilities for the three feature cases ($C_{\downarrow}$, C_{-}, $C_{\uparrow}$) with the definition of Equation 5.8 and assumption specified by Equation 5.9. Since measurements are used with the reference model predictions to determine residuals, the square-root of the sum of residuals presents a RMS error, which is not Gaussian. In this section, we analyze the no-fault measurements distribution in detail to provide the methodology for determining a proper value of the threshold ε_i, as defined in Section 5.2.3.

In most cases, it is hard to obtain a reference model covering all operating conditions. To train a reference model after installation, a real-time decision of fault-free or faulty status is mandatory. In contrast to the steady-state and repetition uncertainty, the model uncertainty comes from the imperfections associated with any mathematical model. Here, we define average bias of the model estimation as the averaged residual between the model and the current measurement with no zero-mean noise. The model standard deviation, $\sigma_{i,\text{Model}}$, characterizes the model uncertainty. Since the zero-mean noise uncertainty ($\sigma_{i,\text{SS}}$) and model uncertainties ($\sigma_{i,\text{Model}}$) amplify the variability of residuals independently, it is reasonable to assume that no joint effect exists between the two uncertainties. Therefore, the covariance between the two uncertainties ($\sigma_{i,\text{SS}} \cdot \sigma_{i,\text{Model}}$) is zero, and $\sigma_{i,\text{NF}}$ will be a squared sum of $\sigma_{i,\text{SS}}$ and $\sigma_{i,\text{Model}}$ as shown in Equation 5.18. By combining Equation 5.18 and Table 5.3, $\sigma_{i,\text{Model}}$ can be estimated as shown in Table 5.4. Comparing Table 5.3 to Table 5.4, we can see that the reference model is the same order of magnitude as the steady-state and repeatability uncertainties.

$$\sigma_{i,\text{NF}} = \sqrt{\sigma_{i,\text{SS}}^2 + \sigma_{i,\text{Model}}^2} \tag{5.18}$$

Table 5.4. Net model uncertainties of the features using the 1st, 2nd, and 3rd order MPR models

Model uncertainties, $\sigma_{i,\text{Model}}$ (°C)	T_{sh}	T_{sc}	T_{E}	T_{D}	T_{C}	ΔT_{CA}	ΔT_{EA}
1st order MPR model	0.557	0.244	0.549	0.799	0.179	0.150	0.581
2nd order MPR model	0.328	0.197	0.147	0.319	0.047	0.040	0.131
3rd order MPR model	0.197	0.133	0.123	0.250	0.029	0.019	0.071

Equation 5.18 defines the overall uncertainties of the no-fault residual for one measurement. When a moving window average of n samples is used, the steady-state standard deviation is reduced by the square root of n as shown in Equation 5.19.

$$\sigma_{i,\text{SS}}\big|_{\text{MW}} = \frac{\sigma_{i,\text{SS}}}{\sqrt{n}} \tag{5.19}$$

Equation 5.19 will be applied throughout our calculations since $\sigma_{i,\text{SS}}$ in Table 5.4 is constant as determined in Section 3.2.3.

$$\sigma_{i,\text{SS}}\big|_{\text{MW}} = \frac{\sigma_i\big|_{\text{MW}}}{\sqrt{n-1}} \tag{5.20}$$

Since the model uncertainty, $\sigma_{i,\text{Model}}$, remains the same without regard to the moving window size, the no-fault total uncertainty for the moving window average will be,

$$\sigma_{i,\text{NF}}\big|_{\text{MW}} = \sqrt{\left(\frac{\sigma_{i,\text{SS}}}{\sqrt{n}}\right)^2 + \sigma_{i,\text{Model}}^2} \tag{5.21}$$

where n is the number of measurements in the moving window. Figure 5.8 compares the standard deviations of the three characteristics contributing to the total standard deviation: steady-state, 3$^{\text{rd}}$ order MPR model, and repeatability. As expected, steady-state uncertainty, $\sigma_{i,\text{SS}}$, shows the highest value for T_{sh}. The $\sigma_{i,\text{Model}}$ of T_{D} shows the highest value among the features, but the $\sigma_{i,\text{SS}}$ shows moderate variation. This means that the polynomial model has a higher uncertainty when estimating T_{D}, compared to the steady-state standard deviation. Some of this higher modeling standard deviation is due to the heat inertia of the compressor causing a higher time constant for T_{D}. This higher variation of T_{D} also appears in the $\sigma_{i,\text{Repeat}}$ having the largest value in Figure 5.8.
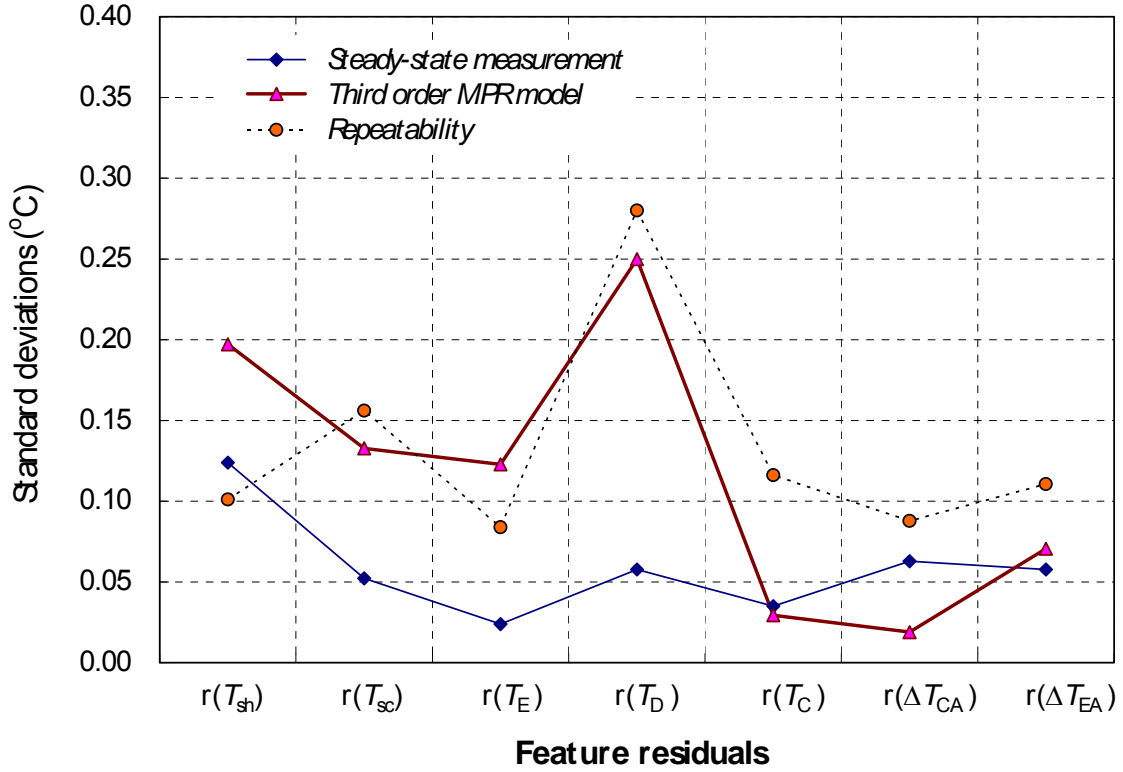
Figure 5.8. Standard deviations for seven feature residuals due to measurement noise at steady state, the 3rd order MPR model, and the lack of measurement repeatability

5.3.3 Combining uncertainties to determine the neutral case, NC, threshold

From sections 5.3.1 and 5.3.2, we observed uncertainties from the no-fault measurements. Considering that total uncertainty is due to steady-state uncertainty, modeling uncertainty, and lack of measurement repeatability uncertainty, the threshold is proportional to the total uncertainty as shown by Equation 5.22, where the constants k_1, k_2, and k_3 define the confidence intervals for each uncertainty.

$$\varepsilon_i = \sqrt{\left(k_1 \frac{\sigma_{i,\text{SS}}}{\sqrt{n}}\right)^2 + \left(k_2 \sigma_{i,\text{Model}}\right)^2 + \left(k_3 \sigma_{i,\text{Repeat}}\right)^2} \qquad (5.22)$$

Depending on the confidence level, the constants k_1, k_2, and k_3 can be determined based on the distribution for each uncertainty term.

5.3.3.1 Confidence interval, k_1, for the steady-state uncertainty

Since we use measurements and standard deviations in a preset moving window, their distribution depends on the characteristics of the moving window. When n no-fault data are sampled from a Gaussian distribution with standard deviation, σ_i, the quantity t can be defined by Equation 5.23.

$$t = \frac{x_i - \mu_i}{\sigma_i / \sqrt{n}} \qquad (5.23)$$

where μ_i is the current mean of the moving window of n samples. In such a case, t in Equation 5.23 follows a Student's t-distribution with $n - 1$ degrees of freedom. When we set a $1 - \alpha$ probability that the two values are equal ($x_i = \mu_i$), the confidence interval, $k_1 = t_{\alpha/2, n-1}$, is described by Equation 5.24.

$$P\left(|x_i - \mu_i| < t_{\alpha/2, n-1} \frac{\sigma_i}{\sqrt{n}}\right) = 1 - \alpha \tag{5.24}$$

where $t_{\alpha/2, n-1}$ is a two-sided confidence interval with $n - 1$ degrees of freedom. In Chapter 3, we determined the appropriate moving window size to be 140 seconds, or 10 samples in the moving window with a 14 second sampling interval. With a $1 - \alpha = 99\%$ confidence, the t-value, $t_{0.005,9}$, is 3.25, which is larger than a Gaussian distribution of 2.58. Table 5.5 shows the values of $k_1 = t_{\alpha/2, 9}$. Thus, constant k_1 in Equation 5.22 can be defined by Equation 5.25. For 99 % confidence (or credibility) level, k_1 is 3.25.

$$k_1 = t_{\alpha/2, n-1} \tag{5.25}$$

Table 5.5. Two-sided confidence intervals with degrees of freedom of four and nine

$1 - \alpha$ (%)	80.0	90.0	95.0	99.0
$\alpha/2$ (%)	10.0	5.0	2.5	0.5
$t_{\alpha/2,4}$[1]	1.533	2.132	2.776	4.604
$k_1 = t_{\alpha/2,9}$[2]	1.383	1.833	2.262	3.250

[1] 5 sample moving window
[2] 10 sample moving window

5.3.3.2 Confidence interval, k_2, for model uncertainty

Figure 5.9 shows the distribution of the T_{sh} residual using the 3rd order MPR model applied to the no-fault steady-state data discussed in Chapter 4. As seen in the plot, a Gaussian assumption tracks the residual distribution of the feature to a certain extent. However, residuals near zero are distributed narrower than a Gaussian. At high residual values where $|r(T_{sh})| > 1.7 \,°C$ (3 °F), a Gaussian assumption underestimates the probability. From the Gaussian approach, 99 % of data fall within the range of $\pm 0.6\,°C$ (1.08 °F), but no-fault test data have a wider range of $\pm 0.78\,°C$ (1.41 °F) to cover 99 % of all data.

Equation 5.26 shows the normalized 99 % confidence intervals for a Gaussian assumption. In Equation 5.27, normalized 99 % confidence intervals of each feature residual are shown based upon the experimental data. Any bounds greater than an absolute value of 2.58 in the experimental results imply that the measurements have a wider 99 % distribution than the infinitely sampled Gaussian assumption.
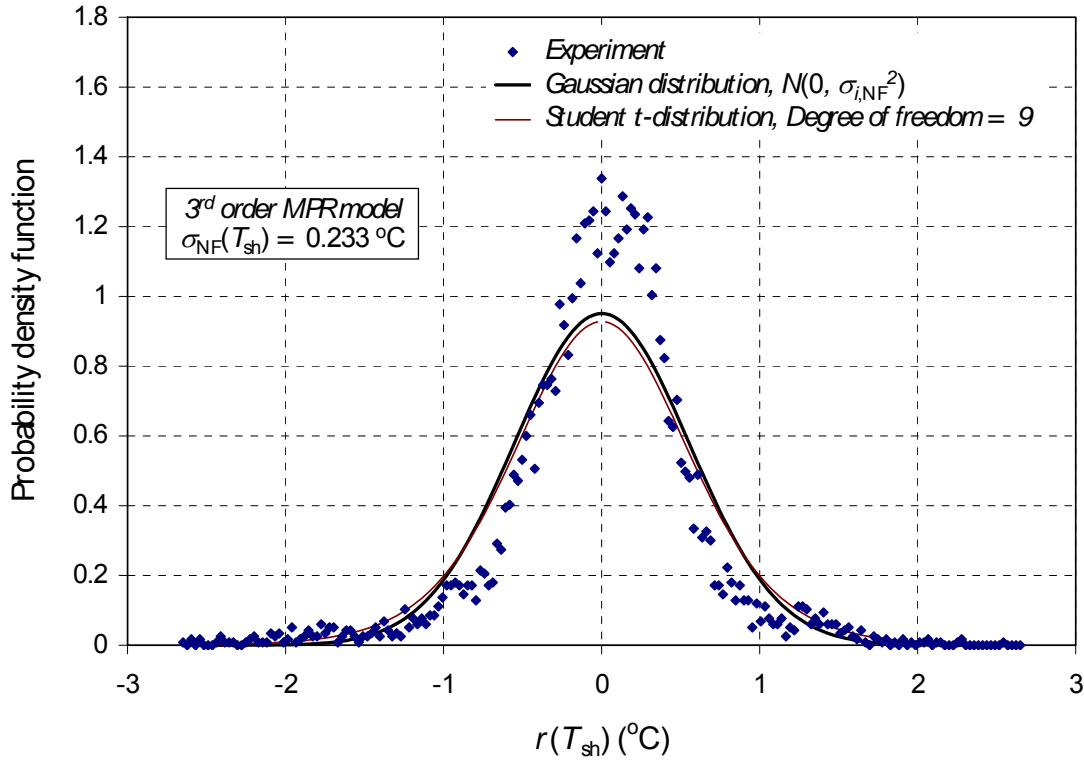
Figure 5.9. Comparison of the distributions of the T_{sh} residuals from no-fault steady-state data and 3rd order MPR model based on the model RMS error; Gaussian distribution, student t-distribution, and the calculated distribution from the test data.

Gaussian distribution: $\qquad -2.58 < \dfrac{r_i}{\sigma_{i,\mathrm{NF}}} < 2.58$ $\qquad$ (5.26)

Experiment: $\qquad -3.37 < \dfrac{r(T_{sh})}{\sigma_{\mathrm{NF}}(T_{sh})} < 3.37$ $\qquad$ (5.27a)

$$-3.03 < \frac{r(T_{sc})}{\sigma_{\mathrm{NF}}(T_{sc})} < 3.03 \qquad (5.27b)$$

$$-2.96 < \frac{r(T_{\mathrm{E}})}{\sigma_{\mathrm{NF}}(T_{\mathrm{E}})} < 2.96 \qquad (5.27c)$$

$$-2.65 < \frac{r(T_{\mathrm{D}})}{\sigma_{\mathrm{NF}}(T_{\mathrm{D}})} < 2.65 \qquad (5.27d)$$

$$-2.63 < \frac{r(T_{\mathrm{C}})}{\sigma_{\mathrm{NF}}(T_{\mathrm{C}})} < 2.63 \qquad (5.27e)$$

$$-2.64 < \frac{r(\Delta T_{\mathrm{CA}})}{\sigma_{\mathrm{NF}}(\Delta T_{\mathrm{CA}})} < 2.64 \qquad (5.27f)$$

$$-3.22 < \frac{r(\Delta T_{\mathrm{EA}})}{\sigma_{\mathrm{NF}}(\Delta T_{\mathrm{EA}})} < 3.22 \qquad (5.27g)$$

As shown by comparing the confidence intervals of Equation 5.26 and Equations 5.27, applying the infinite degree of freedom Gaussian confidence interval would underestimate the threshold ε_i. Table 5.6 lists the confidence intervals for three confidence levels.

Table 5.6. Two-sided confidence interval of the seven features for the 3rd order MPR model

$1 - \alpha$ (%)		75.0	97.5	99.5
$k_2 = t_{\alpha/2,\,n-1}$	T_{sh}	1.00	2.26	2.96
	T_{sc}	0.93	2.22	3.37
	T_{E}	1.10	2.06	2.65
	T_{D}	1.15	1.96	2.63
	T_{C}	1.03	2.03	3.03
	ΔT_{CA}	1.14	1.95	2.64
	ΔT_{EA}	0.95	2.16	3.22

5.3.3.3 *Confidence interval, k_3, for lack of measurement repeatability*

Repetitive measurements of a random variable will follow a Gaussian distribution, thus, under similar measurement conditions, repetitively measured feature residuals will also follow a Gaussian distribution. Table 5.7 shows the confidence interval with regard to the confidence level for a Gaussian distribution at various confidence levels. Thus, constant k_3 in Equation 5.22 is defined by the Gaussian confidence interval in Equation 5.28. For example, with 99 % credibility, k_3 equals 2.576 as shown below.

$$k_3 = g_{\alpha/2} \tag{5.28}$$

Table 5.7. Two-sided confidence intervals of Gaussian distribution

$1 - \alpha$ (%)	75.0	80.0	85.0	90.0	95.0	97.5	99.0	99.5	99.75	99.9	99.95
$k_3 = g_{\alpha/2}$	1.156	1.282	1.445	1.645	1.960	2.241	2.576	2.807	3.024	3.291	3.481

5.3.4 Neutral case, NC, threshold value for the required credibility

In the previous sections we defined the confidence intervals k_1, k_2, and k_3 for each uncertainty term as defined by Equations 5.24, 5.27, and 5.28. With this, the thresholds, ε_i, at any given level of confidence may be calculated using Equation 5.21. Table 5.8(a) and 5.8(b) list the feature thresholds with 50 %, 95 % and 99 % credibility for the moving window size of 5 and 10 samples.

Table 5.8. Feature thresholds at different confidence levels for two sample sizes

(a) Moving window of 5 samples

Threshold of the features	T_{sh}	T_{sc}	T_E	T_D	T_C	ΔT_{CA}	ΔT_{EA}
50 % credibility, $\varepsilon_{i,0.50}$ (°C)	0.131	0.134	0.092	0.243	0.082	0.064	0.086
95 % credibility, $\varepsilon_{i,0.95}$ (°C)	0.504	0.413	0.324	0.756	0.239	0.192	0.274
99 % credibility, $\varepsilon_{i,0.99}$ (°C)	0.758	0.579	0.426	0.987	0.317	0.265	0.383

(b) Moving window of 10 samples

Threshold of the features	T_{sh}	T_{sc}	T_E	T_D	T_C	ΔT_{CA}	ΔT_{EA}
50 % credibility, $\varepsilon_{i,0.50}$ (°C)	0.130	0.134	0.092	0.243	0.082	0.064	0.086
95 % credibility, $\varepsilon_{i,0.95}$ (°C)	0.496	0.411	0.323	0.755	0.237	0.187	0.271
99 % credibility, $\varepsilon_{i,0.99}$ (°C)	0.735	0.574	0.424	0.983	0.313	0.248	0.373

5.4 Application of the FDD Algorithm to a Residential Heat Pump Operating in the Cooling Mode

5.4.1 Implementing single faults

Table 5.9 lists the six types of faults investigated. The online classification of the presence of non-condensable gases is not included in this study, since it can be diagnosed by checking its partial pressure while the system is off (Stylianou and Nikanpour, 1996; Li, 2004). Implementation of the seven artificial faults was detailed in Chapter 3.

Table 5.9. Description of studied faults

Fault	Abbr.	Determination of level of fault during tests
Compressor leakage (4-way valve leakage)	CMF	% of refrigerant flow rate
Improper outdoor air flow rate	CF	% of coil area blocked
Improper indoor air flow rate	EF	% of correct air flow rate
Liquid line restriction	LL	% of normal pressure drop through TXV
Refrigerant overcharge	OC	% overcharge from the correct charge
Refrigerant undercharge	UC	% undercharge from the correct charge

5.4.2 Quantifying the control limits of the TXV

When the TXV is fully open, it behaves like a fixed area expansion device; thus, any faults that occur during this time will affect system features differently than they would if the TXV were within its normal control range. For this reason, the cooling mode TXV's control limits must be assessed so that appropriate feature rule-sets may be developed for the various realms of TXV operation. The delineation of these TXV control realms is aided by correlation of the refrigerant mass flow rate to measured system features.

The cooling mode TXV experiences a large range of inlet refrigerant conditions and must control evaporator exit superheat over a broad range of refrigerant mass flow rates; thus selection of the appropriate TXV is somewhat of an art aided by extensive experimental knowledge. The TXV may reach its control limits when two-phase refrigerant is present or more/less refrigerant flow is required by its superheat setting. Since the TXV is working as a superheat controller, its characteristic behavior should be quantified as a means of assessing its control limits. Equation 5.29 is a simple formulation of mass flow rate via isenthalpic expansion

$$m_{\mathrm{R}} = C_d A \sqrt{\rho_{\mathrm{TXV.up}} \Delta P_{\mathrm{TXV}}} \tag{5.29}$$

where C_d is a characteristic flow coefficient; A is the area, which is a function of valve stem displacement; $\rho_{\mathrm{TXV.up}}$ is TXV upstream refrigerant density; and ΔP_{TXV} is pressure drop across the TXV. For the case of two-phase refrigerant at the inlet of the TXV, an accurate mass flow measurement is required in order to determine the appropriate value of $C_d A$.

Since two-phase refrigerant flow degrades or completely prevents accurate measurement of refrigerant mass flow through the Coriolis type meter used in this study, mass flow is estimated indirectly using a compressor map when TXV upstream subcooling ($T_{\mathrm{sc\_TXV.up}}$) is below 0.5 °C. Equation 5.30 presents the form of the mass flow equation provided by manufacturers according to ANSI/ARI Standard 540 (ARI 2004).

$$\begin{aligned} m_{\mathrm{R}} = {} & c_1 + c_2 T_{\mathrm{S.sat}} + c_3 T_{\mathrm{D.sat}} + c_4 T_{\mathrm{S.sat}}^2 + c_5 T_{\mathrm{S.sat}} T_{\mathrm{D.sat}} + \\ & c_6 T_{\mathrm{D.sat}}^2 + c_7 T_{\mathrm{S.sat}}^3 + c_8 T_{\mathrm{S.sat}}^2 T_{\mathrm{D.sat}} + c_9 T_{\mathrm{S.sat}} T_{\mathrm{D.sat}}^2 + c_{10} T_{\mathrm{D.sat}}^3 \end{aligned} \tag{5.30}$$

To increase the usefulness of Equation 5.30, Dabiri and Rice (1981) suggested Equation 5.31 to adjust mass flow rate when the compressor suction superheat is different from the standard conditions.

$$\frac{m_{\mathrm{R}}}{m_{\mathrm{R.map}}} = 1 + 0.75 \left(\frac{\rho_{\mathrm{S}}}{\rho_{\mathrm{S.map}}} - 1 \right) \tag{5.31}$$

The compressor map was created at a standard suction superheat ($T_{\mathrm{S.sh}}$) of 11.1 °C (20.0 °F). Figure 5.10 shows calculated and measured refrigerant mass flow rate with $T_{\mathrm{sc\_TXV.up}} > 0.5$ °C for suction superheats of 10.2 °C to 13.7 °C (18.4 °F to 24.6 °F). All the measurements are well estimated within a ±5 % deviation. This figure indicates that these two equations are accurate estimators of mass flow rate and that they should be applicable even when two-phase conditions exist at the TXV inlet.

In order to characterize the control limits of the TXV, refrigerant flow rate is calculated with Equations 5.30 and 5.31 when the upstream is two-phase as defined by a $T_{\mathrm{sc\_TXV.up}} < 0.5$ °C. In this case, thermodynamic properties including refrigerant enthalpy and mass quality upstream of the TXV are estimated by an energy balance calculation on the condenser air-side. Two-phase density is calculated using mass quality and a harmonic weight of saturated liquid and vapor densities.
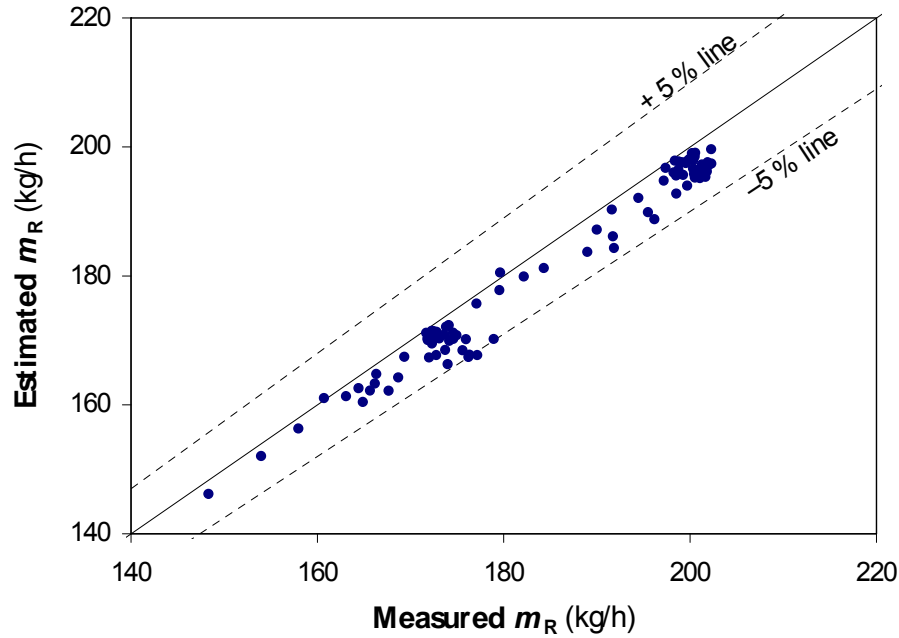
Figure 5.10. Estimation of refrigerant mass flow rate at $\Delta T_{sc\_TXV.up} > 0.5\ °C$ using the compressor map with superheat correction by Dabiri and Rice (1981)

Figure 5.11 shows C_dA with respect to T_{sh} at the evaporator exit. Note that the level of T_{sh} in Figure 5.11 measured at the evaporator exit is smaller than the compressor suction superheat due to heat transfer within the TXV. When T_{sh} is below 9 ºC (zone A), C_dA and T_{sh} show a linear trend where the TXV successfully controls T_{sh}. But in some cases of single-phase and two-phase conditions, the TXV cannot change the superheat because it is fully open (zone B). This condition is known as actuator saturation.

In most cases, TXV saturation occurs when there is two-phase refrigerant upstream; however, actuator saturation also occurs at subcooled upstream conditions due to a non-condensable gas fault. Non-condensable gas collects on the high pressure side of the system and raises the condensing pressure. If non-condensable gas passes through the TXV or so much non-condensable is present that the discharge pressure is forced abnormally high, the TXV can reach its control limits even though the refrigerant is in a subcooled state. In zone B, C_dA does not increase with T_{sh}. Applying Bernoulli's orifice equation, Equation 5.29, to two-phase flow, underestimates mass flow rate through an expansion valve (Aaron and Domanski, 1989). Considering that C_dA is estimated by Equation 5.29 with the homogeneous two-phase assumption, C_dA values in zone B are located below the horizontal line which represents the maximum C_dA of zone A.

From Figure 5.11, when the TXV is saturated, C_dA is near constant, and the TXV is working like a fixed expansion device. Therefore, the fault characteristics of a system with a TXV should be observed in zone A and B, separately.
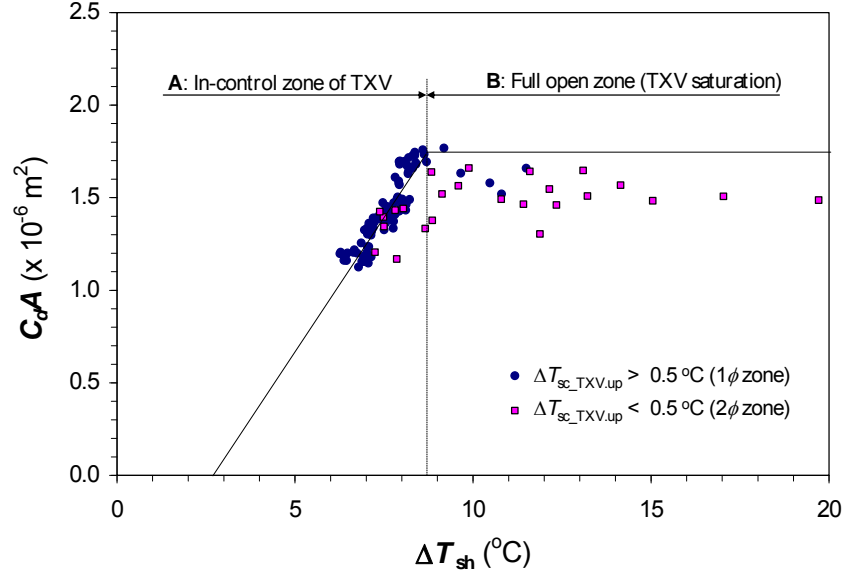
Figure 5.11. C_dA from Equation 5.29 versus T_{sh} for the selected tests

5.4.3 Building a rule-based chart

Figure 5.12 shows a comparative presentation of the effects of single faults on the seven parameters at test condition #5 (T_{OD} = 27.8 °C (82.0 °F), T_{ID} = 26.7 °C (80.0 °F), and RH_{ID} = 50 %) (as in Table 3.3 of Kim et al. 2006). The standard deviations, σ's, of the various features are listed in Table 3.3. Some features show clearly increasing or decreasing trends, but some show little change within a standard deviation.

ΔT_{LL} can be a good indicator that shows whether the condenser exit is in two-phase or single-phase. However, ΔT_{LL} is not a rapidly changing feature when subcooled refrigerant at the condenser exit flashes into two-phase during liquid line migration. In addition, the degree of ΔT_{LL} highly depends upon ΔT_{sc} and ΔP_{LL}. Thus, a two-phase condition upstream does not always guarantee the TXV being saturated or fully open. This is observed also in Figure 5.11, where T_{sh}'s in a number of conditions are well controlled at $T_{sc\_TXV.up}$ < 0.5 °C. Thus, ΔT_{LL} is not selected as a feature of the FDD system in this study, though it is useful for some typical faults like liquid line restriction.

Based on the bounds defined by the model standard deviations (dashed lines on the figure), rules for each feature can be determined as in Table 5.2. The rule-based chart in Table 5.2 uses three residual indices of no-change (–), positive-change (↑), negative-change (↓). By using the no-change index, the no-fault case can also be included in the rule-based chart thus creating a complete FDD algorithm that deals with all possible residual states. Even if a fault case is within the no-fault threshold and is assigned a no-change value for a particular fault level, as the fault level increases, the residual may move out of the no-fault threshold bounds. In such a case, the changed case should be properly adjusted to positive/negative-change.

This re-assignment of case indices within the rule set for a particular fault occurs during TXV saturation as mentioned in Figure 5.8; the rule set was separated into zone A and B. Note that the residual of T_{sh} has no change in zone A but increases in zone B. TXV saturation is not observed within the test range for compressor valve leakage, improper indoor air flow, or refrigerant overcharge faults. The rule set for the liquid-line restriction fault were all NC indices for zone A.
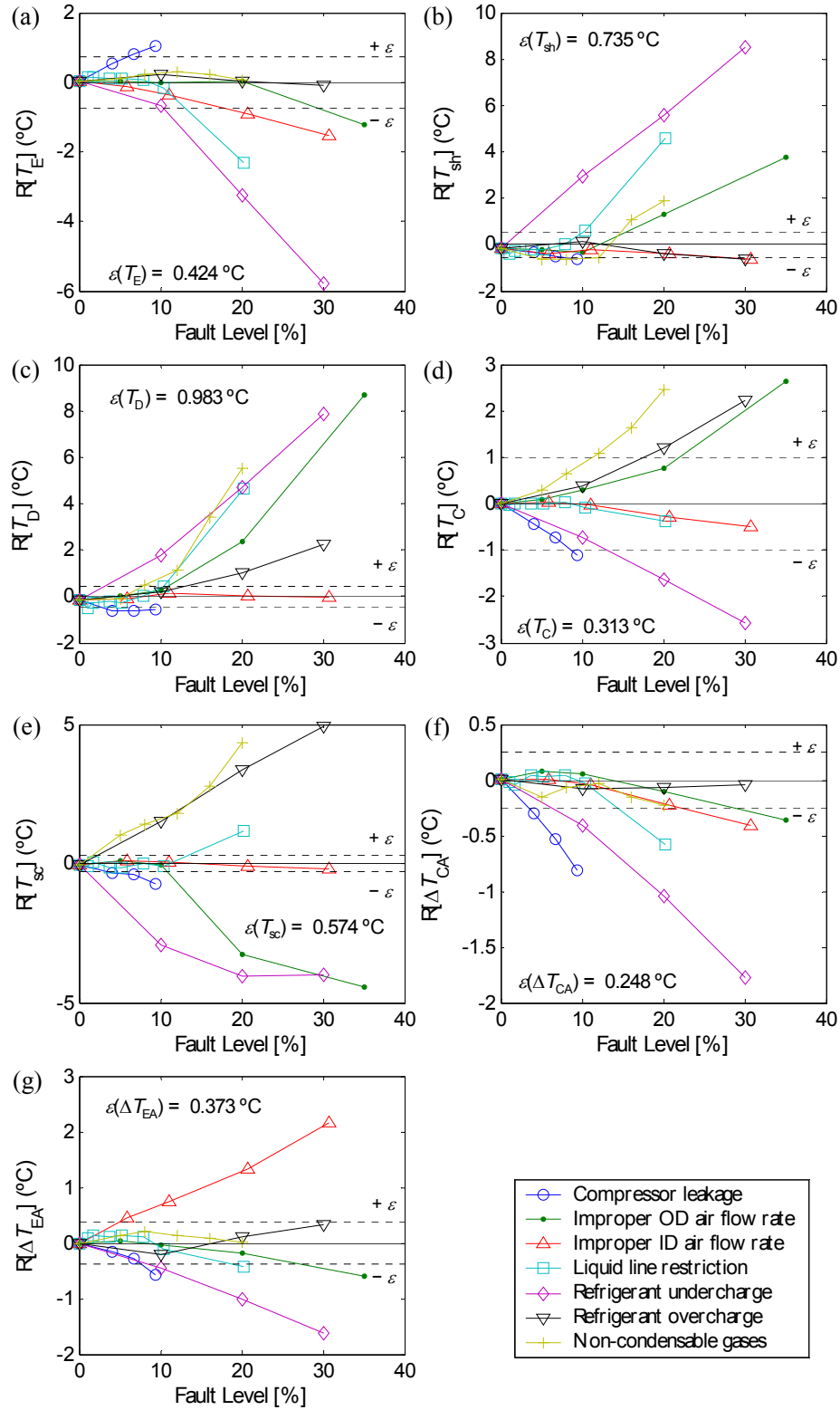
Figure 5.12. Residuals of seven parameters for different faults. (Test #5: T_{OD} = 27.8 °C (82.0 °F), T_{ID} = 26.7 °C (80.0 °F), and RH_{ID} = 50 %): Residual of (a) T_E, (b) T_{sh}, (c) T_D, (d) T_C, (e) T_{sc}, (f) ΔT_{CA}, and (g) ΔT_{EA} (Kim et al. 2006)

5.4.4 Example FDD module

Appendix A presents screenshots of the FDD modules comprising the entire FDD system. Figure 5.13 shows the main interface window of the FDD module developed under this study. Moving Window Module (A.2), Steady-state Detector Module (A.3), Preprocessor Module (A.4), No-fault MPR Reference Module (A.5 and A.6), and Statistical Rule-based FDD Module (A.7) are running in the background while the main module is running.

In Figure 5.13, sample operation at a 20 % reduced indoor air flow fault is demonstrated. The moving window average is manipulated through the moving window module at the left hand side. Based on the MPR model, feature residuals is calculated and fed into Rule-based FDD Module, which indicates on-going fault. In the meanwhile, Preprocessor Module calculates real-time EER, from which EER degradation is evaluated. From the FDD Module, we can see the EER degradation warning is ON and improper indoor air flow fault (EF) is properly diagnosed.
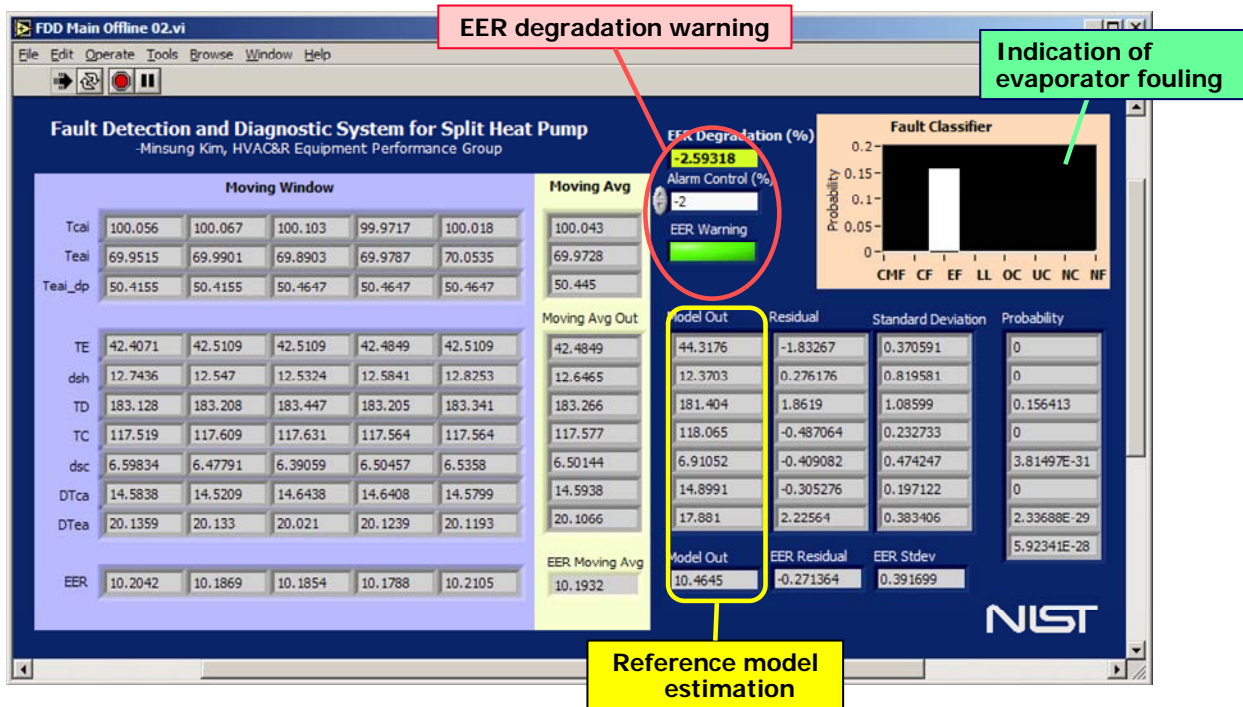
Figure 5.13. Main interface window of the FDD system indicating an improper indoor air flow fault.

The flow diagram in Fig. 5.14 shows a working algorithm for the FDD system in Figure 5.13. After a steady state is identified, NFSS parameters are calculated using the operating condition as input parameters. When the performance degradation parameter, in this case EER, is over the high limit in the fault detection module, the system is regarded to be faulty and the detailed fault status is analyzed in the fault diagnostic modules. In this research, the fault detection alarm is activated when EER is degraded more than 3.0 % below the NFSS reference EER value. Then the appropriate rule-based chart is determined based upon whether or not the TXV is in control or out of control. The TXV status is evaluated, as in Figure 5.11, from the degree of subcooling at the TXV upstream (greater than or less than 0.5 °C). Based on the rule-based chart and the fault calculation algorithm in sections 5.2 and 5.3, the current fault is identified in the fault diagnostic module.

Starting FDD

Operating condition: T_{OD}, T_{ID}, $T_{ID,dew}$

Field measurements

Steady-state Detector — **Steady-state?** → yes

Reference Module — **No-fault Reference Model**

$EER_{model} - EER_{system} < \varepsilon$ → yes

No

Calculate feature residuals

$\Delta T_{sc\_TXV.up} > 0.5\ ^{\circ}C$ (TXV in control) → yes

No

Rule-based chart in zone B

Rule-based chart in zone A

FDD Modules

Rule-based FDD Analysis

Fault Diagnosis

End of FDD
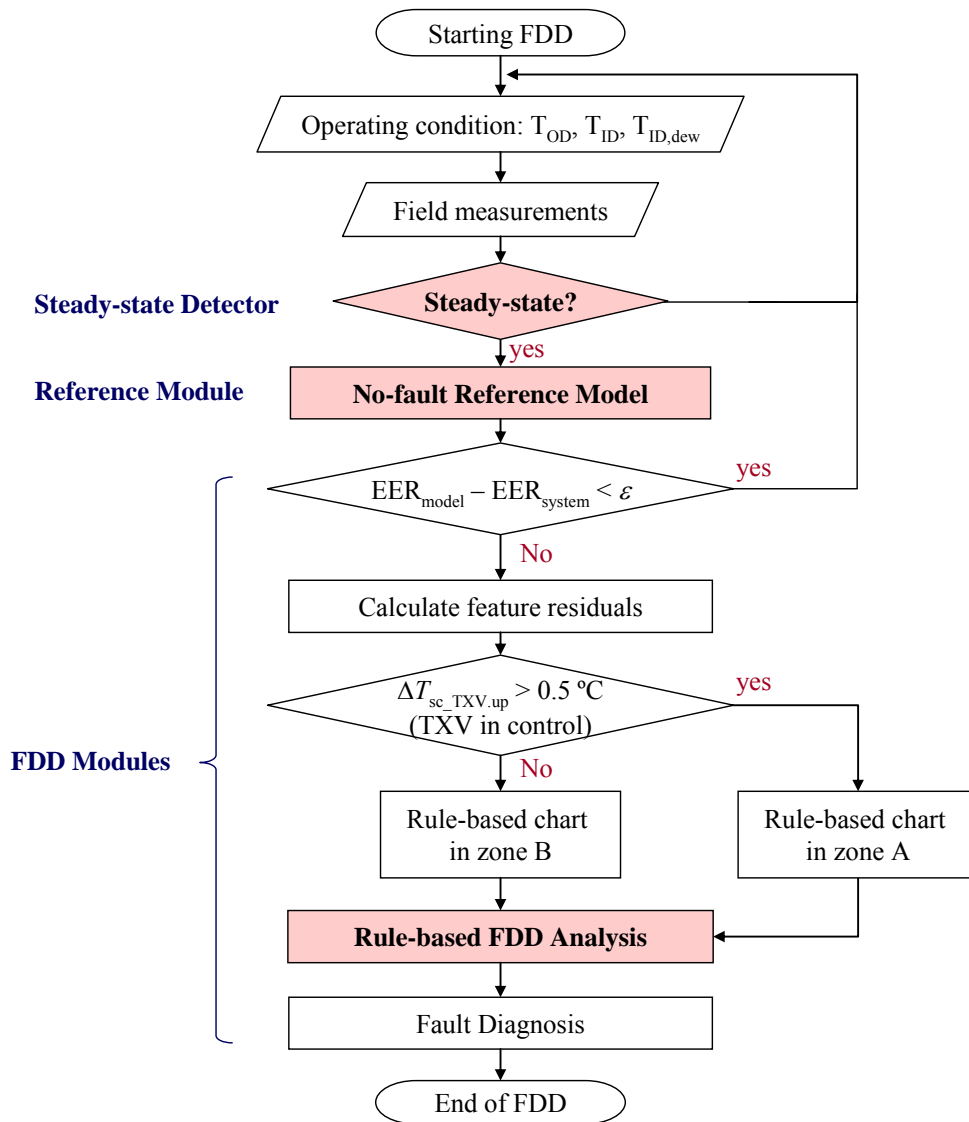
Figure 5.14. Sequential algorithm of the sample FDD system

5.5 Performance of the FDD System

5.5.1 Comparative evaluation of fault effects on cooling capacity and EER

For the validation of the FDD algorithm, the experimental data in Kim et al. (2006) were utilized. The six single-fault cases–compressor leakage, improper OD air flow rate, improper ID air flow rate, liquid-line restriction, refrigerant undercharge, and refrigerant overcharge–were tested. Seventeen combinations of indoor and outdoor conditions in Table 5.10 were selected as experimental conditions.

Table 5.10. Operating conditions for FDD tests from Kim et al. (2006)

Test number	Indoor		Outdoor	
	Dry-bulb temp. °C (°F)	Relative humidity %	Dry-bulb temp. °C (°F)	Relative humidity %
1*	26.7 (80.0)	51	35.0 (95.0)	40 to 60
2	21.1 (70.0)	50	21.1 (70.0)	40 to 60
3	26.7 (80.0)	50	21.1 (70.0)	40 to 60
4**	21.1 (70.0)	50	27.8 (82.0)	40 to 60
5**	26.7 (80.0)	50	27.8 (82.0)	40 to 60
6	21.1 (70.0)	50	32.2 (90.0)	40 to 60
7	26.7 (80.0)	50	32.2 (90.0)	40 to 60
8**	21.1 (70.0)	50	37.8 (100.0)	40 to 60
9**	26.7 (80.0)	50	37.8 (100.0)	40 to 60
10	21.1 (70.0)	dry coil	21.1 (70.0)	40 to 60
11	26.7 (80.0)	dry coil	21.1 (70.0)	40 to 60
12	21.1 (70.0)	dry coil	27.8 (82.0)	40 to 60
13	26.7 (80.0)	dry coil	27.8 (82.0)	40 to 60
14	21.1 (70.0)	dry coil	32.2 (90.0)	40 to 60
15	26.7 (80.0)	dry coil	32.2 (90.0)	40 to 60
16	21.1 (70.0)	dry coil	37.8 (100.0)	40 to 60
17	26.7 (80.0)	dry coil	37.8 (100.0)	40 to 60

* ARI Standard 210/240 (2006) rating point
** Combination of test conditions selected for fault tests except improper ID air flow rate fault

The test data show to what extent faults effect cooling capacity and EER and at what ambient temperature conditions particular faults have the greatest effect. Cooling loads are proportional to the indoor and outdoor temperature difference or temperature lift. The highest to lowest temperature lift occurs with test conditions $8 > 9 > 4 > 5$. Cooling capacity, Q_{ER} in Figure 5.15(a), is highest to lowest with test condition $5 > 9 > 4 > 8$. This illustrates that the system produces the highest capacity at the minimum temperature lift. The EER in Figure 5.15(b) is inversely proportional to the temperature lift. We have seen from our testing that the feature residuals will show the most distinctive impact at the high capacity, test #5, conditions where the temperature lift is the lowest, and EER is the highest.
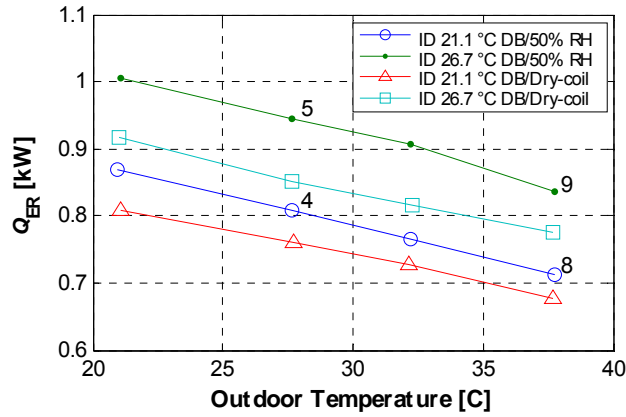
(a) Cooling capacity
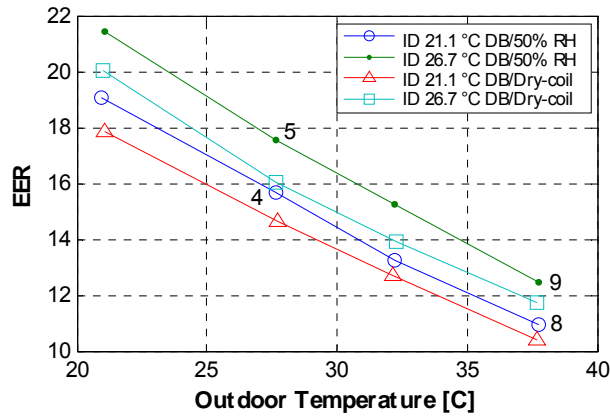
(b) EER

Figure 5.15. Variation of system performance under fault-free conditions

Figure 5.16 presents a histogram of estimated fault levels that would cause a 5 % reduction in EER relative to the fault-free EER. The bars marked by an asterisk represent linear extrapolation of fault levels to those which would cause a 5 % degradation in EER. EER is relatively robust with evaporator fouling or refrigerant overcharge faults. For a refrigerant overcharge fault, the fault level is more sensitive at the highest temperature lift seen with test #8. This is because higher operating temperature raises optimum refrigerant charge. Since a high temperature lift adversely effects capacity, EER degradation is more sensitive to fault level at a higher capacity (low lift test #5) but less sensitive at a lower capacity (higher temperature lift test #8) for all faults except evaporator fouling or refrigerant overcharge. All faults, except the compressor leakage fault, must have a fault level greater than 10 % to produce a 5 % decrease in EER.

Figure 5.17 presents estimated EER degradation relative to the fault-free EER at a 10 % level compressor fault and a 20 % fault level for the remaining five faults. With a 20 % improper refrigerant charge, undercharge causes more EER degradation than overcharge, especially at the lowest temperature lift occurring for test #5. EER degradation is greater when T_{ID} is at 26.7 °C than at 21.1 °C.
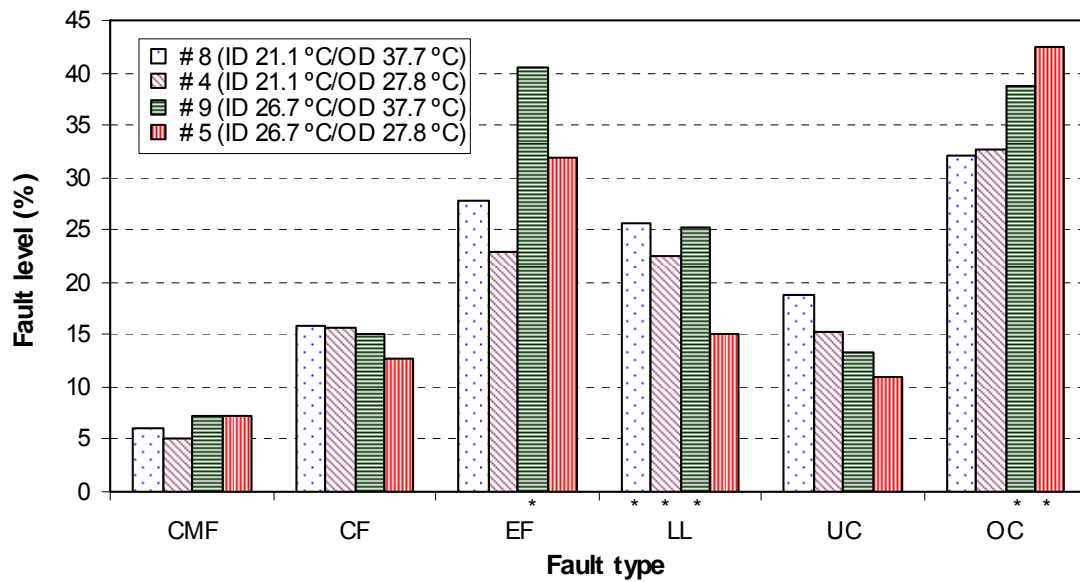
Figure 5.16. Estimated single-fault levels for a 5 % degradation in EER at four different operating conditions. ('*' below the *x*-axis bars represents linear extrapolation beyond the test condition bounds)
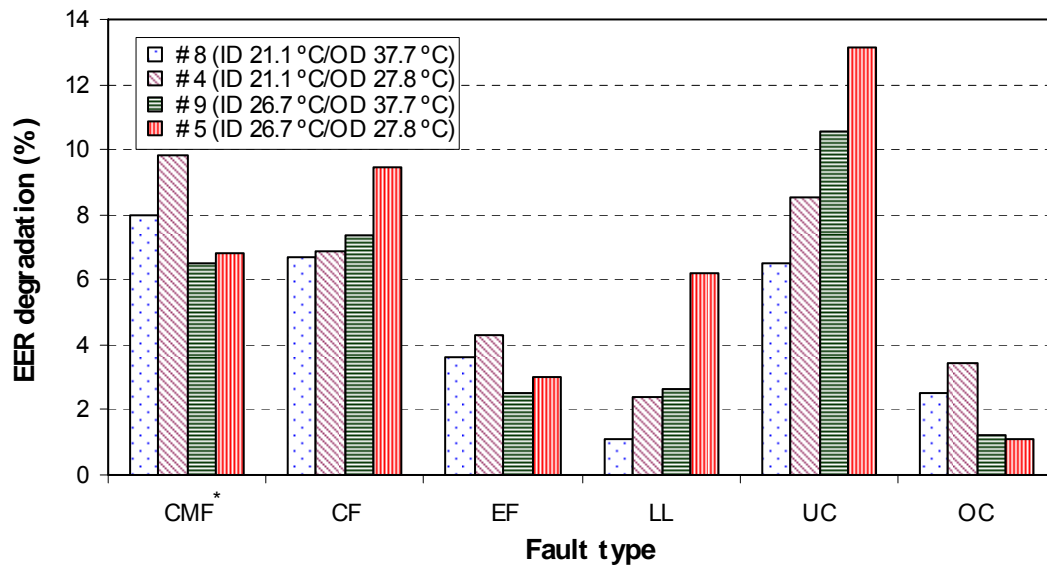
Figure 5.17. Estimated EER degradation for a 10 % compressor fault level and a 20 % fault level for the remaining faults

5.5.2 Example implementation of the FDD system

Performance of the FDD system was verified using the steady-state data in Kim et al. (2006). The NFSS reference model trained through the random operations in Chapter 4 were applied as a base to the FDD system. The considerations of the FDD system in this section are listed as follows.

  - EER warning alarm : 3 % EER degradation from the NFSS reference value.
  - NFSS reference model: The 3rd order multivariate polynomial model.
  - Isolation of diagnosed system status: The case of the maximum probability more than 3 times of the second high probability. Otherwise, the case regarded as undetermined.
  - Constant s in Equation 5.10: $s = 2.0$

Table 5.11 presents diagnostic results of no fault cases using the FDD system built in section 5.4.4. From Table 5.11, no fault cases were well diagnosed by the FDD system. EER degradations in Table 5.11 is not zero even though the cases were set to zero fault level. This is because the reference EER is generated by the NFSS model which had non-zero mean square error for the regression.

Table 5.11. FDD results for no fault (NF) cases

Test condition	Diagnosed system status	TXV zone	EER warning	EER degradation (%)	Probability for each case						
					Compressor Leakage (CMF)	Improper OD air flow rate (CF)	Improper ID air flow rate (EF)	Liquid-line restriction (LL)	Refrigerant undercharge (UC)	Refrigerant overcharge (OC)	No Fault (NF)
2	NF	A	0	-0.26	2.88E-21	8.45E-19	9.73E-14	7.68E-36	1.86E-14	8.34E-14	0.27146
3	NF	A	0	0.05	4.68E-23	3.32E-14	1.15E-10	1.23E-10	8.29E-16	1.07E-04	0.00320
4	NF	A	0	0.19	3.37E-16	4.24E-13	3.81E-12	5.42E-16	8.22E-11	1.32E-07	0.91963
5	NF	A	0	-0.06	1.80E-16	1.55E-14	1.09E-11	2.02E-22	3.61E-10	4.60E-11	0.91433
6	NF	A	0	-1.35	1.28E-16	3.99E-17	2.31E-07	8.93E-16	1.21E-11	8.36E-08	0.69309
7	NF	A	0	0.10	1.90E-29	2.11E-16	2.83E-23	1.63E-40	9.74E-27	4.04E-07	0.08289
8	NF	A	0	-0.06	6.24E-17	4.02E-14	2.22E-11	1.46E-20	1.24E-11	5.36E-09	0.96387
9	NF	A	0	0.04	4.17E-16	6.68E-14	8.62E-11	4.63E-17	7.81E-11	4.09E-08	0.95847
10	NF	A	0	-0.17	8.00E-18	4.16E-14	3.52E-14	1.15E-25	1.40E-10	8.59E-13	0.77679
11	NF	A	0	0.38	3.99E-16	1.94E-13	1.23E-13	5.72E-23	1.51E-10	4.41E-10	0.88323
12	NF	A	0	-0.20	8.08E-18	1.01E-15	3.23E-09	2.00E-17	3.00E-13	1.03E-06	0.89601
13	NF	A	0	-0.28	6.08E-17	1.76E-15	5.61E-11	1.97E-24	1.08E-09	4.98E-13	0.81954
14	NF	A	0	0.10	3.26E-17	6.46E-15	1.96E-10	1.94E-20	3.47E-13	3.81E-08	0.88826
15	NF	A	0	1.06	9.05E-16	7.05E-14	1.96E-15	3.56E-28	1.09E-09	6.52E-13	0.56744
16	NF	A	0	0.42	8.41E-16	1.05E-12	1.63E-13	1.14E-18	6.47E-10	3.15E-09	0.90353
17	NF	A	0	-0.61	2.48E-18	1.77E-15	9.79E-11	3.65E-22	9.61E-13	3.98E-09	0.93935

Table 5.12 thru Table 5.17 present detection and diagnostic results for six single faults. The no-fault threshold, ε, confidence level was set at 99 % for all results shown below. The probability of each fault was calculated according to the method outlined in Section 5.2 with Equations 5.12 and 5.17 implemented according to the rule-chart of Table 5.2 (repeated here for ease of reference). The probability of a given fault was the product of the probabilities of each case as represented in a row of the rule-chart, which includes the no-fault or neutral (NC) case.

Table 5.2 (repeated here). Rule-based fault pattern chart of seven features

Fault Type	zone[1]	T_E	T_{sh}	T_D	T_C	T_{sc}	ΔT_{CA}	ΔT_{EA}
Compressor valve leakage[2] (CMF)	A	↑	–	↑	↓	↓	↓	↓
Improper outdoor air flow (CF)	A	↑	–	↑	↑	↓	–	↓
	B	↓	↑	↑	↑	↓	↓	↓
Improper indoor air flow[2] (EF)	A	↓	–	–	↓	–	↓	↑
Liquid-line restriction[3] (LL)	A	–	–	–	–	–	–	–
	B	↓	↑	↑	↓	↑	↓	↓
Refrigerant undercharge (UC)	A	–	–	–	↓	↓	↓	↓
	B	↓	↑	↑	↓	↓	↓	↓
Refrigerant overcharge[2] (OC)	A	–	–	↑	↑	↑	–	–
No-fault	–	–	–	–	–	–	–	–

[1] Zone A: $T_{sh} < 9$ °C, Zone B: $T_{sh} > 9$ °C

[2] The case of $T_{sh} > 9$ °C was not observed within the fault levels of this study.

[3] The rules when $T_{sh} < 9$ °C were identical with no-fault cases.

Table 5.12 shows the performance of the FDD system with a compressor valve leakage fault (CMF) at four different fault levels and four different test conditions (#4, #5, #8, and #9) with the TXV in superheat zone A as shown in Figure 5.10. At fault levels greater than 5 %, the FDD system made a correct detection and diagnosis. At fault levels less than 5 %, no-fault (NF) and undercharged fault (UC) were incorrectly indicated. For test condition #4 at a fault level of 2.5 %, EER was degraded by 3.4 % while the FDD system indicated NF. As fault level increased to 5 %, the compressor fault was correctly detected and diagnosed while EER degraded by 5.5 %. For test condition #8, the 2.5 % CMF was not detected with an EER degradation of 2.5 %. For test condition #9, the 2.4 % CMF was incorrectly detected and diagnosed as an UC fault while EER was degraded by 1.3 %.

Table 5.12. FDD results for compressor leakage fault (CMF)

Test condition	Fault level	Diagnosed system status	TXV zone	EER warning	EER degradation (%)	Probability for each case						
						Compressor Leakage (CMF)	Improper OD air flow rate (CF)	Improper ID air flow rate (EF)	Liquid-line restriction (LL)	Refrigerant undercharge (UC)	Refrigerant overcharge (OC)	No Fault (NF)
4	2.5	NF	A	1	-3.40	2.52E-08	3.33E-19	1.26E-15	4.15E-19	1.99E-06	1.01E-16	0.0133
4	5.0	CMF	A	1	-5.51	2.05E-05	0	0	0	1.54E-08	0	3.53E-20
4	9.3	CMF	A	1	-8.88	0.015091	0	0	0	0	0	0
4	11.4	CMF	A	1	-10.84	0.209672	0	0	0	0	0	0
5	4.0	CMF	A	1	-3.20	9.35E-13	0	0	0	3.11E-13	0	1.73E-26
5	6.7	CMF	A	1	-5.53	6.12E-12	0	0	0	0	0	0
5	9.5	CMF	A	1	-7.39	3.45E-11	0	0	0	0	0	0
5	27.2	CMF	A	1	-23.03	0.385201	0	0	0	0	0	0
5	38.2	CMF	A	1	-33.50	0.378976	0	0	0	0	0	0
8	2.5	NF	A	0	-2.53	1.24E-07	4.38E-21	1.93E-21	2.89E-26	7.21E-05	2.80E-23	0.000226
8	5.5	CMF	A	1	-4.95	0.000691	0	0	0	2.35E-11	0	3.76E-33
8	9.0	CMF	A	1	-7.92	0.096084	0	0	0	0	0	0
9	2.4	UC	A	0	-1.28	3.53E-07	0	1.31E-18	1.08E-23	5.07E-05	0	1.41E-07
9	5.6	CMF	A	1	-3.89	1.61E-05	0	0	0	8.79E-07	0	0
9	8.9	CMF	A	1	-7.06	0.071916	0	0	0	0	0	0
9	11.5	CMF	A	1	-9.25	0.113017	0	0	0	0	0	0

Table 5.13 shows the performance of the FDD system with an improper outdoor air flow fault (CF) with the TXV in superheat zones A and B. At fault levels near 20 %, the correct detection and diagnosis was made. At fault levels less than 20 %, no-fault (NF) and compressor leakage fault (CMF) were incorrectly indicated, but the EER degradation was less than 3 % for these cases. For test condition #4 at a fault level of 10 %, EER was degraded by 1.9 % while the FDD system indicated NF. As fault level increased to 20 %, the compressor fault was correctly detected and diagnosed while EER degraded by 5.7 %. For test condition #5, the CF was not diagnosed at fault levels of 5 % and 10 % with an EER degradation of 0.4 % and 1.6 %, respectively. For test condition #8, the CF was incorrectly diagnosed as a CMF fault while EER was degraded by 0.9 %.

Table 5.13 FDD results for lowered outdoor air flow fault (CF)

Test condition	Fault level	Diagnosed system status	TXV zone	EER warning	EER degradation (%)	Probability for each case						
						Compressor Leakage (CMF)	Improper OD air flow rate (CF)	Improper ID air flow rate (EF)	Liquid-line restriction (LL)	Refrigerant undercharge (UC)	Refrigerant overcharge (OC)	No Fault (NF)
4	10	NF	A	0	-1.86	4.35E-24	6.75E-10	9.80E-20	3.08E-24	1.23E-19	0.000165	0.07567
4	20	CF	A	1	-5.68	0	0.288118	0	0	0	0	0
4	35	CF	A	1	-9.82	0	3.35E-07	0	0	0	0	0
5	5	NF	A	0	-0.43	2.14E-23	9.73E-13	6.64E-18	1.26E-27	5.00E-19	6.99E-06	0.659723
5	10	CMF	A	0	-1.61	0	3.70E-09	0	0	0	9.90E-05	0.000196
5	20	CF	B	1	-5.95	0	2.72E-05	0	0	0	0	0
5	35	CF	B	1	-16.54	0	0.999999	0	0	0	0	0
5	50	CF	B	1	-36.88	0	1	0	0	0	0	0
8	10	CMF	B	0	-0.93	1.26E-28	1.85E-07	1.24E-28	6.85E-37	2.30E-26	1.75E-06	0.013527
8	20	CF	B	1	-5.23	0	2.82E-01	0	0	0	0	0
8	35	CF	B	1	-12.19	0	0.000877	0	0	0	0	0
9	5	CMF	B	0	-0.71	1.41E-33	3.32E-19	2.85E-19	3.54E-24	9.69E-28	0.062688	0.063006
9	10	NF	B	0	-1.51	0	1.24E-10	0	0	0	0.006799	4.12E-06
9	20	CF	B	1	-5.66	0	0.264652	0	0	0	0	0
9	35	CF	B	1	-11.91	0	0.005673	0	0	0	0	0

Table 5.14 shows the fault detection and diagnosis performance of the FDD algorithm for a lowered indoor air flow rate. Note that even with a more than 30 % reduction in indoor air flow, the EER decreased by less than 10 %. The dry-coil test #13 showed the largest decrease in EER. For test conditions #5 and #9, a NF was indicated with an approximately 6 % decrease in indoor air flow rate, while EER was negligibly effected. Otherwise, the FDD algorithm performed very.

Table 5.14. FDD results for lowered indoor air flow fault (EF)

Test condition	Fault level	Diagnosed system status	TXV zone	EER warning	EER degradation (%)	Probability for each case						
						Compressor Leakage (CMF)	Improper OD air flow rate (CF)	Improper ID air flow rate (EF)	Liquid-line restriction (LL)	Refrigerant undercharge (UC)	Refrigerant overcharge (OC)	No Fault (NF)
4	13.0	EF	A	0	-1.79	0	0	0.779818	0	0	2.59E-48	5.42E-35
4	22.5	EF	A	0	-2.45	0	0	0.751554	0	0	0	0
4	31.4	EF	A	1	-3.77	0	0	0.305285	0	0	0	0
5	5.9	NF	A	0	-0.18	0	0	1.27E-07	0	0	3.67E-11	0.000678
5	11.0	EF	A	0	-0.67	0	0	0.000713	0	0	9.98E-24	6.04E-16
5	20.7	EF	A	0	-1.39	0	0	0.710153	0	0	0	0
5	30.8	EF	A	0	-2.73	0	0	0.210412	0	0	0	0
8	11.8	EF	A	0	-0.99	0	0	1.99E-05	0	0	7.79E-23	2.32E-19
8	21.1	EF	A	0	-1.59	0	0	0.010518	0	0	0	0
8	33.1	EF	A	1	-3.50	0	0	2.88E-06	0	0	0	0
9	5.7	NF	A	0	-0.42	4.76E-35	1.08E-34	0.000371	1.22E-19	7.64E-22	7.61E-08	0.003588
9	10.6	EF	A	0	-0.65	0	0	0.026696	0	0	4.75E-20	8.03E-14
9	20.9	EF	A	0	-0.62	0	0	0.957496	0	0	0	0
9	30.5	EF	A	0	-1.73	0	0	0.079909	0	0	0	0
12	14.3	EF	A	0	-2.49	0	0	0.674034	0	0	0	0
12	24.1	EF	A	1	-4.43	0	0	0.039897	0	0	0	0
12	34.6	EF	A	1	-6.70	0	0	1.56E-07	0	0	0	0
13	6.1	EF	A	0	-0.80	0	0	0.034282	0	0	2.80E-38	6.88E-20
13	11.0	EF	A	0	-1.57	0	0	0.208393	0	0	0	0
13	21.1	EF	A	1	-4.08	0	0	0.147573	0	0	0	0
13	30.9	EF	A	1	-7.63	0	0	8.77E-05	0	0	0	0

Table 5.15 shows the performance of the FDD algorithm with a liquid line restriction fault imposed. A large LL fault level was needed before EER degradation exceeded 3 %. At fault levels where the EER degradation exceeded 3 %, the fault was correctly diagnosed. At EER degradations lower than 3 %, the LL fault tended to be diagnosed as NF.

Table 5.15. FDD results for liquid-line restriction fault (LL)

Test condition	Fault level	Diagnosed system status	TXV zone	EER warning	EER degradation (%)	Probability for each case						
						Compressor Leakage (CMF)	Improper OD air flow rate (CF)	Improper ID air flow rate (EF)	Liquid-line restriction (LL)	Refrigerant undercharge (UC)	Refrigerant overcharge (OC)	No Fault (NF)
4	3.7	NF	A	0	-1.48	9.18E-21	2.44E-16	1.24E-10	2.36E-14	2.01E-14	4.62E-05	0.665639
4	7.0	NF	A	0	-1.08	5.15E-16	2.28E-13	2.17E-11	3.17E-14	9.68E-11	2.23E-07	0.777571
4	12.5	NF	A	0	-0.94	4.24E-16	9.84E-15	1.78E-15	2.29E-12	4.38E-10	3.68E-10	0.123811
4	19.0	LL	B	0	-1.24	0	3.47E-16	5.20E-49	2.96E-08	4.08E-18	1.23E-21	1.26E-36
5	5.3	NF	A	0	-0.22	1.69E-19	6.68E-14	4.72E-14	1.06E-25	4.79E-16	1.28E-07	0.793808
5	10.4	NF	B	0	-0.21	5.81E-16	9.50E-12	2.13E-09	7.25E-09	2.29E-07	8.36E-11	0.055037
5	20.2	LL	B	1	-5.89	0	0	0	0.996187	0	0	0
5	31.9	LL	B	1	-24.43	0	0	0	1	0	0	0
8	4.4	NF	A	0	-0.22	1.33E-24	3.14E-15	1.35E-14	1.25E-20	1.32E-18	0.000209	0.607407
8	8.8	NF	A	0	0.34	1.98E-22	2.77E-13	4.07E-15	5.14E-24	3.18E-18	3.83E-06	0.717091
8	13.3	NF	A	0	0.22	1.05E-28	2.16E-15	5.06E-18	5.77E-24	1.86E-25	0.017534	0.175031
9	7.1	NF	A	0	0.35	2.65E-11	2.32E-15	1.49E-08	9.25E-15	1.24E-05	3.57E-14	0.557706
9	13.3	NF	A	0	0.21	5.64E-20	2.36E-15	1.57E-15	5.67E-13	6.70E-16	4.61E-08	4.63E-05
9	20.0	LL	B	0	-0.44	0	0	0	0.002216	0	0	0

Table 5.16 shows that the FDD algorithm correctly diagnosed the undercharged refrigerant fault at all fault levels presented for both TXV zones A and B as seen in Figure 5.10. This is very promising due to the common occurrence of this fault.

Table 5.16. FDD results for refrigerant undercharge fault (UC)

Test condition	Fault level	Diagnosed system status	TXV zone	EER warning	EER degradation (%)	Compressor Leakage (CMF)	Improper OD air flow rate (CF)	Improper ID air flow rate (EF)	Liquid-line restriction (LL)	Refrigerant undercharge (UC)	Refrigerant overcharge (OC)	No Fault (NF)
						Probability for each case						
4	10	UC	A	0	-2.87	7.03E-08	0	0	0	0.099239	0	0
4	20	UC	B	1	-3.56	0	0	0	0	0.999967	0	0
4	30	UC	B	1	-68.81	0	0	0	0	1	0	0
5	10	UC	B	0	-2.95	0	0	0	0	0.999208	0	0
5	20	UC	B	1	-7.25	0	0	0	0	1	0	0
5	30	UC	B	1	-20.14	0	0	0	0	1	0	0
8	10	UC	A	0	-2.36	6.75E-15	0	0	0	0.011534	0	0
8	20	UC	A	1	-4.09	8.54E-17	0	0	0	0.001896	0	0
8	30	UC	B	1	-9.45	0	0	0	0	1	0	0
9	10	UC	B	0	-0.87	3.61E-17	0	0	0	0.005703	0	0
9	20	UC	B	1	-6.06	0	0	0	0	1	0	0
9	30	UC	B	1	-15.79	0	0	0	0	1	0	0

Table 5.17 shows the performance of the FDD algorithm for an overcharged refrigerant fault. In all cases the fault was correctly diagnosed, even when the EER degradation was below 3 %.

Table 5.17. FDD results for refrigerant overcharge fault (OC)

Test condition	Fault level	Diagnosed system status	TXV zone	EER warning	EER degradation (%)	Probability for each case						
						Compressor Leakage (CMF)	Improper OD air flow rate (CF)	Improper ID air flow rate (EF)	Liquid-line restriction (LL)	Refrigerant undercharge (UC)	Refrigerant overcharge (OC)	No Fault (NF)
4	10	OC	A	0	-0.95	0	0	0	0	0	0.176407	0
4	20	OC	A	0	-1.89	0	0	0	0	0	0.854211	0
4	30	OC	A	1	-3.41	0	0	0	0	0	0.696819	0
5	10	OC	A	0	1.14	0	0	0	0	0	0.002974	1.30E-19
5	20	OC	A	0	-0.10	0	0	0	0	0	0.646483	0
5	30	OC	A	0	-2.84	0	0	0	0	0	0.015035	0
8	10	OC	A	0	-0.92	0	0	0	0	0	0.214176	0
8	20	OC	A	0	-2.21	0	0	0	0	0	0.051813	0
8	30	OC	A	1	-3.71	0	0	0	0	0	0.002555	0
9	10	OC	A	0	0.90	0	0	0	0	0	0.00027	1.11E-20
9	20	OC	A	0	-0.21	0	0	0	0	0	0.142298	0
9	30	OC	A	0	-2.32	0	0	0	0	0	0.029946	0

The FDD algorithm correctly diagnosed all faults causing an EER degradation of more than 3.5 %. Misdiagnosed faults occurred under the conditions noted in Table 5.17 at a maximum EER degradation of 3.4 %.

The liquid line restriction fault produced the highest number of misdiagnosed faults, but these faults occurred with a 1.5 % or less degradation in EER. Liquid line restriction was consistently misdiagnosed as a NF (no-fault) even at fault levels as high as 13 %. Even at this fault level, the liquid line fault was not degrading system EER. EER was relatively insensitive to this fault at the fault levels and test conditions of this study.

Table 5.18. Misdiagnosed faults

Single-Fault Imposed	Indoor to Outdoor Temperature Lift (ºC)	Fault Level (%)	Fault Indicated	EER degradation (%)
CMF	6.7	2.5	NF	3.4
CMF	16.7	2.5	NF	2.5
CMF	11.1	2.4	UC	1.3
CF	6.7	10	NF	1.9
CF	1.1	5	NF	0.4
CF	1.1	10	CMF	1.6
CF	16.7	10	CMF	0.9
CF	11.1	5	CMF	0.7
CF	11.1	10	NF	1.5
EF	1.1	5.9	NF	0.2
EF	11.1	5.7	NF	0.4
LL	6.7	3.7	NF	1.5
LL	6.7	7.0	NF	1.1
LL	6.7	12.5	NF	0.9
LL	1.1	5.3	NF	0.2
LL	1.1	10.4	NF	0.2
LL	16.7	4.4	NF	0.2
LL	16.7	8.8	NF	0.0
LL	11.1	7.1	NF	0.0
LL	11.1	13.3	NF	0.0

CHAPTER 6. CONCLUDING REMARKS

Single-fault test data for an R410A residential unitary split heat pump tested by Kim et al. (2006) in the cooling mode was used to develop an FDD algorithm. This heat pump was equipped with a TXV for the cooling mode expansion device; the TXV tried to maintain evaporator exit superheat even though a fault was occurring. This added level of control meant that faults occurring when the TXV was within its operational range (Zone A in Figure 5.10) or outside of its operational range (Zone B) had to be treated differently. The response of system temperatures to these single-faults was monitored, and their changes during faulty operation formed the basis for the FDD algorithm.

The steady-state detector, SSD, acted as a filter of the dependent variables (features). The SSD was based upon a moving window in the which standard deviation of every feature used by the FDD algorithm must fall below a threshold value before the system is defined as steady-state. The feature standard deviation thresholds were based upon no-fault steady state standard deviations multiplied by a factor of three. The sampling rate and size of the moving window were determined by transient (start-up) tests of the no-fault system.

Once a SSD was developed, a steady-state reference model was formulated. Two different types of feature-correlating models were considered; a multi-variate polynomial regression (MPR) and an artificial neural network (ANN). The 3rd order MPR model produced a better fit than the ANN and was further employed in the FDD system. The 3rd order MPR model was exposed to an F-test to illustrate how the number of coefficients could be reduced to produce a more compact correlation.

Once the no-fault reference model was developed, the cooling mode heat pump's features (temperatures) could be compared to their reference model counterparts and residual values calculated. These residuals were positive, negative or neutral with respect to their no-fault values. A feature's neutrality was defined by how far its residual was from zero. A feature's neutrality threshold was defined by three sources of uncertainty; measurement uncertainty, lack of measurement repeatability, and modeling uncertainty. Each of these uncertainty terms was multiplied by a coverage factor to ensure the desired confidence level, and then a square rooted sum of squares was taken to represent the total uncertainty or neutral threshold value for each feature. A rule-based chart was then generated by noting that certain faults produced a certain arrangement of positive, negative, or neutral residuals within the FDD feature set. Also, the probability of a residual being positive, negative, or neutral was calculated allowing for the determination of a fault probability relative to a no-fault probability. When the fault probability was greater than the no-fault probability, a fault was diagnosed in the system.

The person implementing this FDD method should be aware of the following points:

1. When this FDD algorithm is applied to a real system, some method of determining when to notify the homeowner or responsible authority must be implemented. A fixed percentage degradation in EER can be selected as the notification impetus. Calculating EER using compressor maps and measured temperatures proved to be very effective due to the accurate compressor maps for the tested system.

2. Using only temperatures is not the preferred method for determining the suction and discharge refrigerant saturation temperatures needed by the power and mass flow compressor map equations. A more accurate FDD system would include suction and discharge pressure transducers to provide input to the compressor map equations and allow more accurate superheat and subcooling calculations.

3. Other implementations could choose some parameter other than EER as a notification impetus, or the fault level itself could be correlated and used.

Future work should focus on developing a complete FDD module for a residential heat pump/AC system that is "self training." Adaptable FDD algorithms are necessary for split, field-installed heat pump systems because each installation is unique. A rigid FDD algorithm will not perform correctly under all installation conditions; therefore, a method for evolving the reference model for newly installed systems must be developed.

REFERENCES

Aaron, A. A. and Domanski, P A., 1989, "An experimental investigation and modeling of the flow rate of refrigerant 22 through the short tube restrictor," NISTIR 89-4120, National Institute of Standards and Technology, Washington, DC.

Anderson, D., Graves, L., Reinert, W., Kreider, J.F., Dow, J., and Wubbena, H., 1989, "A Quasi-Real-Time Expert System for Commercial Building HVAC Diagnostics," *ASHRAE Transactions*, Vol. 95, Part 2, pp. 25-28.

ARI, 2004, "Performance rating of positive displacement refrigerant compressors and compressor units," ARI Standard 540, Air Conditioning and Refrigeration Institute, Arlington, VA, USA

ARI, 2006, "Performance rating of unitary airconditioning and airsource heat pump equipment," ARI Standard 210/240, Air Conditioning and Refrigeration Institute, Arlington, VA, USA

Breuker, M.S. and Braun, J.E., 1998a, "Common faults and their impacts for rooftop air conditioners," *International Journal of Heating, Ventilating, Air-Conditioning and Refrigerating Research*, Vol. 4, No. 3, pp. 303-318.

Breuker, M.S. and Braun, J.E., 1998b, "Evaluating the performance of a fault detection and diagnostic system for vapor compression equipment," HVAC&R Research, Vol. 4, No. 4, pp. 401-425.

Cao S, Rhinehart R. An efficient method for on-line identification of steady-state. J Process Control 1995;5(6);363-374.

Castro, N.S., 2002, "Performance Evaluation of a Reciprocating Chiller Using Experimental Data and Model Predictions for Fault Detection and Diagnosis," *ASHARE Transactions*, Vol. 108, Pt. 1, pp. 889-903.

Chen, B. and Braun, J.E., 2001, "Simple Rule-Based Methods for Fault Detection and Diagnostics Applied to Packaged Air Conditioners," *ASHRAE Transactions*, Vol. 107, Pt. 1, pp. 847-857.

Comstock, M.C., Braun, J.E., and Groll, E.A., 2001, "The Sensitivity of Chiller Performance to Common Faults," *HVAC&R Research*, Vol. 7, No. 3, pp. 263-279.

Dabiri, A. E. and Rice, C. K., 1981, "A compressor simulation model with corrections for the level of suction gas superheat," ASHRAE Transactions, Vol. 87, Part 2, pp. 771-782.

Franklin GF, Powell JD, Emami-Naeini A, 1991, Feedback control of dynamic systems (2nd Edition), Addison-Wesley Publishing Company, Reading, MA USA, 1991;617.

Glass AS, Gruber P, Roos M, Tödtli J. Qualitative model-based fault detection in air-handling units. IEEE Control Systems Magazine, 1995;15(4);11-22.

Gordon, J. M. and Ng, K. C., 1995, "Predictive and diagnostic aspects of a universal thermodynamic model for chillers," International Journal of Heat and Mass Transfer, Vol. 38, No. 5, pp. 807-818.

Graybill, F. A. and Iyer, H. K., 1994a, Regression analysis: concepts and applications, 2nd edition, Duxbury Press, Belmont California, pp. 239-241.

Graybill, F. A. and Iyer, H. K., 1994b, Regression analysis: concepts and applications, 2nd edition, Duxbury Press, Belmont California, pp. 431-437.

Grimmelius, H.T., Woud, J.K., and Been, G., 1995, "On-line Failure Diagnosis for Compression Refrigeration Plants," *International Journal of Refrigeration*, Vol. 18, No. 1, pp. 31-41.

Hassoun, M.H., 1995, "Fundamentals of Artificial Neural Networks", The MIT Press, Cambridge, MA.

Isermann, R. 1984, "Process fault detection based on modeling and estimation methods—A survey," *Automatica*, Vol. 20-4, 387-404.

Jiang T, Chen B, He X, Stuart P. Application of steady-state detection method based on wavelet transform. Computers and Chemical Engineering 2003;27(4);569-578

Kim, M. and Kim, M.S., 2005, "Performance Investigation of a Variable Speed Vapor Compression System for Fault Detection and Diagnosis," *International Journal of Refrigeration*, Vol. 28, No. 4, pp. 481-488.

Kim, M., Payne, W.V., Hermes, C.J.L., and Domanski, P.A., 2006, "Performance of a Residential Air Conditioner at Single-Fault and Multiple-Fault Conditions," NISTIR 7350, National Institute of Standards and Technology, Gaithersburg, MD.

Kim, M., Yoon, S. H., Payne, W. V., and Domanski, P. A., 2008, "Design of a steady-state detector for fault detection and diagnosis of a residential air conditioner," International Journal of Refrigeration 31(5), 790-99.

Kramer, M.A., 1987, "Malfunction Diagnosis Using Quantitative Models with Non-Boolean Reasoning in Expert Systems," *AIChE Journal*, Vol. 33, No. 1, pp. 130-140.

Kramer, M.A. and Palowitch, B.L., 1987, "Rule-Based Approach to Fault Diagnosis Using the Signed Directed Graph," *AIChE Journal*, Vol. 33, No. 7, pp. 1067-1078.

Krandel, A., 1992, Fuzzy Techniques in Pattern Recognition, Wiley, New York.

Lee, W.S., Grosh, D.L., Tillman, F.A., and Lie, C.H., 1985, "Fault Tree Analysis, Methods, and Applications – A Review," *IEEE Transactions on Reliability*, Vol. R-34, No. 3, pp. 194-203.

Lee, W.Y., Park, C., and Kelly, G.E., 1996a, "Fault Detection in an Air-Handling Unit Using Residual and Recursive Parameter Identification Methods," *ASHRAE Transactions*, Vol. 102, Part 1, pp. 528-539.

Lee, W.Y., House, J.M., Park, C., and Kelly, G.E., 1996b, "Fault Diagnosis of Air-Handling Unit Using Artificial Neural Networks," *ASHRAE Transactions*, Vol. 102, Part. 1, pp. 540-549.

Lemmon EW, McLinden MO, Huber ML., 1998, NIST Reference fluid thermodynamic and transport properties – REFPROP, Version 7.0. National Institute of Standards and Technology, Gaithersburg, MD USA.

Li, H. and Braun, J.E., 2003, "An Improved Method for Fault Detection and Diagnosis Applied to Packaged Air Conditioners," *ASHRAE Transactions*, Vol. 109, Pt. 2, pp. 683-692.

Li H. A decoupling-based unified fault detection and diagnosis approach for packaged air conditioners. Ph.D. Thesis, West Lafayette, IN: Purdue University, 2004.

Mahuli SK, Rhinehart R, Riggs JB. Experimental demonstration of non-linear model-based in-line control of pH. J Process Control 1992;2(3);145-153.

Navarro-Esbri J, Torrella E, Cabello R., 2007, "A vapour compression chiller fault detection technique based on adaptive algorithms. Application to on-line refrigerant leakage detection," International Journal of Refrigeration, Vol. 29, pp. 716-723.

Norford, L.K. and Little, R.D., 1993, "Fault Detection and Load Monitoring in Ventilation System," *ASHRAE Transactions*, Vol. 99, Part 1, pp. 590-602.

Ott, L., 1984, An introduction to statistical methods and data analysis, 2nd edition, PWS Publishers, Duxbury Press, Boston, Massachusetts, ISBN 0-87150-473-1, pp. 438-443.

Pape, F.L.F., Mitchell, J.W., and Beckman, W.A., 1991, "Optimal Control and Fault Detection in Heating, Ventilating, and Air-Conditioning System," *ASHRAE Transactions*, Vol. 97, Part 1, pp. 729-745.

Peitsman, H.C. and Bakker, V.E., 1996, "Application of Black-Box Models to HVAC Systems for Fault Detection," *ASHRAE Transactions*, Vol. 102, Part. 1, pp. 628-640.

Proctor, J., 2004, "Residential and Small Commercial Central Air Conditioning; Rated Efficiency isn't Automatic," Presentation at the Public Session. ASHRAE Winter Meeting, January 26, Anaheim, CA.

Rossi, T.M., 1995, Detection, diagnosis, and evaluation of faults in vapor compression cycle equipment, Ph.D. Thesis, Purdue University, West Lafayette, IN, USA

Rossi, T.M. and Braun, J.E., 1997, "A statistical, rule-based fault detection and diagnostic method for vapor compression air conditioners, *International Journal of Heating, Ventilating, Air-Conditioning and Refrigerating Research*," Vol. 3, No. 1, pp. 19-37.

Rossi, T.M., 2004, "Unitary Air Conditioner Field Performance," International Refrigeration and Air Conditioning Conference at Purdue, Paper No. R146, July 12-15, West Lafayette, IN.

Schein, J. and Bushby, S., 2005, "A Simulation Study of a Hierarchical, Rule-Based Method for System-Level Fault Detection and Diagnostics in HVAC Systems," *NISTIR 7216*, National Institute of Standards and Technology, Gaithersburg, MD.

Smith, V.A. and Braun, J.E., 2003, "Fault Detection and Diagnostics for Rooftop Air Conditioners," Final Report Compilation for Project 2.1, Publication #P500-03-096, California Energy Commission, http://www.archenergy.com/cec-eeb/reports.htm

Stylianou, M. and Nikanpour, D., 1996, "Performance Monitoring, Fault Detection and Diagnosis of Reciprocating Chillers," ASHRAE Transactions, Vol. 102, Pt. 1, pp. 615-627.

Stylianou, M., 1997, "Application of Classification Functions to Chiller Fault Detection and Diagnosis," *ASHRAE Transactions*, Vol. 103, Pt. 1, pp. 645-656.

Tzafestas, S.G., 1989, "System Fault Diagnosis Using the Knowledge-Based Methodology," Fault Diagnosis in Dynamic Systems Theory and Applications, Prentice Hall, New York, pp. 514-543.

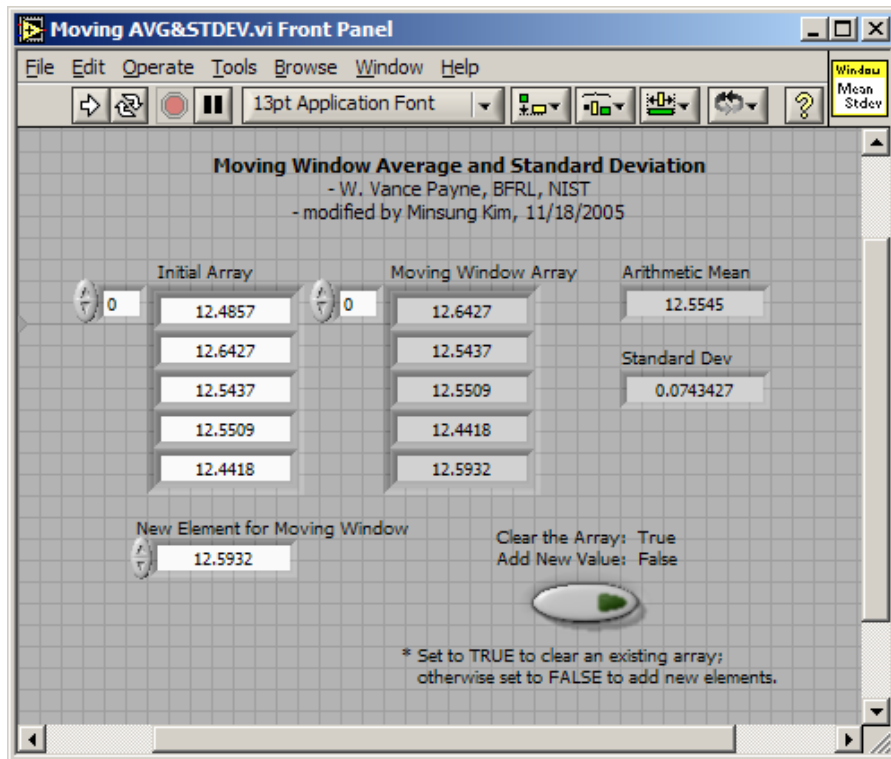Wasserman, P.D., 1989, "Neural Computing Theory and Practice", Van Nostrand Reinhold, New York, NY.

APPENDIX A. FDD MODULES

This appendix presents individual windows of the FDD system developed and implemented on the split residential system used in this study.
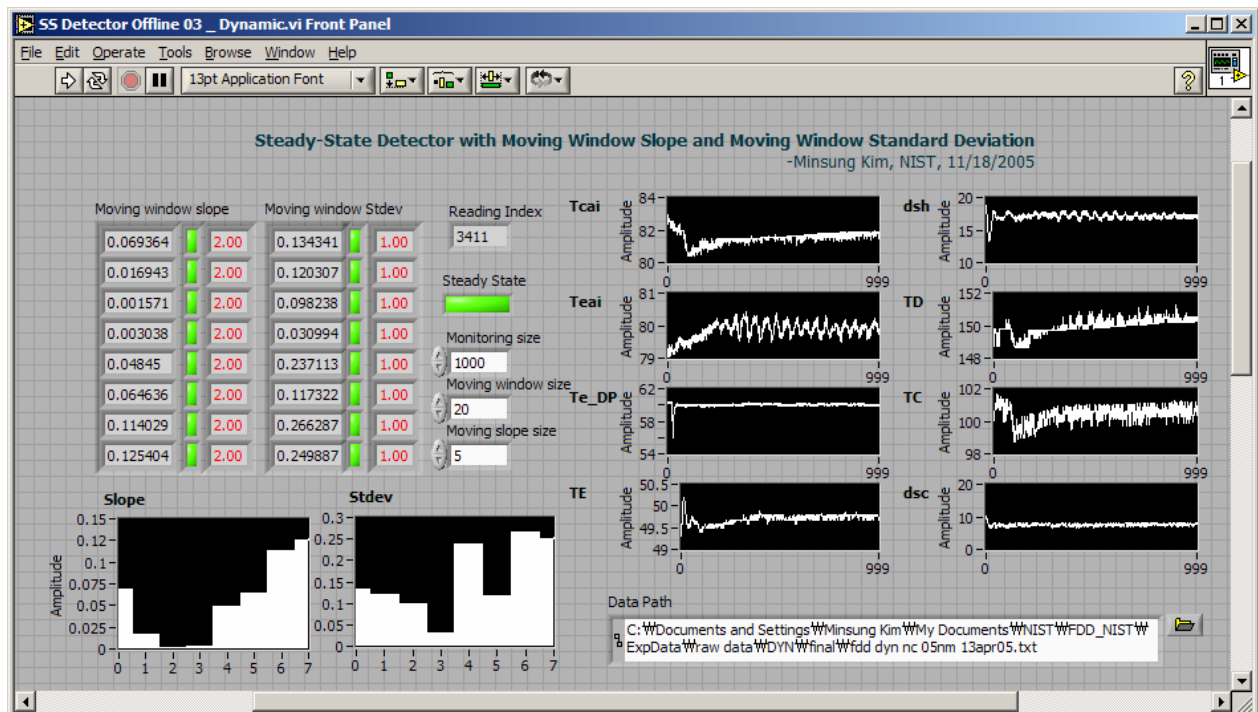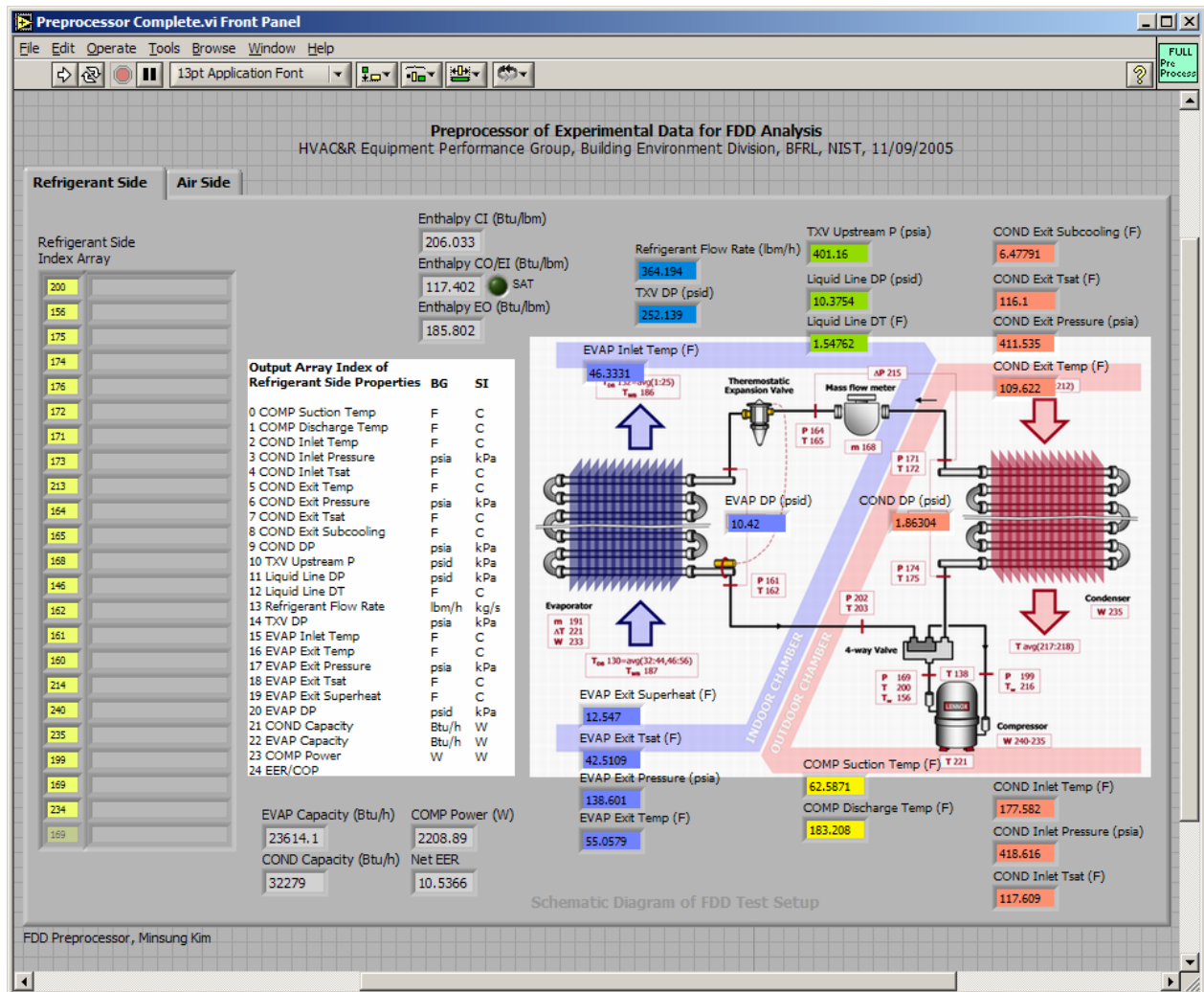
A.1 Main Module
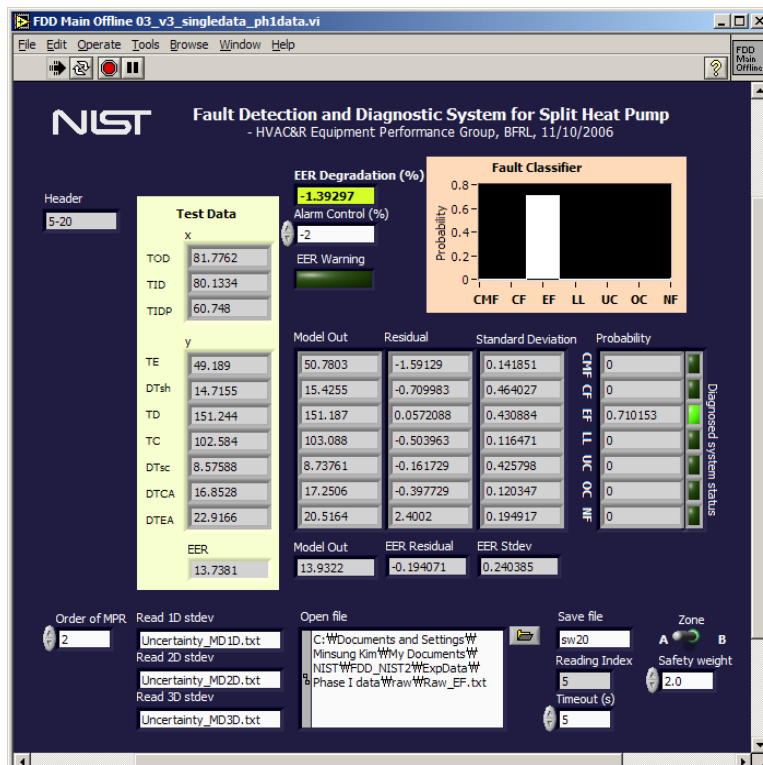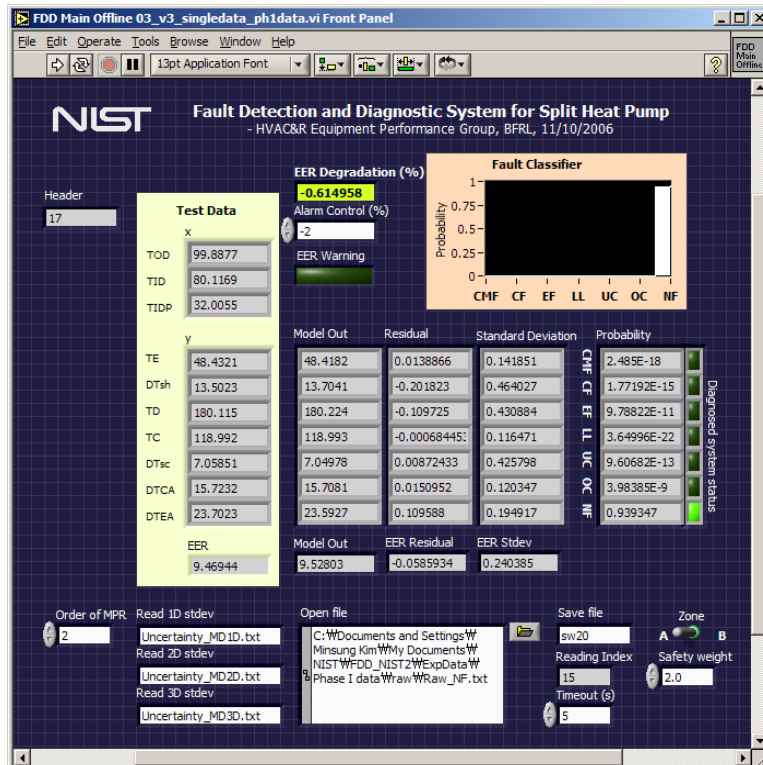
A.2 Moving Window Module
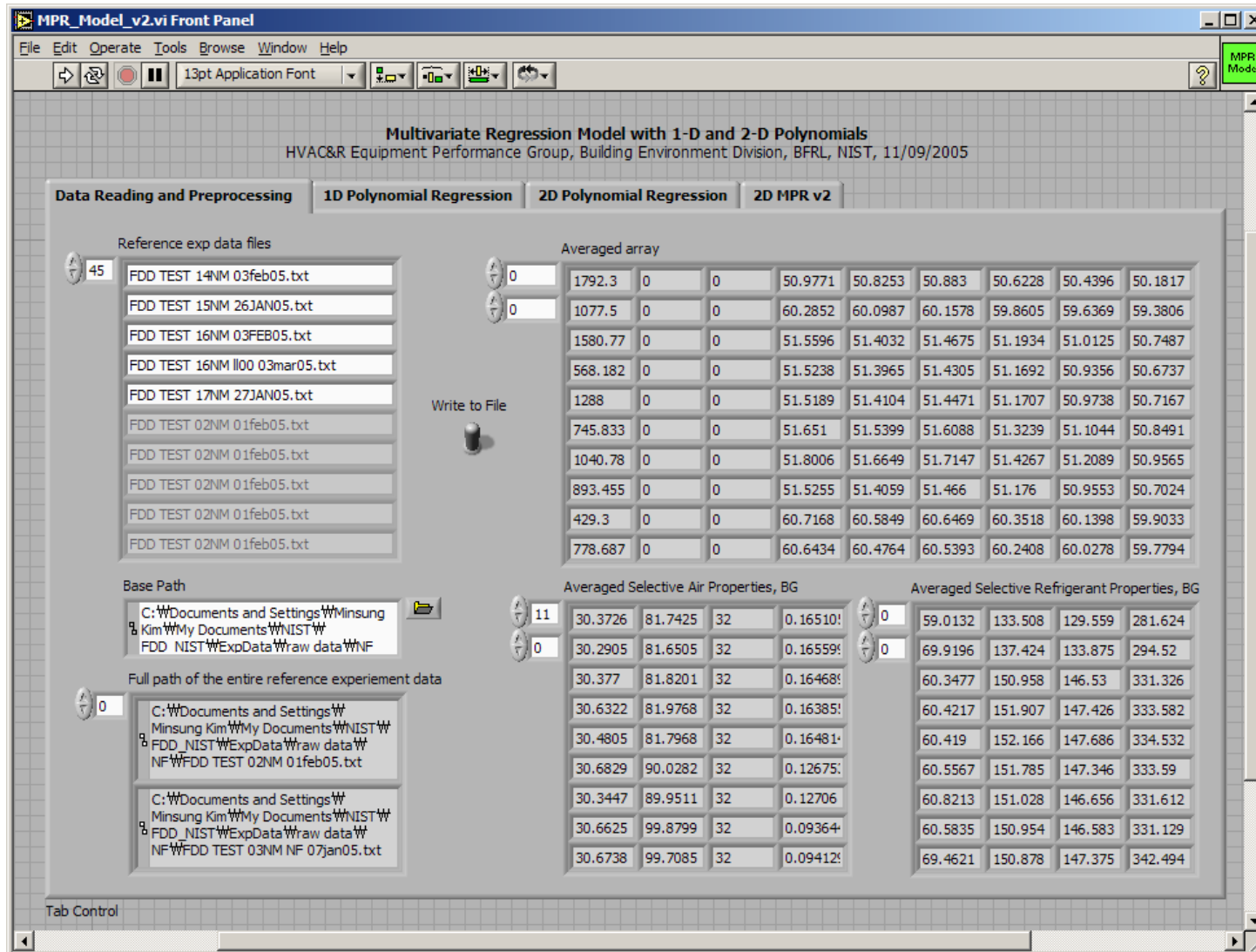

A.3 Steady-State Detector Module

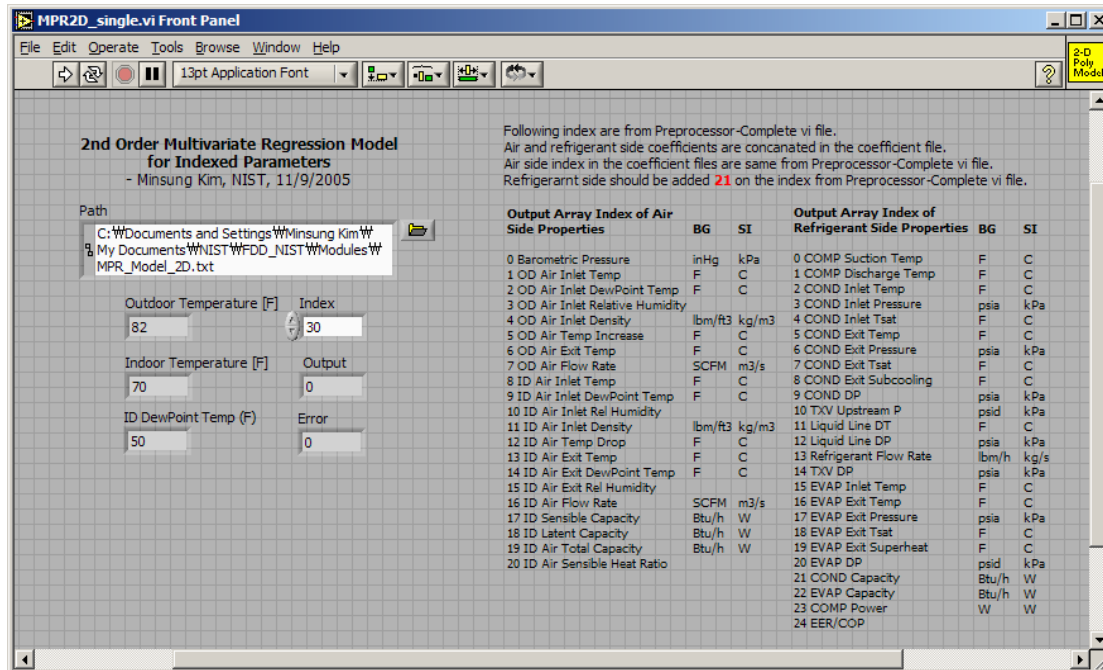## A.4 Preprocessor Module

A.5 Reference Model Correlation Interface

A.6 No-Fault MPR Reference Module

A.7 Statistical Rule-Based FDD Module